A NEW APPARATUS FOR STUDIES OF QUANTIZED VORTEX DYNAMICS IN DILUTE-GAS BOSE-EINSTEIN CONDENSATES

by

Zachary L Newman

A Dissertation Submitted to the Faculty of the

COLLEGE OF OPTICAL SCIENCES

In Partial Fulfillment of the Requirements
For the Degree of

DOCTOR OF PHILOSOPHY

In the Graduate College

THE UNIVERSITY OF ARIZONA

2016

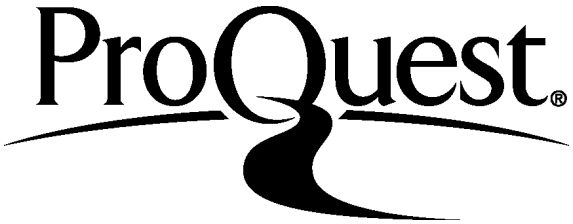

THE UNIVERSITY OF ARIZONA
GRADUATE COLLEGE

As members of the Dissertation Committee, we certify that we have read the dissertation prepared by Zachary L Newman
entitled A New Apparatus for Studies of Quantized Vortex Dynamics in Dilute-Gas Bose-Einstein Condensates
and recommend that it be accepted as fulfilling the dissertation requirement for the Degree of Doctor of Philosophy.

Date: 22 April 2016

Brian P. Anderson

Date: 22 April 2016

Ewan M. Wright

Date: 22 April 2016

R. Jason Jones

Date: 22 April 2016

Final approval and acceptance of this dissertation is contingent upon the candidate's submission of the final copies of the dissertation to the Graduate College.
I hereby certify that I have read this dissertation prepared under my direction and recommend that it be accepted as fulfilling the dissertation requirement.

Date: 22 April 2016

Dissertation Director: Brian P. Anderson

STATEMENT BY AUTHOR

This dissertation has been submitted in partial fulfillment of requirements for an advanced degree at the University of Arizona and is deposited in the University Library to be made available to borrowers under rules of the Library.

Brief quotations from this dissertation are allowable without special permission, provided that accurate acknowledgment of source is made. Requests for permission for extended quotation from or reproduction of this manuscript in whole or in part may be granted by the head of the major department or the Dean of the Graduate College when in his or her judgment the proposed use of the material is in the interests of scholarship. In all other instances, however, permission must be obtained from the author.

SIGNED: Zachary L Newman

ACKNOWLEDGEMENTS

I would like to thank my advisor, Brian Anderson, for his guidance and encouragement over the past seven years. His physical intuition, creativity, and his methodical approach to solving complicated problems have been invaluable in the lab. I consider Brian one of my closest friends and am thankful for our morning talks, late night zombie movies, backpacking trips and many other fun adventures. I would also like to thank the other members of my committee, Jason Jones and Ewan Wright, for their assistance with this thesis and throughout my Phd.

Finishing a Phd is the culmination of a (very) long stint in the educational system and I am extremely grateful to all my mentors and teachers. I want to say a special thanks to my high school math teacher, Mr. (Sam) Tumolo, who has been in my corner since I started high school. Sam and Jeanie retired and moved out to Tucson shortly after I started graduate school and have become dear friends over the past six years.

Kali Wilson has been another great friend and mentor. Kali joined the BEC group a year before I did and was always willing to help me scramble over the hurdles she had just leapt over. We have had many thoughtful discussions about life and physics and countless adventures together. Kali is a brilliant scientist and a thoughtful and caring friend and I imagine we will continue to stay close for a very long time.

Of course, I am deeply indebted to the other members of the BEC group. Jessica Myers has played a major role in nearly all the work described in this dissertation and it was an absolute pleasure working with her in the lab. Jessica has a deep passion for education and I know she will become a great mentor and teacher in the future. Although I didn't work directly with Joe Lowney and Sam Neremberg I consider both of them close friends. Joe and I shared many insightful conversations during late evenings in at the office or on the car ride home. Sam is intelligent, energetic and very funny. Room 572 is in capable hands going forward. Finally, Andrew Schaffer joined the Jessica and I in the lab in my last semester in Tucson. Although we didn't overlap for very long, I had a blast spending time with him in the lab. We share a dry sense of humor and a love of sports and, of course, Jimmy Johns sandwiches. I know that he'll do some great science with the new system and I look forward to working with him again.

I have thoroughly enjoyed scientific (and non-scientific) discussions with the guys in the Quantum Information and Control group (Pascal, Hector, Enrique, Dan, David and Nathan).

I want to thank my Aunt Eve and Uncle Joe (my unofficial third set of grandparents) for nudging me in the direction of physics. Some of my best memories involve

traveling to DC to visit and helping fill Opthos boxes with packing peanuts. Who would have guessed that the lasers in the new lab would be referenced to Opthos Rb cells! I am so proud to be joining the NIST family this summer for my post-doc.

None of the work in this thesis would have been possible without the support and camaraderie of my close friends David and Cecile C., Kali W., Logan A., Julia T., Tyler T., Blake C., Jimmy R., Andrey A., Pascal M., Hector S., Marc V., Alec D., Shane A., Garam and Stefano Y., the Millstones, Stacey S. and Anael G. Thank you for making Tucson a second home for me.

Finally, special thanks to my family, who have supported me my entire life: grandma Dorsey and grandpa Irv, grandma Char, mom, dad, Andrea and Laura. It's hard to imagine getting to this point without a lot of help along the way. I love you guys.

TABLE OF CONTENTS

LIST OF FIGURES

LIST OF TABLES

ABSTRACT

The presence of quantized vortices and a high level of control over trap geometries and other system parameters make dilute-gas Bose-Einstein condensates (BECs) a natural environment for studies of vortex dynamics and quantum turbulence in superfluids, primary interests of the BEC group at the University of Arizona. Such research may lead to deeper understanding of the nature of quantum fluid dynamics and far-from-equilbrium phenomena.

Despite the importance of quantized vortex dynamics in the fields of superfluidity, superconductivity and quantum turbulence, direct imaging of vortices in trapped BECs remains a significant technical challenge. This is primarily due to the small size of the vortex core in a trapped gas, which is typically a few hundred nanometers in diameter. In this dissertation I present the design and construction of a new ^{87}Rb BEC apparatus with the goal of studying vortex dynamics in trapped BECs. The heart of the apparatus is a compact vacuum chamber with a custom, all-glass science cell designed to accommodate the use of commercial high-numerical-aperture microscope objectives for *in situ* imaging of vortices.

The designs for the new system are, in part, based on prior work in our group on *in situ* imaging of vortices. Here I review aspects of our prior work and discuss some of the successes and limitations that are relevant to the new apparatus. The bulk of the thesis is used to described the major subsystems of the new apparatus which include the vacuum chamber, the laser systems, the magnetic transfer system and the final magnetic trap for the atoms. Finally, I demonstrate the creation of a BEC of $\sim 2 \times 10^6$ ^{87}Rb atoms in our new system and show that the BEC can be transferred into a weak, spherical, magnetic trap with a well defined magnetic field axis that may be useful for future vortex imaging studies.

CHAPTER 1

Introduction

Bose-Einstein condensation was first predicted for massive particles by Einstein in 1924 [1, 2] following the statistical analysis by Bose [3] on the energy distribution of photons radiated from a blackbody. In his work, Einstein predicted that below a certain critical temperature, T_C, a system of identical, non-interacting, massive bosons would undergo a phase transition in which a finite fraction of the total number of particles in the system would occupy the quantum mechanical ground state. This phenomenon is unique to bosons (particles with integer spin) since the Pauli exclusion principle restricts identical fermions from occupying the same state.

Superfluidity, which refers to a state of fluid flow without dissipation due to viscosity, was discovered in 1938 by Kapitza [4] and Allen and Meisner [5] by measuring flow of liquid ^{4}He through small channels. In the same year London [6] suggested a connection between superfluid liquid ^{4}He and an ideal Bose-Einstein condensate (BEC) by noting that the discontinuity in specific heat in liquid ^{4}He at the λ-point closely resembles the same discontinuity in an ideal, non-interacting Bose gas. The discovery of superfluid liquid ^{4}He represents the first realization of Einstein's ideas in a physical system and connects the concepts of superfluidity and Bose-Einstein condensation.

One of the hallmarks of superfluid flow is the presence of quantized vortices, which were first proposed by Onsager in his 1949 paper on statistical hydrodynamics [7]. Vinen later confirmed Onsager's predictions by measuring the rate of precession of a wire submerged in a rotating vessel of liquid ^{4}He [8, 9]. Quantized

vortices play an important role in superfluid phenomena and an understanding of the dynamics of quantized vortices is of critical importance in the fields of superfluidity and superconductivity and may lead to a greater understanding of practical issues such as the decay of current in superconductors [10]. For good reviews of superfluidity and vortices in superfluids see Refs. [11, 12].

Despite the large volume of work on quatized vortices in liquid ^{4}He and their importance in a number of related fields, direct visualization of vortices in a superfluid remains an important technical challenge. The first direct observation of quantized vortices in a superfluid was demonstrated by Yarmchuck *et al.* [13] in 1979. In this work regular arrays of quantized vortices were observed in a rotating volume of ^{4}He by charging vortex lines with electrons which were recorded on a photographic plate, however this technique was limited to parallel arrays of vortices where the ends of the vortex lines were accessible. More widely used techniques for studying superfluid dynamics, such as second sound attenuation [14] and ion-trapping, probe only bulk properties of the flow like the vortex-line density averaged over a large volume [15]. More recently, Bewley *et al.* [16, 17, 18] have demonstrated the ability to observe arbitrary, three-dimensional distributions of vortices using solid, micron-sized hydrogen particles trapped in the vortex core as tracers of the motion of vortex lines. The use of micron-sized hydrogen particles as tracers of vortex motion in Helium is an significant step forward in experimental investigations of vortex dynamics and this technique has been utilized to study quantized vortex reconnections [19, 20] and aspects of quantum turbulence in ^{4}He [21, 22]. In some cases however, the presence of tracer particles can effect the stability and dynamics of vortices they are entrained in [23]. In addition, the strong interactions in liquid He present difficulties in a theoretical understanding of vortex dynamics.

Dilute-gas BECs[1] offer a unique environment for studies of superfluid dynamics and quantized vortices for several reasons: First, due to weak atom-atom interactions, vortices in dilute gas BECs can be visualized directly in time-of-flight expansion of the BEC [28]. Second, the lasers and magnetic fields required for cooling and trapping allow a high degree of control over the local environment and the quantum mechanical state of the atoms in the BEC. Finally, the Gross-Pitaevskii equation (GPE) gives an accurate description of the dynamics of the fluid and provides theoretical framework for experiments [29, 30].

Research in the BEC group at the University of Arizona has focused on the study of the dynamics of quantized vortices in dilute-gas BECs, especially as they relate to phase transitions, the nature of superfluidity, and quantum turbulence in two dimensions. A long-term goal of the group is to build a detailed understanding of vortex generation, annihilation, interactions and dynamics in BECs. Detailed studies of vortex dynamics requires overcoming three key technical challenges: 1) The ability to non-destructively image vortex distributions in *in situ*; 2) methods for engineering arbitrary arrangements of many vortices in a BEC; and 3) access to a wide range of BEC trapping geometries.

The work in this dissertation involves the design and construction of a new BEC apparatus for our group, with the goal of making advances in all three of these areas. The designs for the new apparatus draw on the designs and experiences working with our original apparatus and the successes and limitations of the vortex manipulation

[1] Bose-Einstein Condensates (BECs) were first realized in dilute atomic gases of ^{87}Rb [24], ^{23}Na [25], and ^{7}Li [26, 27] in 1995. The demonstration of Bose-Einstein condensation in dilute gases represents the culmination of nearly a quarter century of prior work on laser cooling and trapping of neutral atoms and has had a major impact on the field of atomic physics. To date, dilute-gas BECs have been demonstrated in isotopes of H, He, Li, Na, K, Ca, Cr, Rb, Sr, Cs, Y, Dy and Er. The list of atoms that have been condensed is largely composed of atoms with a simple valence electronic structure for which sources for laser cooling are widely available.

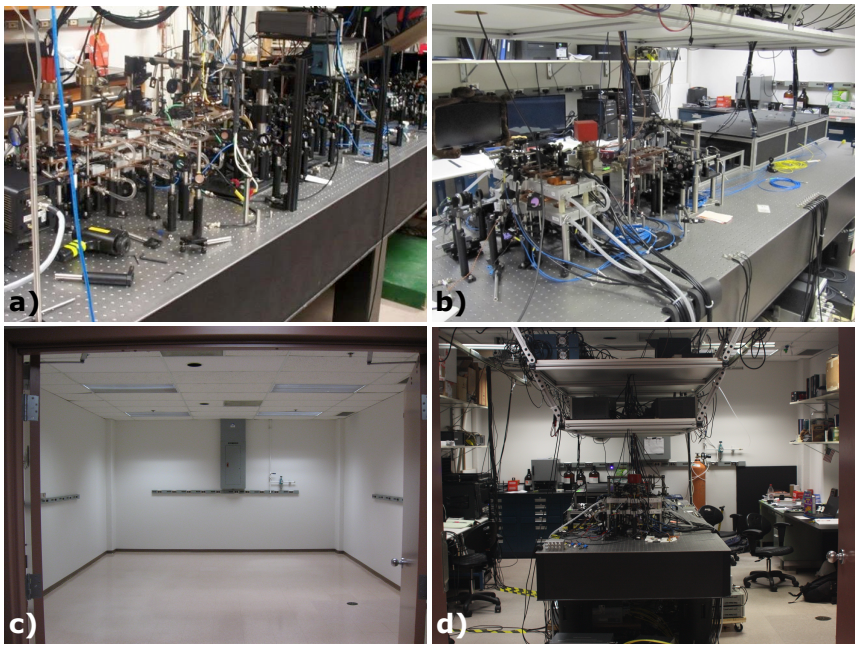

Figure 1.1: Side-by-side photographs of a) BEC 1 and b) BEC 2. c) A photograph of the lab on May 22nd, 2012, the day I moved into the new lab. d) A similar view of the lab on April 22nd, 2016, showing the current state of the system.

[31] and imaging [32] experiments discussed in more detail below.

Figure 1.1a) shows an image of our original BEC apparatus alongside a similar view of the new system shown in Fig. 1.1b). For the remainder of the thesis I refer to the original BEC system as BEC machine 1 (or BEC 1) and the new system as BEC machine 2 (or BEC 2). Construction on BEC 1 began in 2001 and it achieved BEC in the fall of 2005. I joined the group in 2009 and began assisting with experiments on that machine. The vortex manipulation and imaging studies described below were performed on BEC 1 with the help of Carlo Samson, Kali Wilson, and Joe Lowney.

In the fall of 2011 I began designing the new system while still working on BEC 1. I was given the keys to the new lab (Rm. 566) on May 22nd, 2012 and we achieved BEC in the new system on Dec. 27th, 2015. Figure 1.1c) and d) shows

side-by-side images of the lab on day 1 and at the time of writing this document. I have been building the new system primarily with the help of Jessica (Doehrmann) Myers and most recently Andrew Schaffer.

1.1 Background

1.1.1 Bose-Einstein condensation

A key idea in Einstein's 1924 paper is that for a system of identical, massive particles, the total number of particles must be finite. For an ideal gas of non-interacting atoms in a 3D harmonic trap, at temperature, T, the number of atoms in the BEC is given by:

$$N_{BEC} = N\left[1 - \left(\frac{T}{T_C}\right)^3\right]. \tag{1.1}$$

where N is the total number of atoms. This is, of course, an approximation, since a real gas of atoms will always have some interactions, but this form is sufficient for making a consistent set of measurements of the condensate parameters in our system. For a more detailed analysis see [33, 34].

The transition temperature T_C is given by:

$$k_B T_C \simeq 0.94\hbar\bar{\omega}N^{1/3} \tag{1.2}$$

where k_B is the Boltzmann constant, $\hbar$ is the reduced Plank's constant and $\bar{\omega} = (\omega_x\omega_y\omega_z)^{1/3}$ is the geometric mean of the harmonic trapping frequencies in the x, y and z directions respectively. The factor $0.94\hbar\bar{\omega}$ in the transition temperature is related to the geometry of the system.

In order to understand the effects of atom-atom interactions in a real gas, we rely on the GPE which is solved to determine the approximate dynamics of the wave

function of the condensate in the limit that the inter-particle separation is much greater than the s-wave scattering length, a.[2] The time-independent GPE, which is used to find the ground state wave function for an external potential V_{ext}, is given by

$$\mu\psi(\vec{r}) = \left(-\frac{\hbar^2}{2m}\nabla^2 + V_{ext}(\vec{r}) + \frac{4\pi\hbar^2 a}{m}|\psi(\vec{r})|^2\right)\psi(\vec{r}) \tag{1.3}$$

where $\psi(\vec{r})$ is the condensate wave function, μ is the chemical potential, m is the mass of the atom, $-(\hbar^2/2m)\nabla^2$ is the kinetic energy operator, and $\frac{4\pi\hbar^2 a}{m}|\psi(\vec{r})|^2$ is the mean field interaction energy.

In the limit of strong, repulsive interactions (which is the case for ^{87}Rb), the interaction energy in Eq. 1.3 is much larger than the kinetic energy term and thus the kinetic energy term can be neglected.[3] In this limit, the condensate density, $n(\vec{r}) = |\psi(\vec{r},t)|^2$, in rectilinear coordinates is:

$$n(x,y,z) = \begin{cases} \frac{\mu}{g}\left(1 - \sum\limits_{i=x,y,z}\frac{i^2}{R_{TF,i}^2}\right), & \text{for} \quad \sum\limits_{i=x,y,z}\frac{i^2}{R_{TF,i}^2} \leq 1, \\ 0, & \text{otherwise.} \end{cases} \tag{1.4}$$

The condensate density is parabolic with a semi-axis in the x, y and z direction given by the Thomas-Fermi radius,

$$R_{TF,i} = \sqrt{\frac{2\mu}{m\omega_i^2}}. \tag{1.5}$$

[2]The GPE is an approximation to the many-body Schrödinger equation that relies on the Hartree approximation of the many-body wave function. Although the GPE does not include finite temperature system effects, predictions of BEC dynamics using the GPE are very accurate. See [33] for a description of how the time-dependent GPE can be utilized to simulate BEC dynamics.

[3]This is known as the Thomas-Fermi approximation [33].

The chemical potential, μ, is given by

$$\mu = \frac{15^{2/5}}{2}\left(\frac{aN_{BEC}}{\bar{\ell}}\right)^{2/5}\hbar\bar{\omega} \tag{1.6}$$

where $\bar{\ell} = \sqrt{\hbar/m\bar{\omega}}$ is the mean harmonic oscillator length. Equations 1.5 and 1.6 relate the atom number in the condensate directly to system parameters and the Thomas-Fermi radius. The total atom number in the BEC is given by

$$N_{BEC} = \frac{15a}{\bar{\ell}}\left(\frac{mR_{TF,i}^2\omega_i^2}{\hbar\bar{\omega}}\right)^{5/2} \tag{1.7}$$

If the harmonic trap frequencies are known, a measurement of the Thomas-Fermi radius can be used to determine the atom number.

A conceptual condition for condensation is that a BEC occurs when the temperature of a gas of identical bosons is low enough that the mean spatial extent of the atoms determined by the thermal deBroglie wavelength, λ_{dB}, is comparable to the inter-particle separation.

This idea can be expressed mathematically in terms of the phase space density, ρ. Phase space refers to a multidimensional space which represents all the possible states of a system, and for a gas of identical bosons, phase space includes three spatial degrees of freedom and three momentum degrees of freedom. The phase space density encapsulates the spatial density and the temperature of the system into a single number. Phase space density is given by

$$\rho = n\lambda_{dB}^3 \tag{1.8}$$

where n is the number density and the deBroglie wavelength is given by

$$\lambda_{dB} = \sqrt{\frac{2\pi\hbar}{mk_BT}}. \tag{1.9}$$

In terms of the phase-space density, the quantum nature of a dilute-gas is relevant when the phase-space density, $\rho \sim 1$.[4]

In Ch. 5, I describe the measurement process for some condensate parameters in our system including trap frequency, atom number, and the transition temperature.

1.1.2 Vortices in BECs

As mentioned above, the concepts of superfluidity and Bose-Einstein condensation are intimately related. From a hydrodynamic perspective, a BEC can often be considered to be a minute drop of superfluid with a fluid velocity given by

$$\vec{\mathrm{v}}(\vec{r}, t) = \frac{\hbar}{m}\nabla\phi(\vec{r}, t) \tag{1.10}$$

where $\phi(\vec{r}, t)$ is the phase of the condensate wave function,

$$\psi(\vec{r}, t) = \sqrt{n(\vec{r}, t)}e^{i\phi(\vec{r},t)}, \tag{1.11}$$

and $n(\vec{r}, t) = |\psi(\vec{r}, t)|^2$ is the condensate density. Equation 1.10 implies that fluid motion in the BEC must be irrotational, since $\vec{\nabla} \times \vec{v} = 0$, except in the case of a quantized vortex which corresponds to a singularity in condensate phase, and the curl of the velocity field is infinite. At the point of singularity, the BEC density drops to zero, so the that wavefunction remains single-valued everywhere in space.

[4] As a point of reference, in his 1924 paper Einstein calculated that degeneracy would occur in a non-interacting gas in a box when $\rho = 2.612$

In addition, the condensate phase must change by an integer multiple of 2π around any closed surface in the fluid.

The fluid circulation, Γ, which is defined as the line integral around a closed loop of the velocity field in the fluid is given by

$$\Gamma = \oint \vec{v} \cdot d\vec{l}. \tag{1.12}$$

The fluid velocity at a fixed distance from the center of a single vortex in an infinite superfluid is

$$\vec{v} = \frac{\hbar q}{mr}\hat{\ell} \tag{1.13}$$

and the circulation around the vortex is

$$\Gamma = \oint \frac{\hbar q}{mr}\hat{\ell} \cdot d\vec{l} = \frac{h}{m}q \tag{1.14}$$

where h is Plank's constant, m is the mass of a single particle in the fluid and q is the circulation quantum number. Thus, a vortex in a superfluid has quantized circulation, where the quantum of circulation is h/m. The quantization of circulation is a direct consequence of the condensate phase and is a defining characteristic of a superfluid and was predicted by Osanger in 1949 [7].

The vortex core is defined as the line of zero density in the BEC with fluid circulating about the core. In an highly oblate BEC, where fluid flow is roughly confined to a plane, the vortex core forms a straight line through the condensate parallel to the axis of symmetry and fluid circulation about the core is either clockwise or counterclockwise. In our experiments, we choose to work with highly oblate BECs, as the vortex is easily distinguished from the surrounding fluid.[5]

[5]Vortices in an Abriskov lattice in a rapidly rotating BEC also have straight line cores. Rotating

The BEC density in the presence of a single vortex at the center of the condensate takes the form

$$n_{vortex}(r) = n_z(r) * \chi(r). \tag{1.15}$$

where r is the radial coordinate. Here I assume a cylindrically symmetric condensate (where z is the axis of symmetry), and only consider the integrated density along the axial direction, $n_z(r)$. $\chi(r)$ represents the vortex core profile and can be approximated by

$$\chi(r) = \frac{r^2}{r^2 + (\xi/\Lambda)^2} \tag{1.16}$$

where ξ is the condensate healing length and $\Lambda \approx 0.825$ is a constant which governs the slope of the condensate density near the core [36]. The healing length defines the length scale over which the BEC density returns from zero to its bulk density in response to a localized perturbation, and roughly corresponds to the radius of a vortex core. The healing length is related to the local density of the BEC by

$$\xi(r) = \frac{1}{\sqrt{8\pi a n(r)}}. \tag{1.17}$$

As Eq. 1.17 indicates, the healing length, and correspondingly the vortex core size is inversely proportional to the square root of the condensate density. In an inhomogeneous BEC, the vortex core size can vary over the extent of the condensate. In areas of high density, the vortex core size will be smaller than in areas of lower density. For reference, the healing length is $\sim$0.28 μm for typical BEC densities in our oblate traps in BEC 1.

---

the condensate ensures that the fluid flow is predominantly in a plane and individual vortices in the lattice form straight lines parallel to the axis of rotation [35].

1.2 Imaging vortices in a BEC

The ability to image vortices *in situ* is central to our investigation of vortex dynamics in BECs. The primary challenge in imaging vortices *in situ* is that the size of the vortex core in a trapped BEC is a few times smaller than the wavelength of light used to image the cloud, making direct imaging of vortices difficult.

Traditionally, imaging vortices in BECs has involved releasing the BEC from its trap and allowing the condensate to expand for a period of a few tens of milliseconds [28]. During this process the vortex core also expands to the point where it is easily resolvable. A drawback of this method is that the expansion process is destructive and results in an image of the condensate density at a single point in time. This method works well in harmonic traps where the condensate density in expansion is an accurate representation of the in-trap density.

It is possible to study dynamics using this technique but studies are limited to situations where vortex dynamics are repeatable. Measuring vortex dynamics in this way involves initializing a vortex distribution in a repeatable manner, and then imaging the expanded BEC after different evolution times. Since the expansion is destructive, a new BEC must be created for each point in the evolution. As an example, an earlier work from our group investigated the evolution of a vortex dipole with this technique [37].

While expansion imaging of vortices is the norm, it is certainly not the rule. Several groups have demonstrated *in situ* imaging of vortices in multicomponent BECs by filling vortex cores with a second atomic state [38]. The "filler" state increases the size of the vortex core and the vortex can be imaged with minimally destructive imaging techniques used for imaging bulk BECs [34]. However, interactions between the two states affects the vortex dynamics.

More recently, vortex dyamics have been studied by transferring a small fraction of atoms in the BEC into an untrapped state and imaging the untrapped fraction in expansion [39]. The remaining fraction of atoms stay trapped and vortex dynamics are uninterrupted by the imaging process. Dynamics of arbitrary arrangements of a few vortices have been imaged and this method seems to hold promise for more complex distributions. The main drawback of this technique is that the extracted fraction has low density and as a result, vortex core sizes are large compared to their trapped counterparts. While this enables vortex visualization for small numbers of vortices, there is some question as to whether this technique will be effective for large numbers of closely packed vortices, as is the case in quantum turbulence [40].

Our group has instead focused on the ability to resolve vortices in a trapped BEC directly, without altering the natural vortex core size. In 2015, our group demonstrated the first *in situ* images of bare vortex cores in a single-component BEC using a commercial objective with a numerical aperure (NA) of 0.2 [32]. Dark field imaging [41, 42, 34], a technique in which unscattered light from a probe laser is blocked by a mask and only light scattered into large angles contributes to the image, was used to isolate the vortex core signal from the bulk BEC. Using this method, vortices appear as bright spots on a dark background.

Figure 1.2 a)-c) shows a set of *in situ* images of a vortex lattice in a BEC with a 3:1 aspect ratio using the second iteration of our vortex imaging system. This iteration utilizes a more sensitive camera than was used in the previous study and a custom microscope objective with an NA = 0.25. We have also demonstrated the ability to take multiple (up to four) images of the same vortex lattice using this imaging system.[6]

[6]See Kali Wilson's PhD thesis for a detailed discussion of three imaging techniques and a numerical analysis of the vortex signal using the dark field approach [43]. Joe Lowney's thesis

Unfortunately, with the current imaging system, we have been unable to detect vortex cores *in situ* for BECs in the highly oblate traps desired for studies of vortex dynamics and 2D quantum turbulence (2DQT). Images d) and e) show the degradation of the vortex core signal as the BEC is transfered from a magnetic trap with an aspect ratio of 3:1 to a hybrid optical and magnetic trap with an aspect ratio of 4:1. We suspect that the increased density and corresponding decrease in the vortex core size hinders our ability to resolve a vortex core from the bulk BEC. Numerical analysis of the probe light intensity as it passes through a BEC with vortex supports the idea that the detected signal improves drastically as the vortex core size increases. In addition, moving to a higher NA optical systems will enable collection of scattered light and improve the vortex signal.

---

includes a discussion of the signal-to-noise issues that arise when trying to distinguish a weak vortex signal from the bulk BEC [44].

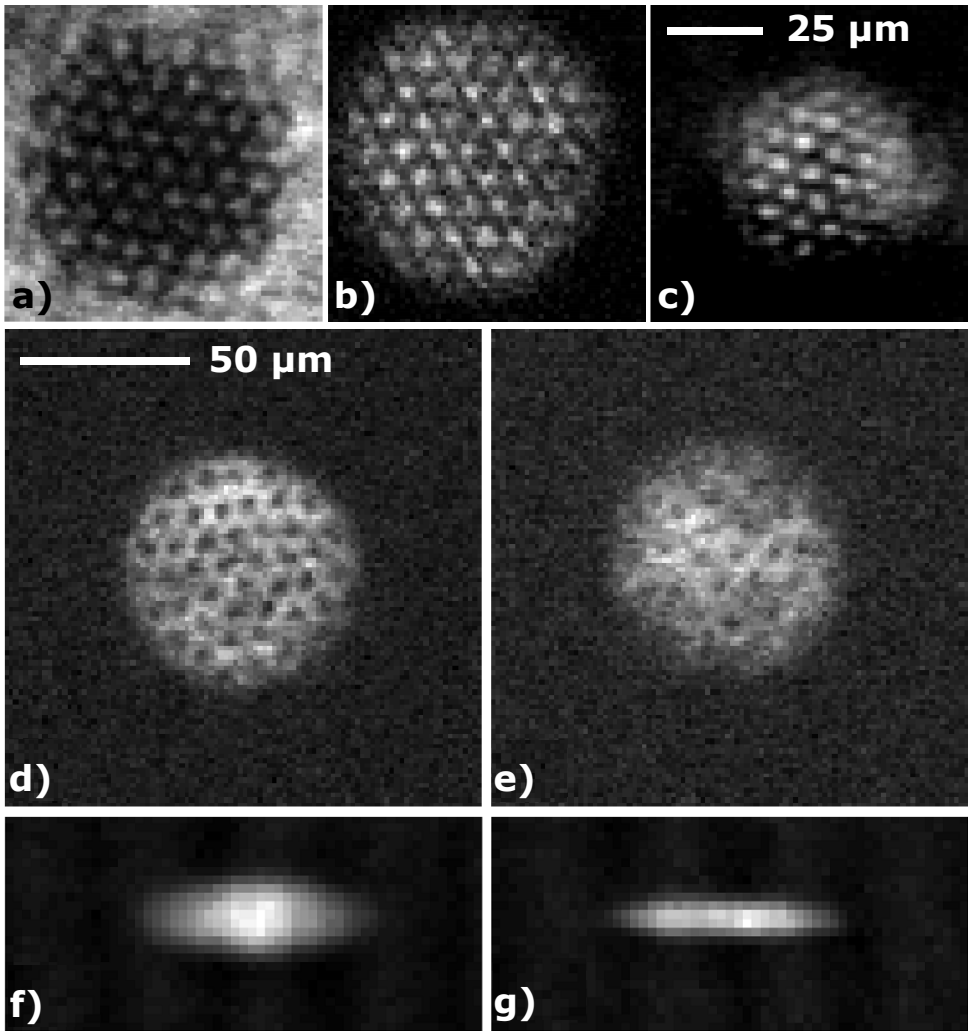

Figure 1.2: a)-c) 100μm×100μm *in situ* images of a vortex lattice in a 3:1 aspect ratio BEC from [43] using a) standard absorption imaging, b) Faraday imaging [45] and c) dark field imaging. d) and e) 140μm×140μm *in situ* Faraday images of a vortex lattice before and after loading into a weak hybrid trap. Corresponding phase contrast images showing the aspect ratio of the rotating BEC in the f) TOP trap (aspect ratio = 3:1) and g) in the weak hybrid trap (aspect ratio = 4:1).

1.3 Generating arbitrary vortex distributions

Conjugate to imaging vortex distributions *in situ* is the ability to create arbitrary arrangements of vortices in the condensate. In a recent study [31], we demonstrated

a new method for controllably creating and manipulating two vortices of opposite circulation using two blue-detuned laser beams sweeping through a BEC. In this technique, two blue-detuned lasers are focused onto the BEC at a position such that they perforate the BEC. The position of each beam is controlled electronically using a home-built scanning mirror system which used piezo-electric actuators to control the mirrors. Initially the beams are co-located slightly off of center of the condensate. At the start of the procedure, the beams simultaneously move laterally through the condensate and separate at constant velocity. The beam velocity is below the critical velocity for vortex dipole shedding. For appropriate sweep velocities, two vortices of opposite circulation are created with a single vortex pinned to each beam. Subsequent motion of the blue detuned beams allows us manipulate the final position of one or both vortices. Figure 1.3 shows a diagram of the creation process along with several images of the BEC during the process. We plan to extend this method to upwards of 10 vortices, using computer controlled holographic optical tweezers [46, 47].

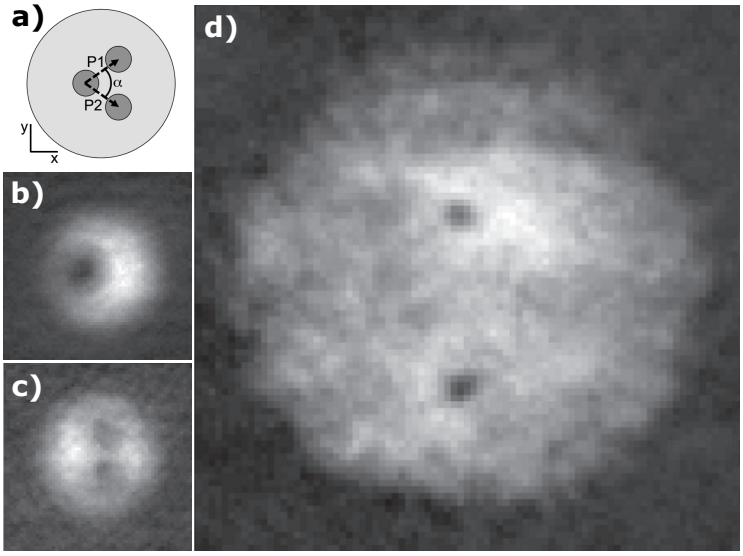

Figure 1.3: a)-c) Images of the procedure for controllably creating two vortices of opposite circulation in the BEC. d) Image of the BEC in expansion after the pinning potentials have been released showing the two vortices in the location of their respective pinning beams [31].

1.4 Designs for BEC 2

In this section I discuss some of the design choices for our system. Many of the designs have not been implemented (i.e. imaging with high numerical-aperture objectives, weak radial trapping frequencies, homogeneous trapping geometries, high quantum efficiency cameras, etc.); current progress on implementing these designs is discussed in Ch. 7.

1.4.1 Thin science cell and high-NA imaging objectives

The (two) science cell(s) in BEC 2 are Starna Cells, 10-mm wide by 5-mm tall, quartz flourimetry cuvettes which are attached directly to our 3D MOT chamber. With respect to standard BEC experiments, this is an extremely thin cell design. We have chosen to use a thin cell as this enables high-NA imaging from the top

and bottom sides of the cell with commercially available, short working distance microscope objectives. Custom, long working distance objectives suitable for use with standard vacuum chambers are very costly and require much larger optics that might inhibit optical access. The designs for the vacuum chamber are discussed in detail in Ch. 2.

Higher NA imaging objectives (NA ~ 0.4) will allow us to collect more refracted light and will result in an improved vortex core signal over our current *in situ* imaging system. In addition, higher NA objectives will allow smaller optical tweezers and thus more vortices can be created controllably in the condensate.

1.4.2 Weak radial trapping frequencies for larger healing length

As discussed in Sec. 1.1.2, the vortex core size is inversely proportional to the square root of the local BEC density. For the same number of atoms (N$\sim 2\times 10^6$), weaker radial trapping frequencies result in lower density BECs and thus a larger vortex core size. We plan to trap atoms in highly oblate (aspect ratio = 11:1) geometries with a radial trapping frequency near $\sim 2\pi\times 3$ Hz. At this trap frequency, $\xi \sim 0.4$ μm, a factor of 1.7 larger than in our highly oblate traps in BEC 1. In conjunction with higher NA objectives, we expect this will improve *in situ* vortex signal substantially.

1.4.3 Harmonic traps with a well-defined magnetic field axis

Currently we create BECs in our system using a Time-averaged Orbiting Potential (TOP) trap [48], a standard in BEC experiments. While this provides a reliable geometry for making condensates, the bias field direction orbits in time and makes *in situ* imaging more difficult. We are currently working on developing alternative all-magnetic, harmonic trapping geometries with well-defined magnetic fields. One

of these trap geometries, known as the gravito-magnetic trap, is discussed in Ch. 6.

1.4.4 Combined optical-magnetic hybrid traps

Ultimately we plan to move towards cooling atoms to degeneracy in a hybrid-optical magnetic trap. As in BEC 1, hybrid optical-magnetic traps will be used to create oblate trapping geometries for studies of 2D vortex dynamics. Optical traps also offer the flexibility of moving to flat-bottomed or box potentials that may be investigated in the future.

1.5 Format of this dissertation

The purpose of this dissertation is to serve as a technical user's manual for the new apparatus. To that end, I focus on detailed descriptions of the apparatus including our design choices, construction procedures and methods for diagnosing the system but have not included in-depth discussions of the experimental techniques used. The references in the text should help point the reader to appropriate background material.

Chapters 2 through 5 give a description of the new apparatus. Chapter 2 focuses on the vacuum chamber with attention to the science cells that have been designed for *in situ* imaging. Chapter 3 discusses the lasers systems used to prepare a cold ensemble of atoms prior to condensation in a magnetic trap. Chapter 4 covers the magnetic field systems used for transferring atoms from the MOT to the science cells on either side of the vacuum chamber and the magnetic fields used to produce the condensate. Chapter 5 gives an overview of the evaporation procedure and some of the measurements for characterizing the BEC.

In Chapter 6, I discuss our implementation of a gravito-magnetic (GM) trap that

utilizes the magnetic field system discussed in Chapter 5. The GM trap provides a simple way of generating a range of trap geometries from spherical to oblate with a well defined magnetic field axis aligned with the imaging system axis. At the time of writing, we have demonstrated the loading of a nearly pure BEC into a spherical GM and we are hopeful that we will be able to us the GM trap for studies of 3D condensates.

Finally, in Chapter 7, I discuss some of the planned additions that will make the system fully functional. I also discuss a few lessons we have learned during the building process that may be beneficial for future students designing similar experiments.

CHAPTER 2

The vacuum chamber

The vacuum chamber is the heart of our apparatus and was the first piece of the system to be designed. Many of the designs for the rest of the apparatus reflect the vacuum geometry (i.e. the magnetic transfer system, the shuttle mount, 2D MOT beams etc.).

The vacuum chamber in BEC 2 is a compact, two-chamber, single-pump system; a diagram of the chamber is shown in Fig. 2.2. In this chapter I give a detailed description of the vacuum chamber in BEC 2. In Section 1, I give an overview of the important experimental requirements that govern the chamber design. Next, in Section 2, I describe the main components of the vacuum chamber including the glass 2D MOT cell, the differential pump tube, the stainless steel chamber that houses the vacuum pump and the glass 3D MOT/science cell where we create our BECs. Finally, in Section 3, I give a quick calculation of the expected pressures in our chamber and describe the initial bakeout procedure.

2.1 Design considerations

The four main design considerations for BEC 2 are listed below:

1. **High numerical aperture imaging with commercial objetives:** A number of groups have demonstrated high resolution imaging of ultra-cold atoms. Typically, these types of experiments have chosen to use standard vacuum geometries and have either used *in vacuo* optics [49, 50] or designed custom,

high-NA, long-working distance microscope objectives to fit their vacuum geometries [51, 52, 53, 54]. *In vacuo* optics enable very high NA imaging systems, but must be vacuum-compatible and bakeable and in some cases can limit optical access. Objectives placed outside the vacuum chamber allow greater optical access and do not require vacuum compatibility but typically have lower NAs and the thick (>2 mm) windows on standard vacuum cells introduce significant spherical aberration that must be accounted for in the objective design. In either case, optical design and fabrication of a suitable objective can be very costly.

An alternative to this approach is to use commercial objectives and tailor the vacuum geometry to fit the objective. Salim *et al.* [55] have demonstrated high-resolution imaging of cold atoms on a chip based cold atom system.

Recently, our group demonstrated *in situ* imaging of vortices in a BEC using a commercial objective with an NA = 0.2 on BEC 1 [32] and subsequently with a custom objective with an NA=0.25 on the same system [43]. However, as discussed in Ch. 1, we suspect that *in situ* vortex imaging in highly-oblate traps will require imaging systems with NA > 0.3.

The science chamber in BEC 2 was designed allow high resolution imaging using commercially-available, biological microscope objectives (with NA > 0.4). Figure 2.1 shows a diagram and a photograph of the science cells in BEC 2, which are 5-mm tall quartz cuvettes with 1.25-mm thick walls. Accounting for the magnetic field coils and associated mounting structure (Ch. 5), we anticipate being able to use near-infrared (NIR) microscope objectives, with ∼15-mm working distances, designed to work with ∼1-mm biological cover slips. The science cells are discussed in more detail in Section 2.2.4.

2. **Dual species experiments:** The vacuum chamber in BEC 2 contains both Rubidium and Potassium sources attached to the 2D MOT cell. By incorporating Potassium sources into the chamber, we open up the possibility of studying vortex dynamics in a BEC with tunable interactions at low bias field strengths.[1] A more long term goal of the apparatus is to study the development of turbulence arising from the counterflow of counter-propagating condensates [58]. The 2D MOT cell is discussed in detail in Section 2.2.1.

3. **Compact vacuum/optical system:** In order to accommodate two-species experiments on a single optical table, we have designed a compact vacuum chamber that utilizes a single non-evaporable getter (NEG) pump. The chamber layout and pump are discussed in section 2.2.

4. **Two BECs for the price of one:** The low pressure side of the chamber is composed of an octagonal MOT loading chamber and two quartz science cells that are attached directly to the MOT chamber. Figure 2.1 shows an image of the 3D MOT chamber and the identical science cells attached to either side. With two science chambers, we have the ability to set up separate experiments that access the same MOT load and magnetic transfer equipment and individual experiments can be worked on in parallel.

[1] ^{39}K has several known Feshbach resonances that occur at bias field strengths below 100 G with widths ∼10 G [56]. In constrast, the widest observed resonances in ^{87}Rb occur at bias strengths near ∼1000 G with widths of ∼0.2 G.[57]

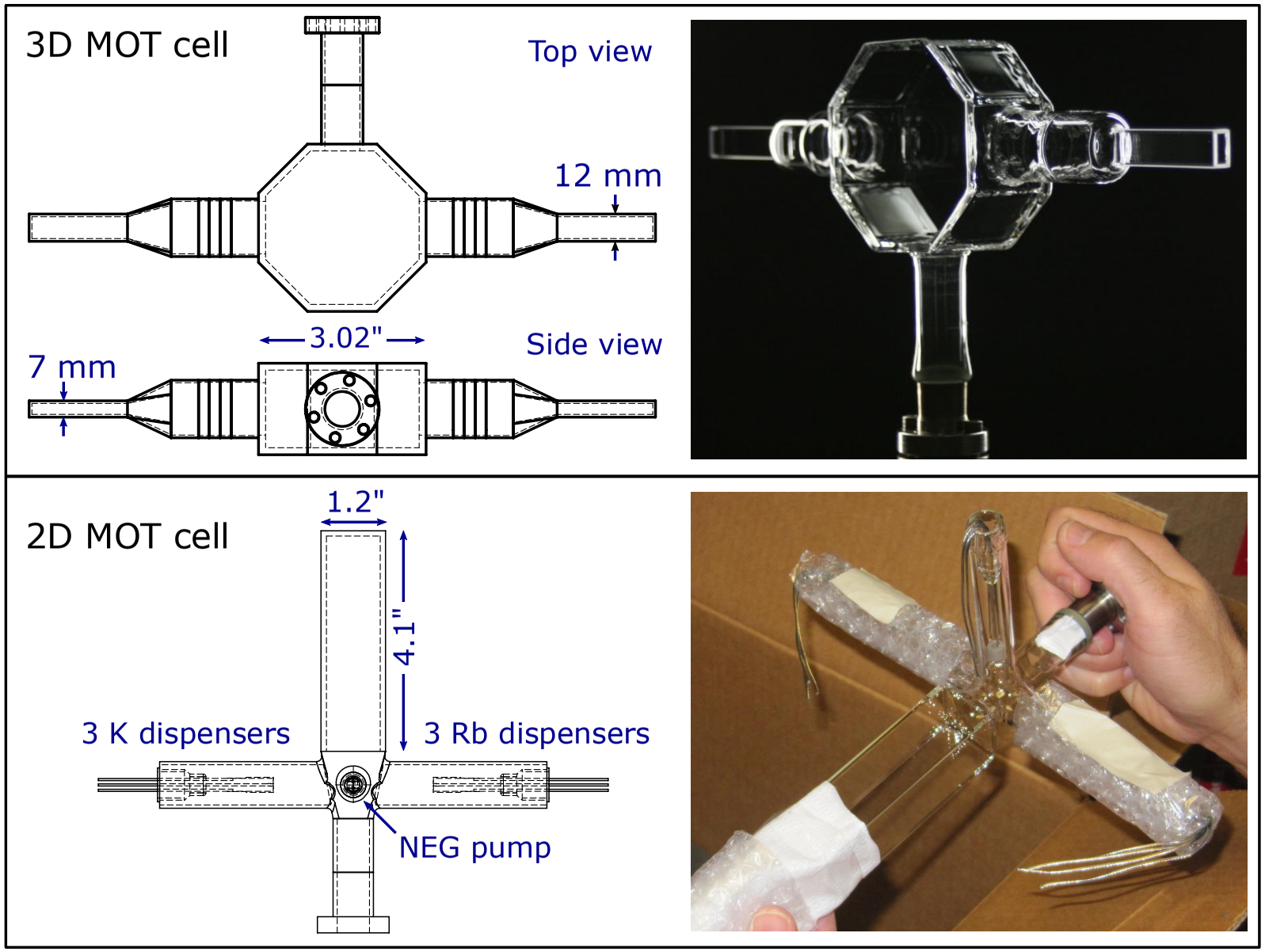

Figure 2.1: CAD daigrams of the 2D and 3D MOT cells and corresponding photographs.

2.2 Vacuum chamber

The vacuum chamber in BEC 2 has four main components which are shown in Fig. 2.2 and described in detail below. These are 1) the 2D MOT cell; 2) the 6-way cross; 3) the vacuum pump and the stainless steel pump housing; and 4) the 3D MOT/science chamber.

2.2.1 2D MOT cell

The 2D MOT cell consists of a 1-inch by 4-inch quartz cuvette which has been fused onto a Pyrex glass-metal seal by Ron Bihler at Precision Glassblowing in Centennial, Colorado. Three Pyrex arms are attached directly to the glass-metal seal. The arms contain a set of 3 Rubidium dispensers, a set of 3 K dispensers and a non-evaporable getter pump (NEG).[2] Figure 2.1 shows a CAD drawing of the 2D MOT cell.

The dispensers in the 2D MOT cell are SAES Alkali Metal Dispensers. The dispensers are composed of a small stainless steel pouch attached to a filament which have been filled with a mixture of a getter material (mostly Zirconium) and Rubidium (or Potassium) Chromate powders. Heat is applied to the dispenser by running current through the filament, which drives the following reaction:

$$Rb_2CrO_4 + Zr \rightarrow ZrCrO_4 + 2Rb \tag{2.1}$$

[2]NEG pumps work by the sorption of gas molecules onto a highly-porous surface. Typically, NEG pumps are made of materials that readily form stable compounds with active gases (such as H, O_2, N_2, CO_2, etc) so that once a molecule has been adsorbed onto the surface of the pump it can diffuse into the bulk material and is effectively removed from the chamber. Inert gases and hydrocarbons are much less reactive and are pumped more slowly.

Once the bulk material is saturated the pump rate decreases exponentially. This is typically the case when using the NEG pump for the first time as they are often exposed to air during the vacuum assembly process. Absorbed gas can be expelled by heating and NEG pumps often require an activation process once the chamber has reached a sufficient level of vacuum.

Since we operate at very low pressures, we expect that the NEG pumps should keep their initial pump rates once activated. The NEG pump in the 2D MOT cell has not been activated, but remains an option if we decide further pumping is needed in the future.

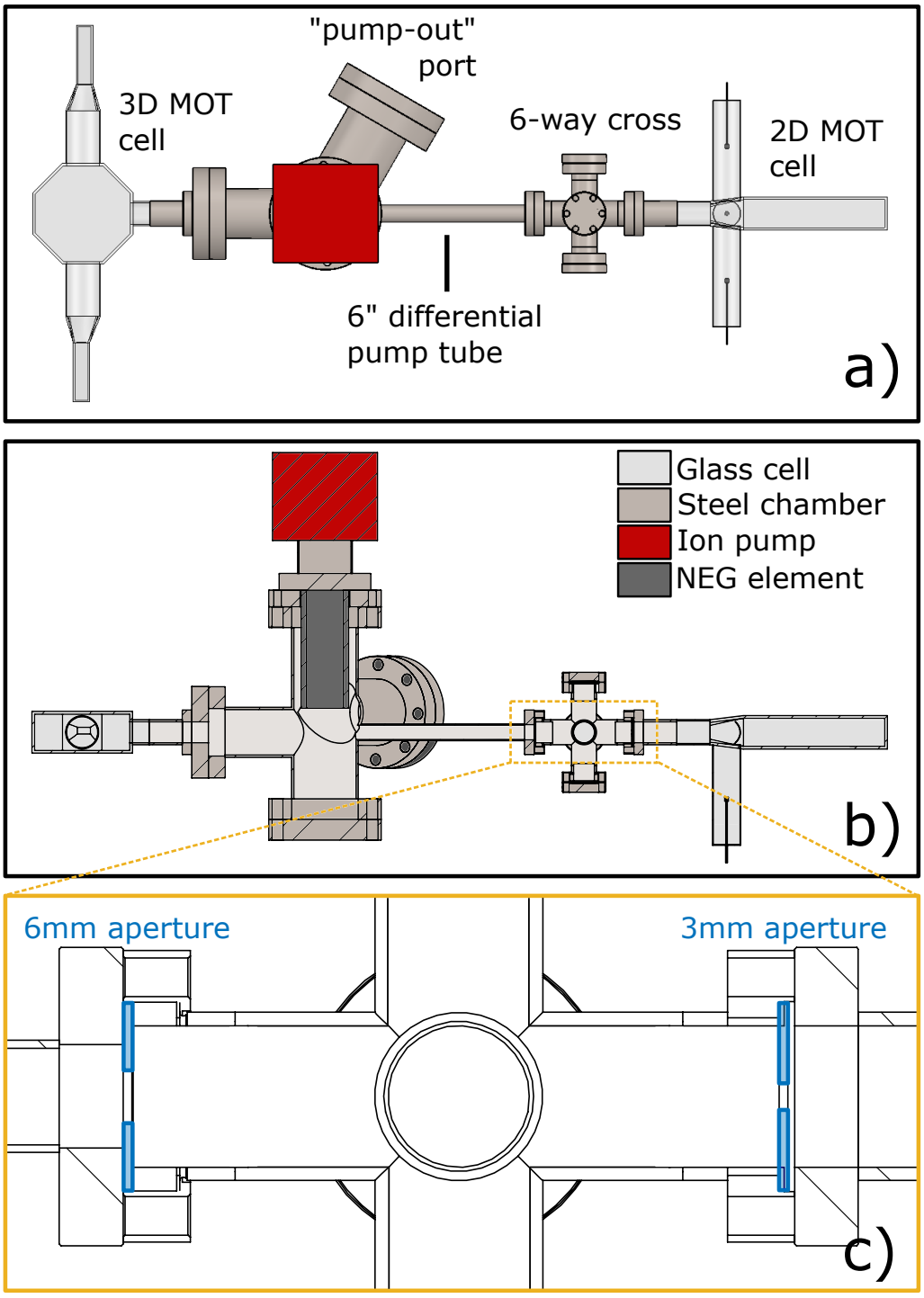

Figure 2.2: a) Overhead view and b) corss-section view of the vacuum chamber. c) shows a blown-up cross section of the 6-way cross, highlighting the two copper apertures that separate the high pressure and low pressure sections of the vacuum chamber.

and releases Rb into the chamber. The steel pouch is coated with NEG material which helps to adsorb any active gases that are released during the heating process. We typically run our Rb dispenser at 3.17 A. At this current we release enough Rb to load 3D MOTs with about 3-5$\times 10^9$ atoms in 30-45 sec and have reasonable background gas limited magnetic trap lifetimes ($\sim$150 sec).

The 2D MOT cell is used to create the cold beam source (the 2D MOT is discussed in Section 3.2) that we use to load our 3D MOT. Creating the 2D MOT requires a relatively high partial pressure of Rb ($\sim 10^8$ Torr) so we separate the high pressure 2D MOT cell from the rest of the chamber with a pair of pinholes and a differential pumping tube (discussed below). The 2D MOT cell is attached to the rest of the chamber via the 1.33" ConFlat (CF) flange on the glass-metal seal.

2.2.2 6-way cross

The 6-way cross separates the relatively high pressure 2D MOT chamber from the lower pressure pump and science chambers using a pair of pinholes machined into a pair of copper gaskets as shown in Fig. 2.2. A 3-mm diameter pinhole separates the cross from the 2D MOT cell and a 6-mm diameter pinhole separates the cross from the low pressure side of the chamber. The 3-mm pinhole is an integral part of the 2D MOT, and acts as a low-pass velocity filter for atoms in the cold beam. The filtering aspect of the pinhole is discussed in Section 3.2.

Three (north, south and bottom) ports of the cross are fitted with vacuum compatible windows. We had originally intended to use the windows for 2D MOT diagnostics, but so far have not used this feature.

2.2.3 Differential pump tube and main pump housing

The main section of the vacuum chamber is a custom stainless steel chamber that houses the main pump, includes a pump-out port for the initial stages of pumping and connects the high and low pressure sides of the chamber via a 6" long 11-mm inner diameter tube.

The body of the chamber is a 2.75-inch CF nipple that houses our main vacuum pump: a SAES NexTorr D 200-5 pump. The NexTorr pump is a compact, high capacity, high speed pump designed for use in UH vacuum systems. The NexTorr pump combines a large NEG element which serves as the primary pump and a small, ancillary (6 L/s) ion pump that removes noble gas species and hydrocarbons not pumped by the NEG element and provides a pressure reading in the chamber.

After a series of high temperature bake-outs (described in Section 2.3) the NEG pump was activated. Following the activation of the NEG element, the pressure guage on the ion pump controller read P= 1×10^{-10} Torr, which is the lower limit of the pressure readout. Based on lifetime measurements of atoms in the magnetic trap (see Section 5.3.4) and the pressure calculations in Section 2.2.5, we suspect that the pressure in the main chamber is $\sim1\times10^{-11}$ with a slightly lower pressure in the science cell.

2.2.4 3D MOT/science cells

The 3D MOT cell, which was also made by Precision Glassblwoing, is certainly the most unique aspect of our chamber. The body of the cell is a 1.65-inch high Pyrex octagonal prism with 1.25-inch sides. Figure 2.1 shows a diagram and a photograph of the 3D MOT cell. The top, bottom and four of the side windows are used for the 3D MOT laser cooling beams. The fifth side is used for a glass-metal seal

and connects the 3D MOT cell to rest of the chamber. The window opposite the glass-metal seal is used for imaging atoms in the 3D MOT location and for MOT alignment purposes. The two quartz science cells are attached to the remaining two windows via 1-in diameter, 2.1-inch long arms.[3] The two science cells are separated by ∼11 inches and we use an all-magnetic transfer procedure for transferring atoms from the octagonal MOT load chamber to either of the two science cells.

The science cells are externally AR coated on all five sides of the cell to avoid some of the interference fringes associated with using coherent imaging light. Unfortunately, the coating was damaged during the assembly of the cell and has, in some locations, made imaging the atoms in our science cell difficult.

2.2.5 Vacuum calculations

For the conditions in our chamber, the dynamics of the gas inside the chamber are in the molecular flow regime which occurs when the mean (collision) free path of atoms in the chamber is larger than the size of the chamber. For chambers on the order of a few centimeters in size, this occurs at pressure well below 10^{-3} Torr. In this regime atoms can essentially be thought of as billiard balls bouncing around inside the chamber and features of the chamber than restrict the motion of atoms (like thin tubes or corners) serve to isolate sections of the chamber and create a pressure differential. If the pumping speed, S_0, at a particular location in the chamber (the NexTorr pump inlet for example) is known, the pumping speed at any other point

[3]The arms that attach the quartz science cells to the body of the 3D MOT chamber are actually made of a series of five smaller sections of tubing made of different glasses. The thermal expansion coefficients of Pyrex and quartz differ enough that the firing process prohibits attaching the quartz cuvettes directly to the Pyrex body. The smaller sections of tubing create a graded thermal expansion coefficient along the arm and allow the cuvettes to be attached to the octagonal body.

in the chamber, S, can be calculated using

$$\frac{1}{S} = \frac{1}{C} + \frac{1}{S_0} \tag{2.2}$$

where C is the conductance in [L/s] which is determined by the chamber geometry.

The conductances for an aperture and a tube in the molecular flow regime are given by

$$C_{aperture} = \frac{3.81D^3}{L}\sqrt{3k_BT/M} \quad \text{[L/s]} \tag{2.3}$$

$$C_{tube} = 3.7A\sqrt{3k_BT/M} \quad \text{[L/s]} \tag{2.4}$$

where D and L are the diameter and length of the tube, A is the area of the aperture, T is the temperature of the chamber in Kelvins, k_B is the Boltzmann constant and $M = 85.4$ amu is the molecular weight of the gas.[4] For a complicated chamber geometry, the total conductance is just the sum of the individual section conductances in parallel ($1/C_{chamber} = 1/C_1 + 1/C_2 + 1/C_3 + ...$).

2.2.6 More information

Lab notebook #1 pgs. 22-48 and 99-103 contain annotated drawings of the vacuum chamber and details about the bake-out process.

2.3 Chamber construction and bakeout

Achieving the ultra-high vacuum conditions necessary for BEC requires careful preparation of the vacuum chamber. Typically this involves a "bakeout", where the chamber is thermally isolated from the room and heated to a few hundred degrees C,

[4] The chamber can be decomposed into a series of tubes and apertures.

which is intended to free any substance that has been adsorbed onto the walls of the chamber (primarily water). Once adsorbed materials have been freed from the walls of the chamber, they can be removed with an external pump. Without a cleaning and bakeout process adsorbed material would slowly desorb and compromise the quality of vacuum.

For BEC 2 we chose to do a two step bakeout process which involved a 350°C bakeout of the metal components of the chamber and a second, 125°C bakeout after the glass components had been attached. Our assembly and bakeout procedures are detailed below.

2.3.1 Chamber assembly

Since the stainless steel components were delivered sealed from the factory, we decided not to clean the parts prior to assembly.[5] The metal components of the vacuum chamber were wiped down with methanol and all knife edges and copper gaskets were checked for dents or nicks which could lead to leaks. Silver plated bolts were used to prevent threads from seizing to the chamber during the bakeout in the event that we ever need to make changes to the chamber in the future. During assembly, powder-free latex gloves were worn to avoid contaminating the clean components.

Once the metal components of the chamber were assembled, the chamber was connected to a Varian Trubo-DRY 70 pumping station for the initial pumping.[6] For

[5]Dirty vacuum components can be cleaned in an ultrasonic bath with soap, washed off with water and then cleaned with alcohol in the ultrasonic bath. Individual components can also be pre-baked in a clean oven prior to assembly which can speed up the bakeout process.

[6]The Turbo-DRY 70 is a oil-free turbo pump backed by a diaphragm pump and can operate from atmospheric pressure down to 1x10^{-6}Torr. This pump is shared with Poul Jessen's group and has been used to create the initial vacuum in most of the labs on our hallway. The turbopump module has an ion gauge and belows attached, but the bellows have been contaminated with Cesium in the past. The user's log on the pump should be kept up to date and it may be worth checking with the previous user before attaching to a clean system. That said, the pump has worked very well for us in the past and after a period of about a day of pumping we have routinely been able

the high temperature bake CF blanks were placed in the locations where glass components would be attached later. Before pumping we wrapped the chamber in heater tape and attached thermocouples in various locations to monitor the temperature during the bakeout.

2.3.2 Chamber bakeout

The initial bakeout lasted roughly three weeks. During the bakeout the average temperature of the thermocouples placed around the chamber was ∼278°C. At the end of the bakeout we achieved a base pressure of 4.8x10^{-8} Torr. The chamber was returned to room temperature over a period of two days so as not to damage any of the vacuum seals by abruptly cooling the chamber and the turbopump was turned off. Before installing the 2D and 3D MOT cells and the windows on the 6-way cross, the chamber was vented to nitrogen above atmospheric pressure in order to prevent water vapor from adsorbing to the chamber walls.

Once all the glass components were attached we pumped out the chamber and set up for the second, low temperature bakeout. All six dispensers were degassed prior to the bakeout and rubidium was detected in the chamber by the attenuation of a probe laser. The second bakeout lasted a little over a month during which the average temperature of the thermocouples was ∼130°C and the chamber reached a final pressure of ∼1.7x10^{-8} Torr.

Immediately following the second bakeout the NEG element in the NexTorr pump was activated and the ion pump was turned on. After a full day of pumping the gate valve was closed and the turbopump was shut off. The pressure reading at the end of the day on March 3, 2013 was $P < 1 \times 10^{-11}$ Torr, indicating the pressure

to achieve base pressures of 5x10^{-7} before baking. Details on how to operate the turbo pump are given in Appendix B.

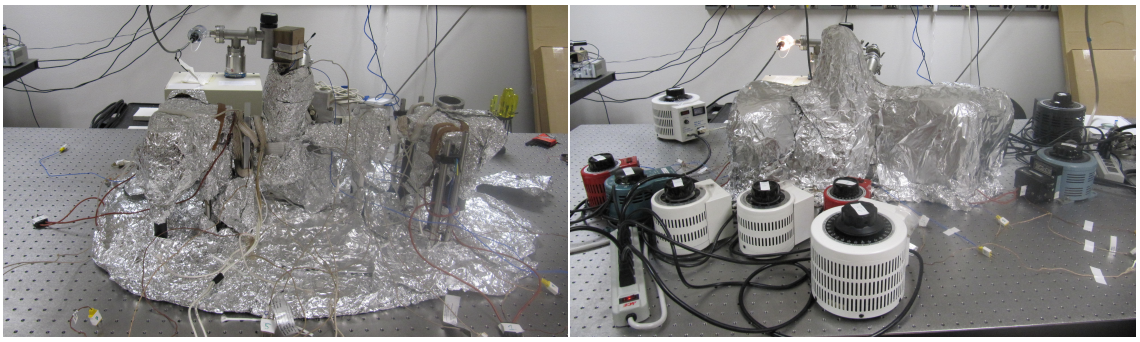

Figure 2.3: The physics turkey: Two images showing the vacuum chamber in preparation for (left) and during (right) the low temperature bakeout. The left photograph shows heater tape and a number of thermocouples in place before a final layer of insulation is added. In addition, the NexTorr ion pump magnets have been removed and the turbopump is attached to the chamber. The photograph on the right was taken during the bakeout and shows the variacs used to power the heater tape.

in the chamber was below the lower limit of ion pump gauge.[7] Figure 2.3 shows photograps of the chamber during the high temperature bakeout with plots of the pressure and temperature during the bakeout in Fig. 2.4.

[7]The NexTorr pump controller was recalled a few months after we finished our second bake and we sent the controller back to the manufacturer for a firmware upgrade. One of the changes following the firmware upgrade was the lower limit on the ion gauge reading which is now $P_{LL} = 1 \times 10^{-10}$ Torr.

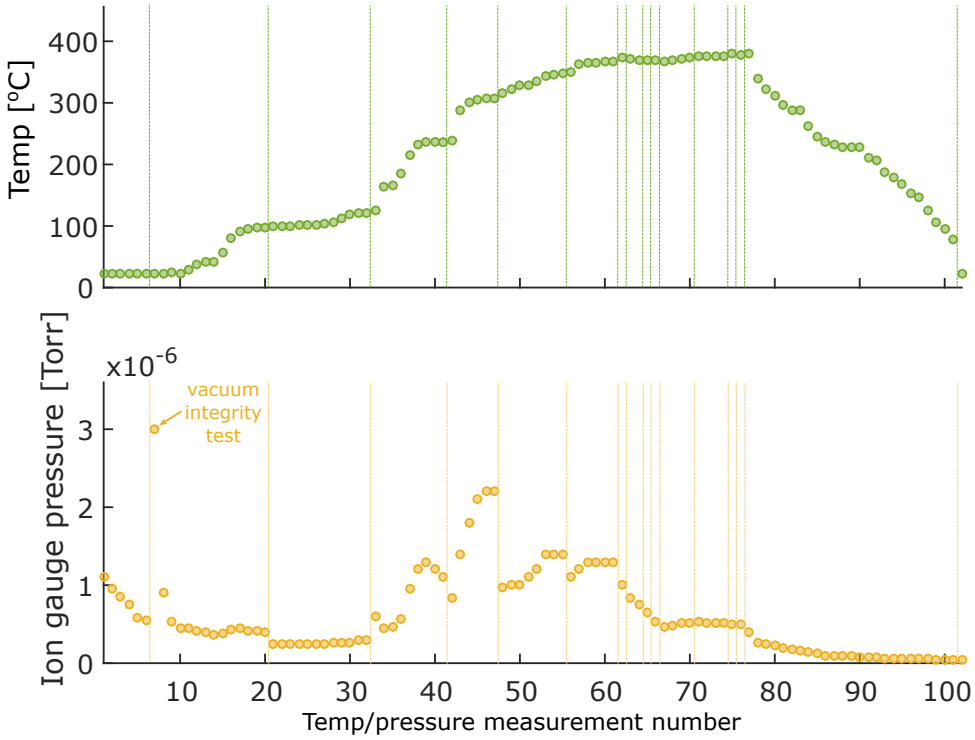

Figure 2.4: Plots of the maximum chamber temperature (top) and pressure (bottom) during the high temperature bakeout of the stainless steel vacuum components. Dotted lines in the figures indicate breaks between days during the ∼3 week bakeout. As the temperature in the chamber is increased over the coarse of a day, material adsorbed onto the chamber walls is released and the pressure rises. As the temperature settles, the released material is pumped out and the pressure drops.

CHAPTER 3

Lasers and Laser Cooling

A Magneto-optical trap (MOT) provides a way to create a cold, localized sample of atoms inside a vacuum chamber; the MOT is used as a starting point for nearly all cold-atom experiments. In this chapter I briefly discuss the configuration of a standard MOT and then describe in detail its implementation in BEC 2. Section 1 provides a description of the laser systems used to generate the MOT light, section 2 gives an overview of 2D MOT systems and describes the 2D MOT setup in BEC 2 and section 3 describes our 3D MOT and the process for transferring atoms from the 3D MOT into the magnetic trap.

3.1 Magneto-optical trap

Laser cooling and the magneto-optical trap (MOT) refer to a set of experimental techniques developed primarily in the 1980s [59, 60, 61, 62] with which a gas of atoms at room temperature (or higher) inside a vacuum chamber can be cooled to temperatures on the order of a few hundred microKelvin (or lower) using laser light, and simultaneously spatially confined. Since its development, the MOT has become the workhorse of modern atomic physics experiments. The standard configuration for a MOT consists of three orthogonal and intersecting pairs of counter-propagating laser beams. Atoms in the MOT are cooled by selective scattering of light from MOT laser beams whose propagation direction opposes the atomic motion. This is accomplished by tuning the beams to the red of an atomic transition. An atom

moving towards one of the MOT beams sees a Doppler shift in the frequency of the light closer to the atomic resonance frequency and scatters preferentially from that beam.

A spherical quadrupole magnetic field, typically created by a pair of anti-Helmholtz coils, provides a magnetic field gradient where the point at which the magnitude of the magnetic field, $|\vec{B}|$, is zero coincides with the intersection of the laser beams. The effect of the magnetic field is to add a spatial dependence to the atom-photon scattering rate (via the Zeeman shift), so that atoms feel a restoring force towards the center of the MOT. Figure 3.1 shows a diagram of a standard six beam MOT.

The momentum imparted by the absorption of a single photon from one of the MOT beams is small, so the MOT beams must interact with an atom repeatedly for cooling to be effective. For a more detailed discussion of MOT physics see [63, 64]. For an atom with nuclear spin, optical pumping to internal states other than the one accessed by the cooling laser halts the cooling process. In this case, one or more "repump" beams is required to return the atom to a state that can scatter light from the cooling beams. In ^{87}Rb, for example, a repump beam is required.

3.1.1 Lasers

Fig. 3.2 shows a diagram of the $5^2S_{1/2}$ to $5^2P_{3/2}$ transition in Rb from [65]. We use laser light tuned close to the $|5^2S_{1/2}, F = 2\rangle \rightarrow |5^2P_{3/2}, F' = 3\rangle$ transition for our cooling beams and light tuned to the $|5^2S_{1/2}, F = 1\rangle \rightarrow |5^2P_{3/2}, F' = 2\rangle$ transition for our repump beams.

We use a set of four 780-nm, single-mode diode lasers locked to ^{87}Rb transitions to provide the cooling light for the 2D and 3D MOTs. We amplify the cooling and

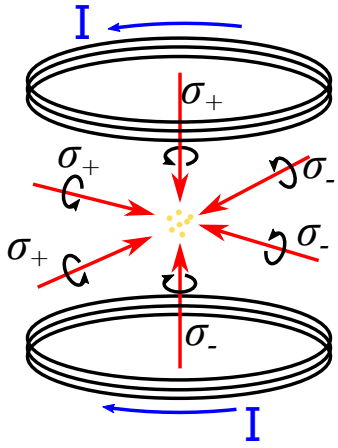

Figure 3.1: A typical six-beam MOT arrangement. A spherical quadrupole magnetic field, which is created by a pair of anti-helmholtz coils (dark circles), provides a spatially dependent energy shift for atoms (yellow dots) in the linear region of the field. The arrows indicate the direction of current, I, in the quadrupole coils. Three orthogonal pairs of circularly polarized laser beams (red arrows) provide a damping force, cooling the atoms in the region of intersection. Here the polarization of each beam (σ_+ or σ_-) is defined with respect to the propagation direction of the beam. Typically, MOTs can cool atoms to temperatures of a few μK to a few hundred μK.

repump light using two 2-W, 780-nm tapered amplifiers. The details of the tapered amplifier systems are discussed in section 3.1.2.

Separate cooling and repump lasers are used for the two MOTs so that the detunings of the 2D and 3D MOTs can be adjusted independently. One cooling laser and one repump laser are electronically stabilized to Rb reference cells and serve as the master lasers for our system; the remaining two lasers are injection locked to the master lasers. The cooling and repump master lasers are use to operate the 2D MOT and the slave lasers are used for the 3D MOT.

The two master lasers are home built external cavity diode lasers (ECDLs) [66] that are locked to ^{87}Rb transitions via saturated absorption and polarization spectroscopy techniques. Figure 3.3 shows a top view drawing and a photograph of one of our EDCLs.

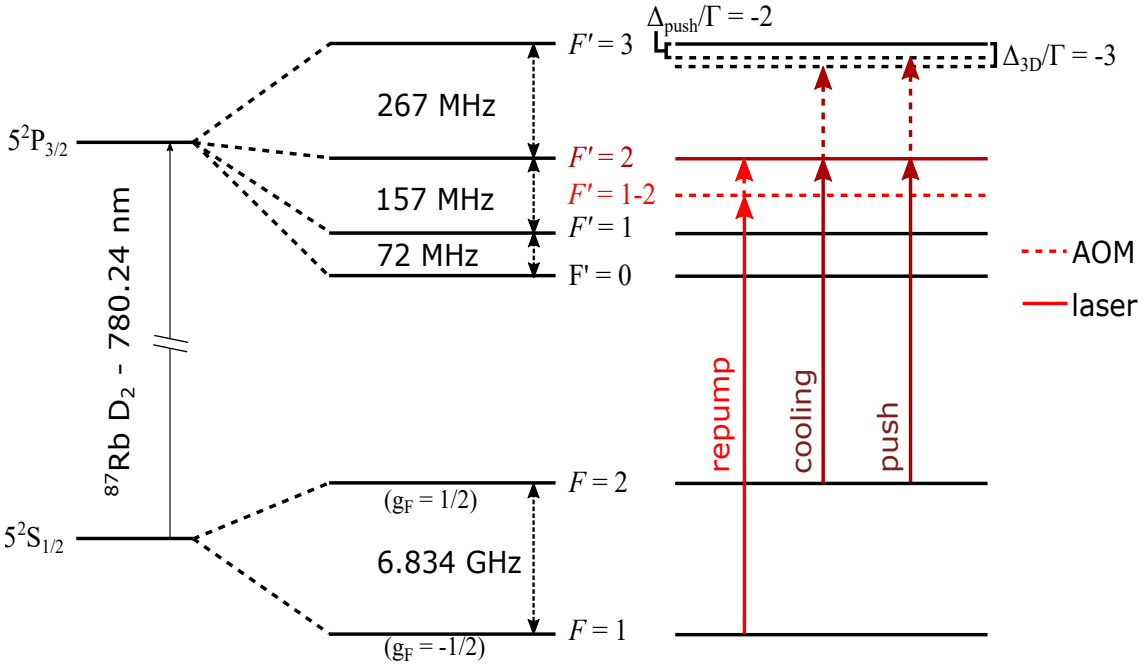

Figure 3.2: Hyperfine splittings for the D_2 transition in ^{87}Rb from Steck [65]. The vertical light and dark red lines on the right show the repump and cooling transitions in our experiment respectively. Solid lines indicate laser transitions and dashed lines indicate a frequency shift induced by an acousto-optical modulator (AOM). The highlighted red horizontal lines indicate the frequencies we stabilize the lasers to. Δ_{3D} and Δ_{push} indicate the detunings of the 3D cooling beams and the push beam from the $|F = 2\rangle \rightarrow |F' = 3\rangle$ transition.

The laser diodes used in the ECDLs are Q-Photonics QLD-780-80S single-mode laser diodes. The diodes are wavelength selected to have a free running wavelength close to 780 ± 2 nm with an output power of $\sim$80 mW. We mount the diodes in a Newport U100-A kinematic mount that rests on an aluminum block that is cooled by a thermo-electric cooler. The mount is temperature stabilized to prevent thermal drifts. In addition, we use the temperature stabilization to set the free running wavelength of the diodes as close to 780 nm as possible. We find that setting the free running wavelength close to 780 nm improves the mode-hop-free tuning range once the external cavity is in place.

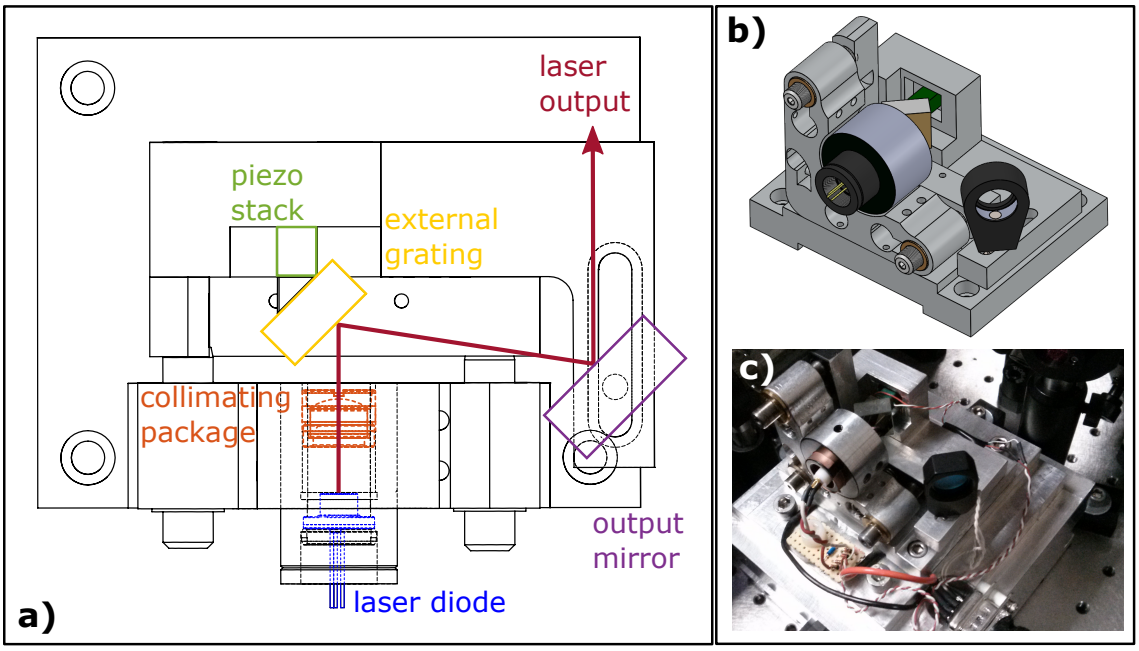

Figure 3.3: Diagram of the external cavity diode lasers (ECDLs) we use to generate the cooling and imaging light for the experiment. a) Top-down diagram of our ECDLs showing the operating components in a Litrow configuration ECDL. b) A 3D rendering of the ECDL, and c) a photograph of the repump master laser in our setup.

The external cavity is composed of the rear diode facet on one end and a Thor-Labs GH13-18U UV Holographic grating with 1800 lines/mm on the other. The holographic grating reflects $\sim 28\%$ (see Thorlabs grating specs) of the total output power back into the diode cavity, providing optical feedback. Moving the grating allows us to tune the output frequency of the laser. The grating is mounted to the diode housing on a piezoelectric stack and we use the grating position to provide electronic feedback and stabilize the laser frequency to a Rb reference cell. Figure 3.4 shows an optical layout for the repump master-slave lasers and the cooling master-slave lasers.

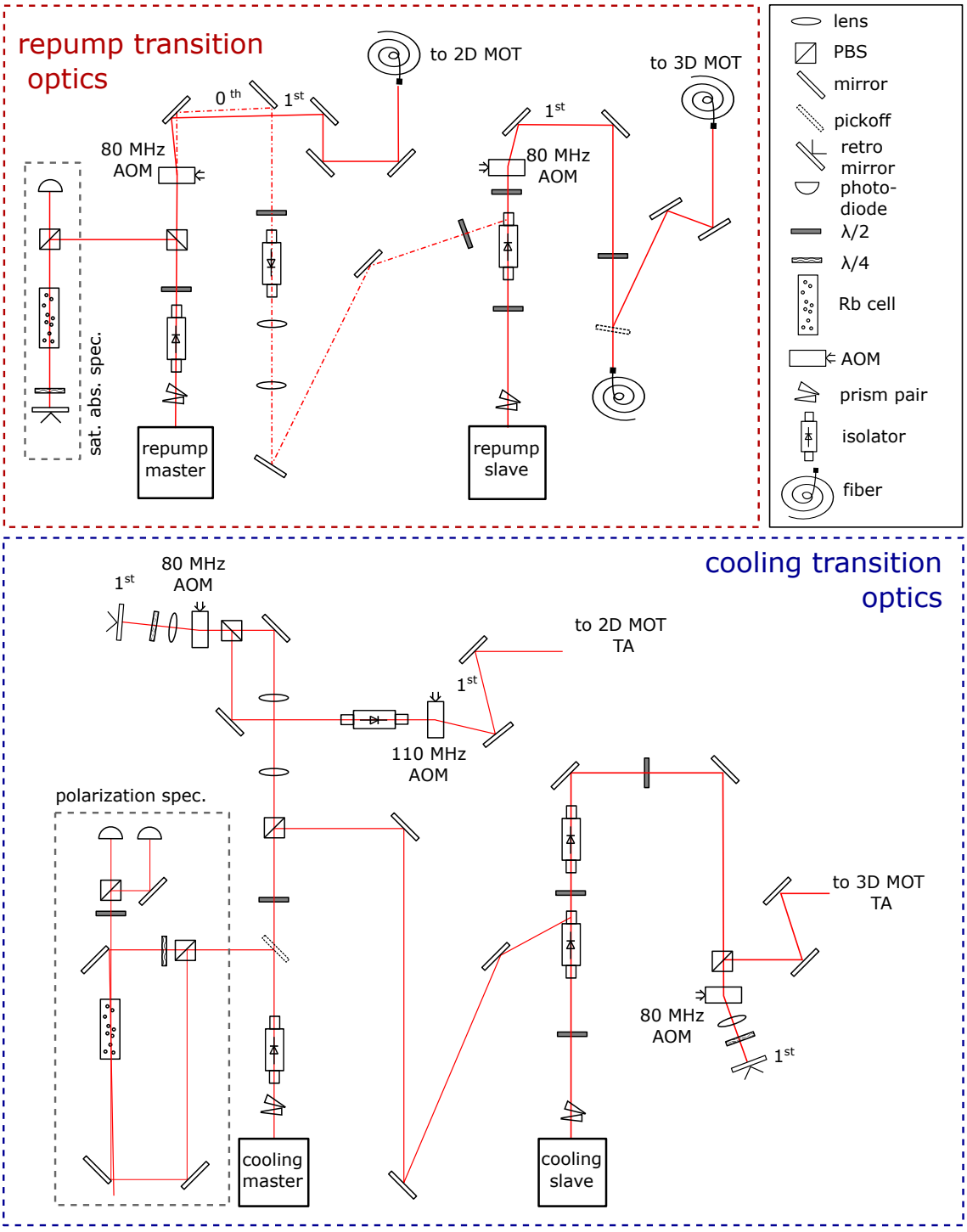

Figure 3.4: Layout of the optical systems for the experiment. The repump master laser is stabilized to a ^{87}Rb cell using standard saturated absorption spectroscopy and an electronic feedback loop that controls the cavity length of the lasers. The cooling master laser is stabilized using polarization spectroscopy. These two lasers provide the light for the 2D MOT. Slave lasers that are injection locked to the master lasers provide the light for the 3D MOT.

3.1.2 Laser locks

We pick off a small amount of light (a few mW) from the output of the two master lasers for use in the Doppler-free spectroscopy setups shown in Fig. 3.4.

Repump lasers:

Figure 3.5 shows an oscilloscope trace of the repump error signal we use to lock the laser. We generate an error signal from the saturated absorption signal by modulating the laser drive current directly, which in turn modulates the frequency of the laser. A lock-in amplifier is used to electronically differentiate the saturated absorption signal.[1] Directly modulating the laser drive current does not negatively affect our ability to make a MOT or image atoms with the repump light.

As Fig. 3.5 indicates, we lock the repump master laser to the $|F' = 1 - 2\rangle$ crossover dip. The majority of the light from the repump master laser passes through an 80 MHz AOM operating at 78.2 MHz so that the 1^{st} order light is on resonance with the $|F = 1\rangle \rightarrow |F' = 2\rangle$ transition. The repump master light is then coupled into one of the inputs of the 2x4 fiber splitter (see section 3.1.3). The unshifted (0th order) light is used to injection lock the repump slave laser.[2] Since we don't adjust the power or frequency of the 2D MOT beams, we leave the repump master AOM on at constant frequency at all times when the experiment is running. This insures that the injected light to the slave laser remains at a constant, low power so as not to damage the diode.

Similarly, the output of the repump slave laser passes through an 80 MHz AOM

[1] We drive the repump master laser using a MOGlabs laser diode controller. In addition to the laser drive current, the MOGlabs controller includes an on-board temperature controller, a 250 kHz AC modulation to the drive current, a lock-in amplifier and an internal servo loop. Locking the repump master laser is done entirely through the MOGlabs controller.

[2] For more information on injection locking see lab notebook #2 pg. 6-7.

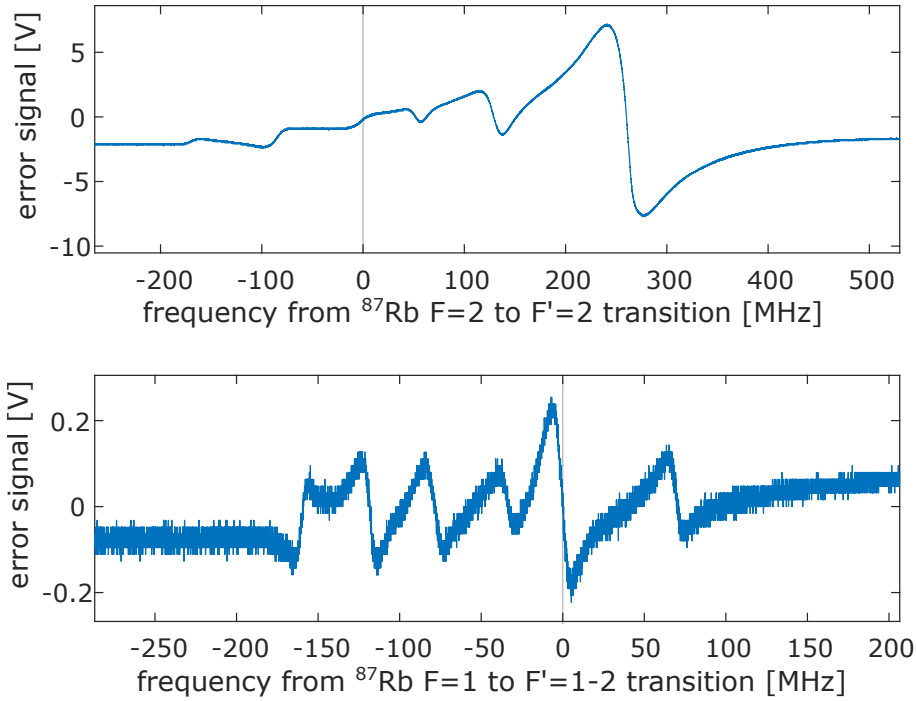

Figure 3.5: Representative scans of the error signal for the cooling (top) and repump (bottom) transitions in ^{87}Rb. The dispersive lineshape for the cooling lock comes directly from the optical setup using polarization spectroscopy while the error signal for the repump lock is generated electronically from a set of Doppler-free absorption dips. Light gray lines indicate the position in each scan where we lock the lasers.

before it is sent to the 3D MOT via optical fiber. In addition to the frequency shift, we use the AOM to switch the repump light on and off quickly ($\sim$20 μsec) during the optical pumping and imaging stages of the experiment.

Cooling lasers:

We lock the cooling laser to the $|F = 2\rangle \rightarrow |F' = 2\rangle$ transition, -266.7 MHz from the $|F = 2\rangle \rightarrow |F' = 3\rangle$ transition, using a polarization spectroscopy based lock. Polarization spectroscopy refers to a Doppler-free spectroscopy technique that takes advantage of optically induced birefringence of an atomic sample using a circularly polarized pump beam. The details of this technique can be found in Refs. [67, 68,

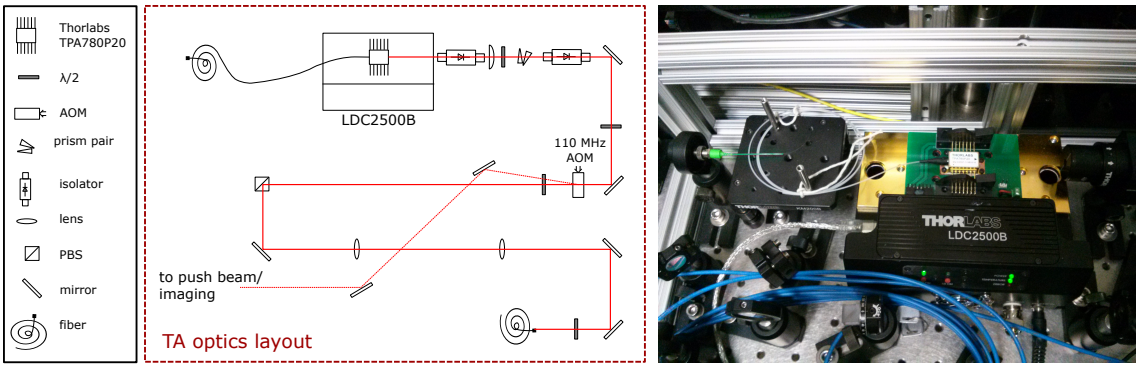

Figure 3.6: Optical layout (right) of the 3D MOT tapered amplifier along with an image (left) of the Thorlabs amplifier and driver. The optical layout for the 2D amplifier is similar, with the exception of the 110 MHz AOM which comes before the amplfier for the 2D MOT.

69, 70]. The advantage of this technique is that it generates an error signal with a zero-crossing at the position of the Doppler-free transitions in an atomic gas without modulating the laser frequency. Figure 3.5 shows the spectrum we use to lock the cooling master laser to the ^{87}Rb cooling transition.

We injection lock the slave laser using a small amount of light picked off from the master laser. The light from both the master and slave lasers is then shifted towards resonance by an 80 MHz, double-pass AOM set at 73.3 MHz and a single pass, 110 MHz AOM set at 102 MHz. The combination of these two AOM shifts gives a total shift of (102+2×73.3) MHz = 248.6 MHz, so that the cooling light for both MOTs is detuned from resonance by $\Delta \sim -3\Gamma$, where Δ is the detuning of the lasers from the atomic resonance, and $\Gamma = 2\pi\times$ 6 MHz is the natural linewidth of the cooling transition.

The output of each of the cooling lasers is sent to a Thorlabs TPA-780P20, 2-W, 780-nm tapered amplifier. The TPA-780P20 is an optical amplifier which has been integrated into a standard 14-pin butterfly package as shown in Fig. 3.6. The input to the tapered amplifiers is a single-mode optical fiber, which makes aligning the

amplifier relatively simple. About 5-10 mW of power is sufficient to seed the tapered amplifiers; at powers higher than 15-20 mW the amplifier gain saturates. The amplifiers are driven by a Thorlabs LDC2500B current and temperature controller that can provide up to 2.5 A of drive current. At this current, the amplifier output is ∼2 W of power at 780 nm with 10 mW of seed light. Under typical operating conditions we run the 2D and 3D MOT amplifiers at ∼1.6 A drive current. At this current, the output of the amplifiers is ∼ 0.8 W each. The output of each amplifier goes through a series of conditioning optics and is then coupled into fiber splitters that provide light for the MOTs. The fiber splitters are discussed in more detail in section 3.1.3.

In addition to stimulated emission from the seed light, the amplifiers also emit a few hundred mW of spontaneous emission. We assume that light coupled into the MOT fibers is predominantly stimulated emission at the seed frequency since the angular divergence of the spontaneously emitted light is much wider than that of the stimulated emission. However, since the seed light is fiber coupled directly to the amplifier chip, a significant fraction of spontaneous emission emerges from the tapered amplifier input fibers in the direction of the seed lasers. In order to avoid optical feedback from the amplifiers, we use two free space isolators on the outputs of all ECDLs.

Figure 3.6 a) shows a layout of the optics used for fiber coupling the output of the 3D MOT laser amplifier (the 2D MOT coupling optics are almost identical). The only major difference between the layouts for the two amplifiers is that the final 102 MHz AOM shift for the 2D MOT light occurs before the amplifier while the AOM shift for the 3D MOT light occurs after the amplifier. The unshifted light from the amplifier is used for the $|F = 2\rangle \rightarrow |F' = 3\rangle$ imaging light and for the 2D

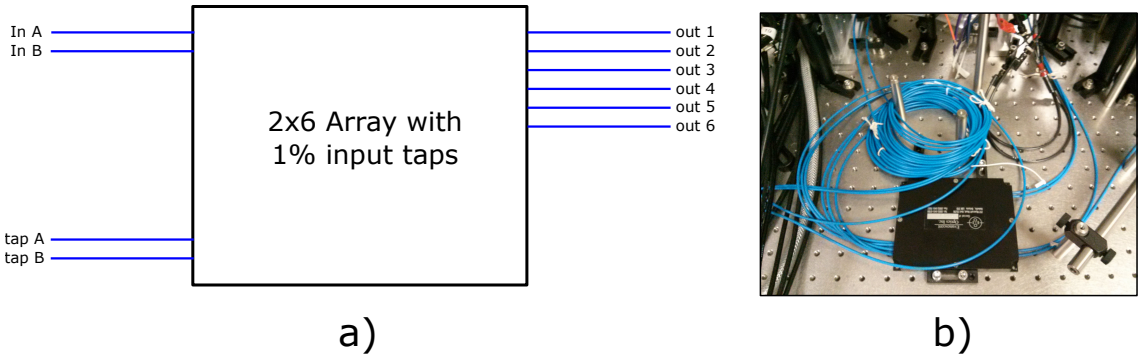

Figure 3.7: a) Diagram and b) image of the 2x6 fiber splitter used to deliver the 3D MOT light to the vacuum chamber.

MOT push beam (discussed in section 3.2). We place the AOM after the amplifier so that we can use the AOM as a fast on-off switch, which is important for imaging the BEC.

3.1.3 Fiber splitters

In place of free space optics we use 2x4 and 2x6 fiber splitters made by Evanescent Optics to deliver light from the amplifiers to the 2D and 3D MOTs respectively. We couple the cooling and rempump light for a single MOT into the same splitter. Fig. 3.7 shows a diagram and an image of the fiber splitter for the 3D MOT. The fiber splitters divide the input light into four (or six) fibers with each close to 25% of the total input power for the 2D MOT (and 16% for the 3D MOT). Due to the elliptical shape of the output beam from the tapered amplifiers and the need for beam conditioning optics and free-space isolators, typical coupling efficiencies are around $55 - 60\%$.

Both fiber splitters include a 1% tap for each input, which we use to monitor the frequency of the light with a Thorlabs SA200 scanning Fabry-Perot cavity. Figure 3.8 shows a trace of the Fabry-Perot output with light from all four MOT

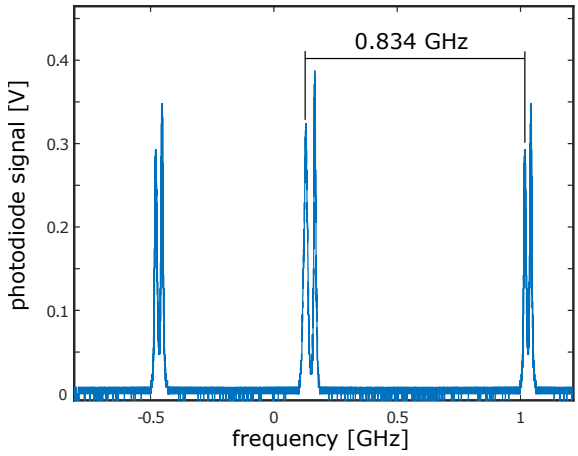

Figure 3.8: Scanning Fabry-Perot (FP) cavity trace of the repump and cooling lines. The free spectral range of the FP cavity is 1.5 GHz. The ground-state splitting in ^{87}Rb is 6.834 GHz, so the repump and cooling lines are separated by 6.834 GHz modulo 1.5 = 0.834 GHz. The resolution of the FP is 7.5 MHz, so although the linewidth our ECDL is a few hundred kHz, each of the lasers shows up as a ∼8 MHz single-mode peak. The master and slave lasers show up as separate peaks due to slight differences in alignment into the FP cavity.

lasers present. The resolution of the SA200 Fabry-Perot cavity is 7.5 MHz, much larger than the linewidth of our locked diode lasers; even so the Fabry-Perot has proven very useful for determining whether or not the lasers are operating in a single longitudinal mode.

The use of fiber splitters to deliver light for the MOT beams offers several advantages over free space optics. First, we do not need ∼100 extra polarization optics, lenses and mirrors for dividing beam power and conditioning the 2D and 3D MOT beams. Second, the amount of space required for two sets of MOT optics is minimized. Third, the cost of free space optics for two MOTs is comparable to the cost of the fiber splitters, while long term beam alignment is improved with fibers. Finally, fiber coupled MOT light also offers added flexibility for potassium or dual species experiments in the future. In that case, the MOT optics near the cell remain the same and we only need to change how light couples into the fibers.

3.2 The 2D MOT - Cold beam source

The capture velocity, v_{cap}, of a MOT refers to the maximum velocity of an atom that can be captured by the MOT. The capture velocity depends only on the volume of the MOT beams and the atomic species being cooled, provided the MOT beam intensity, I, is much greater than the saturation intensity, I_{sat}.

In this case, for a MOT beam with radius $\mathrm{r_{MOT}}$, the maximum acceleration of an atom in the MOT is:

$$a_{max} = \hbar k \Gamma / 2m \tag{3.1}$$

where $k = 2\pi/\lambda$ is the wavenumber for the cooling light and m is the mass of a rubidium atom. For ^{87}Rb, this corresponds to an acceleration of $11 \times 10^4 \mathrm{m/s}^2$.

Assuming the maximum acceleration, the capture velocity for an atom to be cooled to the lower limits of the MOT by the time it reaches the center of the MOT is,

$$v_{cap} = \sqrt{a_{max} r_{\mathrm{MOT}}}. \tag{3.2}$$

In BEC 1, the 3D MOT beams have a radius of $r_{\mathrm{MOT}} = 23mm$ which corresponds to a capture velocity of $v_{cap} \sim 75\mathrm{m/s}$, significantly lower than the root-mean-square room temperature velocity of a ^{87}Rb atom, $v_{rms} \sim 300\mathrm{m/s}$.

It is possible to cool and trap atoms in a MOT from a thermal distribution of atoms, but only atoms in the low velocity tail can be captured. In order to load a large number of atoms into the MOT in a reasonable amount of time, the partial pressure of atoms inside the vacuum chamber must be relatively high so that there are a sufficient number of atoms in the chamber with $v < v_{cap}$. This is the method for loading a MOT in BEC 1.

A MOT can be loaded more efficiently from a pre-cooled source of atoms such as

a cold atomic beam. A number of techniques are available for producing a cold beam of atoms for loading a MOT. Some of these techniques include: Zeeman slowers [71], Low Velocity Intense Source [68], atoms funnels [72, 73] and 2D MOTs.

For BEC 2 we have chosen to load our 3D MOT from a cold beam source provided by a 2D MOT. A 2D MOT is an elogated 3D MOT where the cooling beams and the magnetic field gradient in the longitudinal direction have been removed. With these viscous and restoring forces removed, atoms are free to exit the MOT region along the longitudinal axis. In other words, the 2D MOT is not a true "trap", but radiative cooling in the transverse directions means that atoms that spend time interacting with the MOT beams have a lower $v_{rms} = \sqrt{v_x^2 + v_y^2 + v_z^2}$. Figure 3.9 gives a diagram of a typical 2D MOT.

Atoms are extracted through an aperture in the chamber. The aperture serves two purposes: first, it separates the relatively high pressure 2D MOT side of the chamber from the low pressure science chamber. Second, it acts as a velocity filter for atoms exiting the 2D MOT. The reason for the second point is less obvious and deserves a brief discussion.

Consider an atom moving through the high pressure side of the chamber that encounters the 2D MOT. The more time it spends interacting with the 2D MOT beams, the lower its transverse velocity. An atom moving with higher longitudinal velocity spends less time interacting with the 2D MOT beams and on average has a higher velocity in the transverse direction. The solid angle of the aperture relative to the end of the 2D MOT region defines a cutoff transverse velocity above which atoms will not exit the high pressure chamber.

Several configurations of 2D MOTs exist. The main difference between the various configurations is the presence/absence of cooling beams along the

longitudinal axis. In BEC 2, we choose to add a cooling beam co-propagating with the atoms to collect some of the atoms that would otherwise exit the 2D MOT region and hit the 2D MOT chamber walls; we call this beam the "push" beam.

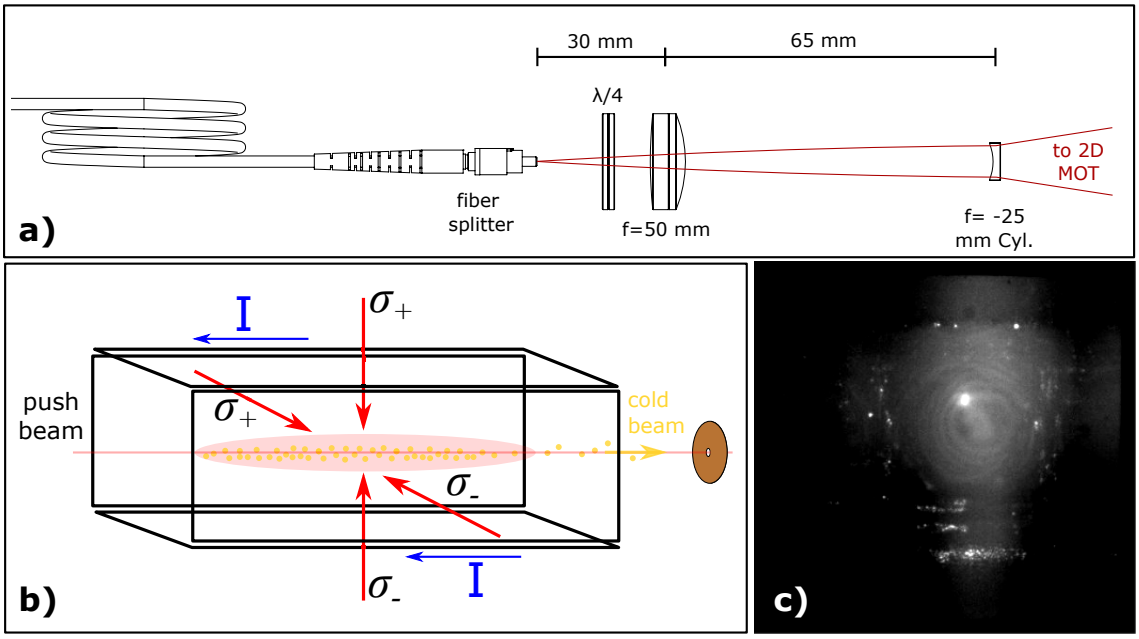

Figure 3.9: a) Optics for shaping 2D MOT beams. With this optical system the 2D MOT beams come directly out of our 2x4 fiber splitter and end up as 1x4 inch, circularly polarized beams at the center of the 2D MOT chamber. b) Diagram of a typical 2D MOT setup with a push beam propagating along the atom beam axis. The 2D MOT beams are shown as red arrows and the elongated quadrupole coils are depicted as black rectangles. The atoms (yellow circles) are shown occupying the region of overlap of the 4 MOT beams (light red oval) and propagating towards the aperture located at the end of the 2D MOT cell. c) An image of the 2D MOT fluorescence looking down the axis of the chamber. The 2D MOT is bright dot in the center of the image. Fluorescence from the MOT beams surrounds the 2D MOT. On close inspection, the glass walls of the 2D MOT chamber can be seen at the edges of the image as a dark black border. The chamber walls are 1" inch across for scale.

Figure 3.9 shows a diagram of a standard 2D MOT with an image of the 2D MOT in BEC 2. Our 2D MOT consists of two pairs of counter-propagating cooling

beams, with an aspect ratio of about 4:1, that overlap with a linear magnetic field in two dimensions. Along the third dimension there is no B-field gradient. This results in a pencil-shaped, optically thin ensemble of laser cooled atoms which forms the 2D MOT. We choose the long axis of the pencil to be parallel with the chamber axis. The 2D MOT creates a cold beam of atoms that propagates down the differential pump tube towards the 3D MOT cell. We then capture the atoms from the cold beam with the 3D MOT.

The cooling and repump light for our 2D MOT comes from one of two tapered amplifiers via a 2x4 fiber splitter as discussed in section 3.1.3. Each MOT beam exits the 2x4 fiber splitter, expands out of the bare fiber and then passes through an $f = 50$-mm, convex lens located 30 mm from the fiber such that the beam is weakly diverging and then passes through a $f = -25$-mm, concave, cylindrical lens located roughly 150 mm from the center of the cell so that the beam diverges strongly in the direction parallel to the vacuum chamber axis. At the center of the 2D MOT chamber the cross section of the four MOT beams are approximately 4 inches wide by 1 inch tall. Figure 3.9 a) shows a drawing of the 2D MOT optics layout for one of the MOT beam paths. We typically run the 2D MOT amplifier drive current at ∼1.6 A. At this drive current, the output power of the amplifier is close to 400 mW at the input of the fiber splitter, which corresponds to 55-60 mW/beam at the position of the 2D MOT. For reference, this ends up being ∼0.5 I_{sat} for the $|F = 2\rangle \rightarrow |F' = 3\rangle$ transition in ^{87}Rb.

In addition to the 2D MOT beams, we also add a push beam that overlaps the 2D MOT. The purpose of the push beam is to redirect atoms moving in the direction opposite the science chamber back towards the 3D MOT cell. The light for the push beam (and the $|F = 2\rangle \rightarrow |F = 3'\rangle$ imaging light) comes from the un-shifted light

from the 3D tapered amplifier. This light is coupled into a fiber (see Fig. 3.6) and then goes through a double-pass, 60 MHz AOM where it is shifted in frequency to the desired detuning. We typically use push beam powers on the order of a few hundred μW.

Initially we chose to use a set of permanent magnets glued to a set of long Thorlabs cage rods that formed a box around the cell to provide the magnetic field gradient for the 2D MOT. Permanent magnets would require fewer power supplies to operate the experiment. However, we found that permanent magnets made aligning the 2D MOT to the chamber axis cumbersome. Ultimately we chose to use electromagnets instead of permanent magnets as they offered a much improved flexibility over the field gradient and the position of the B=0 line.

Figure 3.9 b) shows a diagram and corresponding image of the magnetic field coil arrangement around the 2D MOT chamber. We use a pair of quadrupole coils that provide a gradient of 20 G/cm in the x and y directions and a pair of bias coils that are used to align the 2D MOT axis to the chamber axis.

Figure 3.9 c) shows an image of our 2D MOT looking down the axis of the chamber. Since the 2D MOT has a relatively small number of atoms, we find it easiest to see the 2D MOT by looking down the axis of the chamber so that we see an integrated florescence signal along the long axis of the MOT. We have also been able to see the 2D MOT along the transverse axis by spatially moving the B=0 line via the current in the bias coils, so that we can pick out the atoms in the MOT moving by eye.

We align the 2D MOT to the chamber axis by imaging both ends of the 2D MOT on a camera. If we have done a good job with the alignment, the position of the florescence signal from the atoms should remain constant when focusing on the

ends of the 2D MOT. If not, the position of the atoms will appear to move. We can adjust the alignment by manually adjusting the tilt of the B-field coils. Once the 2D MOT is aligned to the chamber axis, we overlap the position of the MOT with the small pinhole at the end of the 2D MOT cell using the bias coils. The push beam is aligned to the 2D MOT axis by first aligning the push beam to the chamber and then overlapping the position of the MOT flourescence with the position of the push beam (at very low power) on the same camera.

3.3 3D MOT using diverging beams

We collect atoms in our 3D MOT directly from the atom beam created by the 2D MOT. Our 3D MOT consists of 3 pairs of counter-propagating, circularly polarized, diverging beams that intersect at the center of the octagonal 3D MOT cell. We use the center coil in our transfer coil system, which is described in detail in section 4.2, as our 3D MOT coil. Figure 3.10 c) shows an image of the 3D MOT florescence looking down the axis of the chamber.

As with the 2D MOT, the cooling and repump light for the 3D MOT are coupled into a fiber splitter so that the cooling and repump light are overlapped. The MOT light is delivered to the vacuum chamber by a set of six compact beam expanders that are made using Thorlabs cage optics. A diagram of the beam expanders is shown in Fig. 3.10 a) along with an image of one of the assembled beam expanders in place around the vacuum chamber in Fig. 3.10 b). Each of the six ends of the fiber splitter is attached directly to a beam expander via fiber adapters.

Briefly, light exiting one of the MOT beam fibers hits a half-inch mirror at 45° with respect to the table and is directed upwards towards the vacuum chamber. MOT light then passes through a quarter-wave plate (QWP) and a 75-mm focal

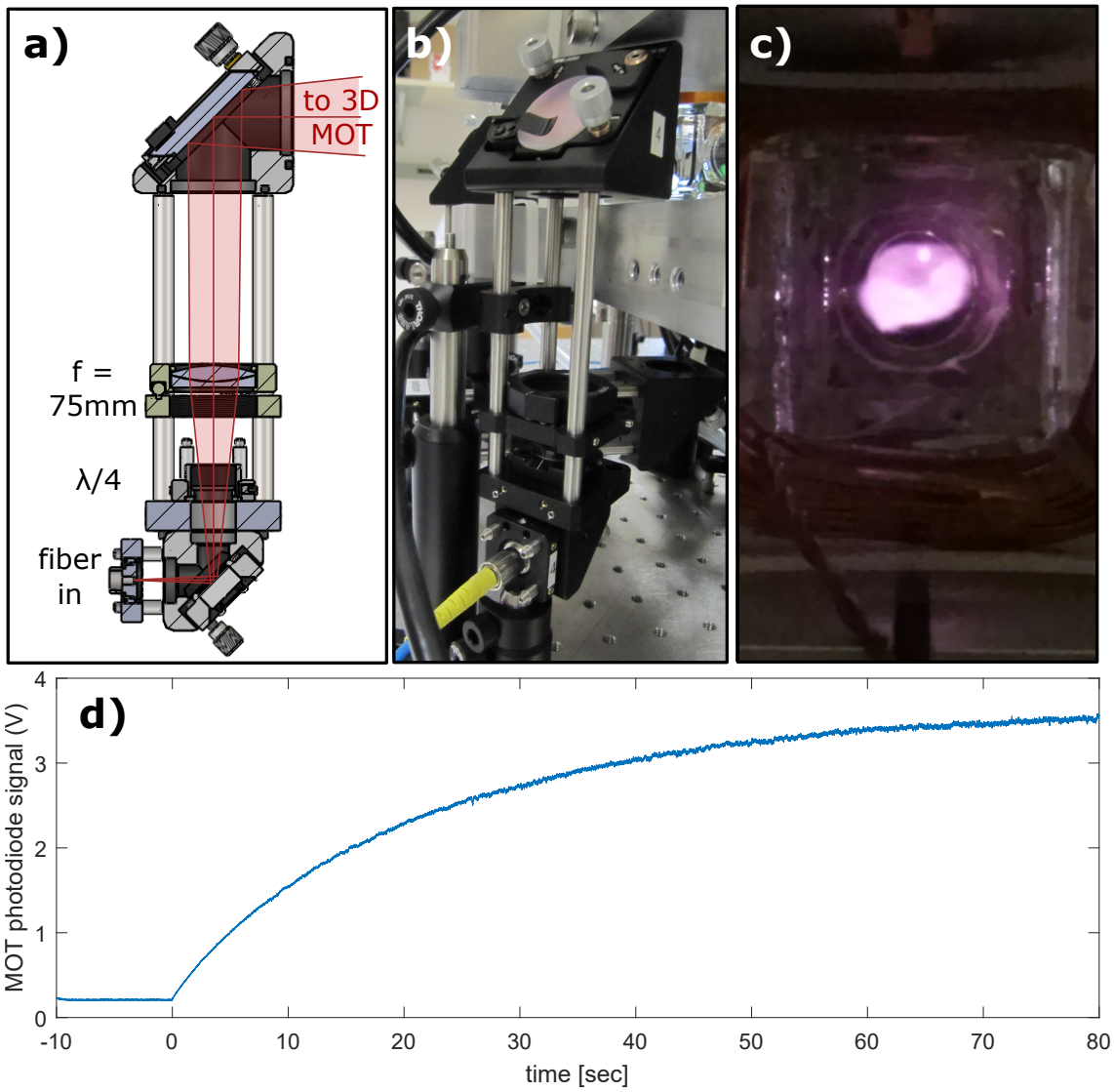

Figure 3.10: a) Optical diagram and b) image of one of the 3D MOT beam expanders. c) Image of the 3D MOT fluorescence in the center of the octagonal cell. The small bright dot in the top right corner of the MOT is the push beam. The presence of the push beam shifts the center-of-mass of the MOT slightly downward. d) A MOT loading curve taken on the same day image as the image in c). A 4V fluorescence signal corresponds to about 5-10x10^9 atoms. We typically load the 3D MOT to about 3-3.5V.

length, convex lens that is mounted on a magnetic, removable mount. The lens is positioned such that the MOT beams are weakly diverging. Finally the MOT light hits a 1" mirror that directs the light parallel to the table and towards one of the 1.25" wide windows that make up the walls of the octagonal cell.

At the walls of the cell, the MOT beams are circular, with a diameter slightly under 1.25". We estimate at the center of the chamber, at the position of the MOT, the beams are close to 1.5" in diameter. One of the advantages of our diverging beam MOTs is that we are able to use small, compact optics and still have the large capture velocities associated with large-diameter MOT beams.

3.3.1 MOT alignment

During the alignment process, we replace the 75-mm lens with a shorter focal length lens and position the lens such that the MOT beams are collimated. We then use irises to stop the beam down to $\sim$1 mm in diameter and coarsely align counter-propagating pairs of MOT beams by adjusting the position and pointing of the beam expanders. We do a finer alignment using the kinematic mounts on each expander. The 75-mm lens is then moved back to the original position, allowing the beams to diverge.

The polarization of each of the six MOT beams is set by aligning the fiber adapter plate so that the fiber notch points down towards the table. Then we set the angle of each of the QWPs by sending the MOT light through a reference polarizing beam-splitter (PBS) cube, the QWP and then retro-reflecting the beam back toward the fiber. If the waveplate is aligned to produce circularly polarized light, the input beam will exit the opposite port of the PBS cube. This procedure is repeated for all six waveplates, and we mark the angles on each waveplate that correspond to

circularly polarized light. The final alignment of each waveplate is done by tweaking the angle of the waveplate to optimize the atom number in the MOT or the shape of the MOT.

3.3.2 MOT Number and Optimization

We calculate the number of atoms, N, in the MOT by measuring the MOT fluorescence on a photodetector. We collect MOT light with a 25-mm focal length lens placed 75 mm from the MOT. The total power, P_{MOT}, emitted by the MOT is given by:

$$P_{\mathrm{MOT}} = E_{photon} \times \textit{photon scattering rate/atom} \times N \tag{3.3}$$

$$= \frac{hc}{\lambda}\Gamma_{sc}(\Delta)N \tag{3.4}$$

$$= \frac{Nhc}{\lambda}\frac{\Gamma}{2}\frac{I/I_{sat}}{1 + I/I_{sat} + 4(\Delta/\Gamma)^2} \tag{3.5}$$

where $I_{sat} = 1.66$ mW/cm^2 is the saturation intensity for the $|F = 2\rangle \rightarrow |F' = 3\rangle$ transition in ^{87}Rb.

We calibrate the photodiode voltage using a 780-nm beam of known power and then calculate the number of atoms based on the voltage measured on the photodiode. For our MOT beam detuning, push beam power and Rb partial pressure, we can typically load $3 - 5 \times 10^9$ atoms in our 3D MOT. On occasion we have been able to load upwards of 1×10^{10} atoms in the 3D MOT.

The largest atom numbers in the 3D MOT do not necessarily indicate the best conditions for making a BEC. We optimize the MOTs by first optimizing the atom number in the 3D MOT as a function of the 2D MOT parameters and then optimizing the number of atoms in the final magnetic trap by adjusting parameters of

the 3D MOT.

Although atom number in the 3D MOT is important, we are primarily concerned with achieving the highest phase space density possible at any point in the BEC production sequence. We have found that the most useful measurements of phase space density are made in the final quadrupole trap after a period of RF evaporation or after transferring atoms into a harmonic trap and allowing the atoms to equilibrate for a few seconds.

The optimization of phase-space density involves both magnetic trap loading and a "compressed MOT" (CMOT) [48] stage, parts of the BEC sequence that occur after loading atoms into the 3D MOT which are discussed later; in the following sections I only discuss methods for optimizing MOT parameters. We have noticed however, that the conditions that optimize phase space density in the quadrupole trap tend to be very similar to the conditions that optimize atom number in the MOT, so practically, optimizing the atom number in the MOT is a reasonable first step in this process.

3.3.3 2D MOT optimization

We optimize alignment and other 2D MOT parameters by maximizing the atom number in the 3D MOT. In adition to the MOT beam alignment we adjust the following parameters of the 2D MOT: bias coil current, MOT beam power and detuning, and push beam alignment, power and detuning.

The following is a step-by-step procedure for optimizing the 2D MOT once the 2D and 3D MOT beams have been aligned and a MOT florescence signal is present on the photodiode:

1. Adjust the current in the bias coils to center the 2D MOT on the vacuum

chamber. There should be a range of 0.5 A per coil pair where the photodiode signal is roughly constant. At some point, 3D MOT number will drop off significantly. This corresponds to a position where the cold beam from the 2D MOT hits the pinhole at the end of the 2D MOT cell. Typically we try to center the 2D MOT on the pinhole.

2. Adjust 2D MOT cooling beam detuning on the 2D MOT double-pass AOM. Since the 2D and 3D MOT beam detunings are independent, a change in the photodiode signal is only due to a change in atom number in the 3D MOT. We find that a 2D MOT cooling beam detuning of $\Delta_{2D} = -2\Gamma$ produces the highest atom numbers in the 3D MOT.

3. Coarsely align the push beam to the center of the chamber using the irises in the push beam path and the center of the 3D MOT cell as a guide. Final alignment of the push beam is done by walking the push beam to a position that optimizes atom number for a given power and detuning.

4. Push beam power and detuning: We determine the optimal push beam power and detuning by iteratively stepping through a parameter space of power and detuning. For a given detuning, we step through a range of push beam powers. Then we change detuning and repeat the process. We choose the conditions that optimize the MOT number. At the time of writing, we are using $\Delta_{push} = -3\Gamma$ and $P_{push} \sim 300\mu$W.

3.3.4 3D MOT alignment

Once the 2D MOT parameters have been set we align the 3D MOT beams to the center of the magnetic field. We typically choose to look at the position of the

MOT relative to the magnetic field zero for the 3D MOT alignment for two reasons: 1) As mentioned above, the total atom number does not necessarily correspond to the conditions for highest phase-space density, and 2) many of the 3D MOT parameters affect the scattering rate and as a result, the MOT photodiode signal is not independent of the 3D MOT parameters. Our procedure for optimizing the 3D MOT parameters once the MOT beams are initially aligned is given below:

1. A rough alignment of the position of the magnetic field zero with the center of the MOT should be performed by shutting off the push beam and coincidentally ramping up the magnetic field gradient in the MOT and watching the motion of the atoms on a camera. If the MOT position coincides with the magnetic field minimum, the MOT will change size (radially shrinks) with no motion of the center of mass of the cloud. If not, there will be a net motion of the center-of-mass of the cloud in the direction of the magnetic field zero. The MOT beam alignment can be tweaked to minimize the center of mass motion.

2. MOT beam intensity balance can be adjusted by turning off the B-field and watching the MOT expand. If there is an imbalance in the cooling intensity in a particular direction the atoms will feel a force away from the higher intensity beam. MOT beam power can then be adjusted until there is no net motion of the center of mass of the cloud when the magnetic field is turned off. This procedure should also be done in the absence of the push beam.

3.3.5 CMOT

Before transferring atoms to a purely magnetic trap we cool and compress atoms in a CMOT. During the CMOT we decrease the MOT cooling beam power and detuning and the repump power. Reducing the cooling beam power and detuning

along with repump power results in a lower scattering rate from $|F = 2\rangle \rightarrow |F' = 3\rangle$ which benefits us in two ways. 1) More energetic atoms in the MOT escape, and the result is a lower temperature MOT. 2) The reduction in scattered light results in an increase in density as the internal radiation pressure pushing MOT atoms outward is reduced. The overall effect of the CMOT is a colder denser cloud. In addition to gains in phase-space density, the denser cloud is better mode-matched to the cloud size in a purely magnetic trap with a strong field gradient. In BEC 2, the CMOT plays a major role in increasing phase-space density and loading atoms into the magnetic trap prior to transfer. Figure 3.11 shows the timing sequence for loading atoms from the MOT into the purely magnetic trap.

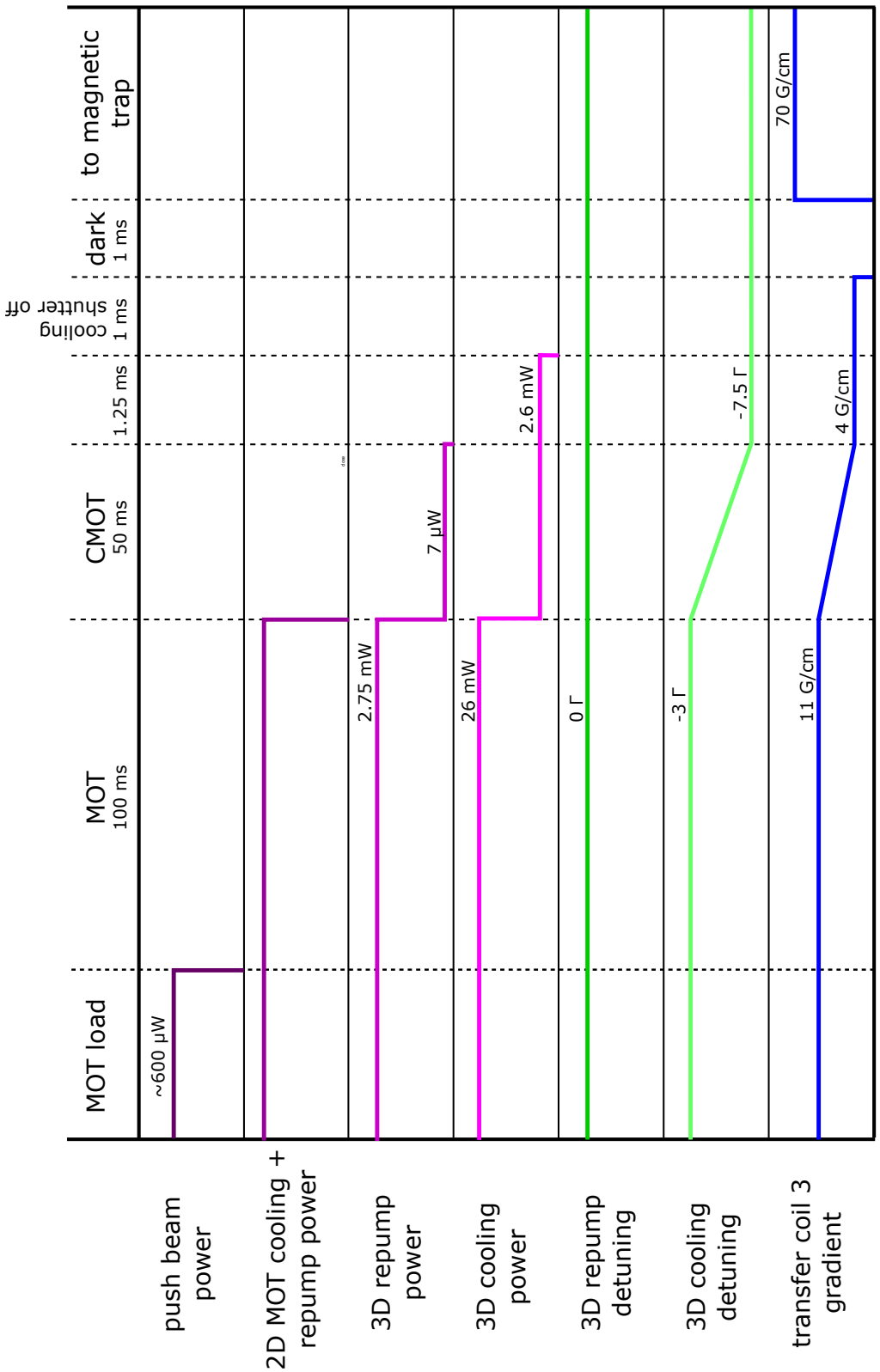

Figure 3.11: Overview of the MOT load and magnetic caputure sequence.

As indicated in the figure, our CMOT stage lasts for 50 ms. During this period we decrease the cooling intensity from 26 mW/beam to 18 mW/beam and the cooling beam detuning from -3Γ to -6Γ. In adition, the repump power is decreased from 2.75 mW/beam to 100 μW/beam. We find that the temperature in the final magnetic trap is most sensitive to the repump power in the CMOT stage.

As shown in Fig. 3.11, in addition to the changes in the cooling and repump beams, we also decrease the B-field gradient from 11 G/cm to 6 G/cm. In the original investigation the B-field gradient was increased during CMOT as it further increases the cloud density. However, we find that loading into our 70 G/cm initial magnetic trap is more efficient if we decrease the B-field gradient during CMOT. The same is true for BEC 1.

It is worth noting that some other groups add an optical molasses stage following the CMOT as a final optical cooling stage before loading into a magnetic trap (ref). We do not use a molasses stage in BEC 1 or 2. In both machines, we have found that the lower temperatures achieved do not compensate for the decreased density in the initial magnetic trap.

3.3.6 Loading into a purely magnetic trap

Following the CMOT state, but prior to loading into a purely magnetic trap we shut off the repump light and leave the cooling light on for 1 ms as a means of optically pumping atoms into the CMOT into the $|F = 1, m_F = -1\rangle$ state, which is magnetically trappable. After the 1ms "dark" period with no fields we snap the magnetic field on to a gradient of 70 G/cm, catching the atoms in a purely magnetic trap. This is the initial step in our magnetic transfer process towards one of the two

science chambers. [3]

3.3.7 Factors of the MOT that affect transfer/BEC

Another significant benefit of a diverging beam MOT is that we are not as sensitive to misalignment of the MOT beams or standing waves due to beam interference as one might expect with a collimated beam MOT. However, that is not to say that we have not noticed effects due to MOT alignment/parameters on the atom number in the final magnetic trap. We have on occasion noticed that optimizing the 3D MOT for atom number has resulted in shot-to-shot inconsistency in the number of atoms in the final quadrupole trap (or in some cases almost no atoms at all). In this case, since the MOT optics themselves are very stable, small tweaks on one of the MOT beam mirrors or QWP plates are all that is needed to return to good loading parameters.

[3] We choose a "catch" value of 70 G/cm so that the size of the initial magnetic trap matches the size of the cloud for a given temperature. Once atoms are trapped, we can adiabatically adjust the B-field gradient to provide stronger confinement.

CHAPTER 4

Magnetic Fields

Trapping potentials provided by inhomogeneous magnetic fields are a central theme for this apparatus. In the previous chapter, magnetic fields provide a position-dependent detuning and corresponding scattering force for atoms confined in the MOT. In this chapter, purely magnetic trapping of atoms is discussed. In Section 1 I describe the types of magnetic traps used in BEC 2. Section 2 covers the magnetic coil system used for transferring atoms from the MOT chamber to either one of two science chambers. Finally, in Section 2, I discuss the trapping coils used for producing BECs. Special attention is given to our modular coil mounting structure (the "shuttle"), which allows for easily reconfigurable trapping potentials suited for a variety of vortex dynamics and turbulence experiments.

4.1 Magnetic trapping of neutral atoms

The potential energy of a neutral atom in a magnetic field is given by

$$U_B = -\vec{\mu} \cdot \vec{B} \tag{4.1}$$

where $\vec{\mu}$ is the atoms' magnetic dipole moment and $\vec{B}$ is the magnetic field. If the energy shift due to the external magnetic field is small compared to the ground state splitting, which in ^{87}Rb is 6.834 GHz, the atomic angular momentum quantum numbers, F and m_F serve as good quantum numbers. In this case, the energy in the presence of the field can be written as:

$$U_B = \mu_B m_F g_F |B| \tag{4.2}$$

where μ_B is the Bohr magneton, m_F is the quantum number for angular momentum about the axis defined by the local direction of $\vec{B}$, and g_F is the Lande g-factor associated with F. For ^{87}Rb in the $|F = 1, m_F = -1\rangle$ state, $g_F = -1/2$. We can create a magnetic trap by creating a magnetic field with a local minimum. For a magnetic field with a local minimum, the magnetic potential also has a local minimum for the so-called "weak field seeking" states, $|F = 1, m_F = -1\rangle$, $|F = 2, m_F = 2\rangle$ and $|F = 2, m_F = 1\rangle$ for ^{87}Rb and thus acts as a trap.[1] By moving the position of the local minimum in the field, we can transfer atoms from one location in the chamber to another.

An atom with magnetic moment m_F will precess about the magnetic field axis at the Larmor frequency $\omega_L = \mu_B m_F g_F B/\hbar$. The Larmor frequency sets the timescale for how quickly we can vary the magnetic fields in our system; that is, as long as the magnetic field is varied slowly with respect to the Larmor frequency, the magnetic moment will follow the external field and the spin state will be preserved.

4.1.1 Quadrupole magnetic field

An anti-Helmholtz coil pair is a pair of co-axial and identical magnetic field coils with equal and opposite current separated by a distance approximately equal to the radius of a coil. This configuration provides a simple method for trapping atoms: the quadrupole magnetic field. A quadrupole field has a local minimum in the magnitude of the magnetic field at the center of the coil pair. The field increases linearly away from the center point. Near the center of the coil pair, the field from

[1] See Dan Steck's notes on Rb properties for a discussion of the Zeeman effect and a table of the Lande g-factors for the ground states of Rb [65].

an anti-Helmholtz pair is given by:

$$B(\vec{r}) = \alpha x\hat{x} + \alpha y\hat{y} - 2\alpha z\hat{z} \tag{4.3}$$

where α is the magnetic field gradient in the $\hat{x}$ and $\hat{y}$ directions. Quadrupole fields work very well for trapping relatively high-temperature clouds where the atoms spend little or no time near the center of the field. At lower temperatures, Majorana losses, which are discussed in Section 4.1.3, make quadrupole fields ineffective due to atom loss in the region near B=0. At the end of our CMOT stage the cloud temperatures are still high enough that Majorana losses are not a significant loss mechanism and we can use quadrupole fields for trapping and transferring atoms from the MOT chamber to the science cell.

4.1.2 Transfer

Atoms can be transported quickly and efficiently using a moving quadrupole potential, which we accomplish using a series of partially overlapping quadrupole coils. By varying the current through adjacent pairs of coils, the B=0 point can smoothly transition from the center of one pair to the center of the adjacent pair; the effect is to move the location of the trap. Current through coil pairs is controlled from the lab computer by applying a voltage to the gate of a high-power transistor. This technique was first demonstrated by Griener *et al.* [74], and is now a well established technique for transferring atoms over large distances (up to a few tens of centimeters).

It is possible to transport atoms using this technique by energizing only two pairs of coils at a time. While straightforward, the aspect ratio of the trap, and as a result the shape of the cloud, changes significantly during the transfer and this

can lead to heating of the cloud. By adding a third coil, the trap aspect ratio can be held constant and thus heating is minimized.

4.1.3 The TOP trap

A major drawback of the quadrupole trap (or any trap with a zero minimum in the field) are losses due to non-adiabatic spin transistions, or Majorana losses [75]. As the temperature of the cloud decreases, atoms spend more and more time near the center of a quadrupole trap where the B-field goes to zero. As atoms approach the zero point in the field, their Larmor frequency, ω_L, also approaches zero. As a result, an atom's spin no longer follows changes in the magnetic field and has a high probability of being lost from the trap. Since the least energetic atoms spend the most time near the center of the trap, this loss mechanism affects primarily these atoms and prohibits cooling to BEC in a quadrupole trap.

A number of methods exist for magnetically trapping atoms in a non-zero minimum trap including the Ioffe-Pritchard trap [75, 76], quadrupole-Ioffe-configuration (QUIC) trap [77], and the plugged quadrupole trap [78]. In BEC 2 we have chosen to use a Time-averaged Orbiting Potential (TOP) trap, which is a time-dependent magnetic field that creates a harmonic trap with a non-zero minimum when averaging in time. The TOP trap technique was first demonstrated by W. Petrich *et al.* [79] and was used the magnetic trap in the first experimental demonstration of a dilute-gas BEC in 1995 [24].

A TOP trap is created by adding a rotating, constant-magnitude bias field to a quadrupole field. The effect of the bias field is to shift the center of quadrupole field to a position outside the extent of the atoms; the instantaneous field remains linear, with a zero point that rotates in space.

If the bias field rotates fast enough, the atoms cannot follow the instantaneous position of the trap minimum. We choose a rotation frequency ω_{TOP} such that:

$$\omega_{trap} << \omega_{TOP} << \omega_L \tag{4.4}$$

where ω_{trap} is the natural oscillation frequency of atoms in the time-averaged harmonic trap. In this case, the atoms occupy the region in space defined by the orginial quadrupole trap and the atoms' spins track the motion of center of the rotating bias field. Typically rotation frequencies of a few kiloHertz are sufficient for achieving these condidtions. In BEC 2, we use a 2 kHz rotating bias field. Equations 4.5 and 4.6 give the time-averaged potential to first order in the absence of gravity:

$$U_{TOP} \simeq \mu B_0 - \frac{\mu B'^2}{4B_0}\left(r^2 + 8z^2\right) \tag{4.5}$$

$$\simeq \mu B_0 + \frac{1}{2}m\omega_r^2 r^2 + \frac{1}{2}m\omega_z^2 z^2, \quad \omega_z = \sqrt{\frac{\mu B'^2}{mB_0}} = \sqrt{8}\omega_r \tag{4.6}$$

where, $B' = \partial B/\partial z|_{r=0}$, is the quadrupole field gradient in the z-direction and B_0 is the value of the instantaneous bias field, which rotates in a plane normal to $\hat{z}$. In Eq. 4.6 the TOP trap potential is written in terms of a harmonic oscillator where the oscillator frequencies in the radial and axial direcions, r and z, are ω_r and ω_z respectively. We often use the trap frequencies as an indication of the degree of confinement in a harmonic trap.

It is important to note that Majorana spin flips are not eliminated using this technique; instead, the troublesome zero-point of the field is shifted to positions far from the center of the quadrupole trap where only the most energetic atoms encounter the zero-point. Spin flips occur in a toroidal region in space defined by

the radius of the zero-point of the field. This region is affectionately called the "circle of death" since atoms that encounter this region are lost from the trap. The "circle of death" region occurs at $R_{COD} = 2B_0/B'$. The genius of the TOP trap is that it transforms non-adiabatic spin flips from a detrimental process that removes least energetic atoms from the center of the trap, to a beneficial process that removes only the most energetic atoms from the edges.

4.2 Transfer system in BEC 2

In BEC 2, we use a set of three coils to transfer atoms 11 cm from the center of the MOT chamber to either one of the two science chambers over a period of 1 sec, where they are transfered to a final pair of quadrupole coils that are concentric with the final transfer coil. The final pair of quadrupole coils is mounted on a removable shuttle along with several other coils used during the evaporation process towards BEC. The shuttle is discussed in detail in Section 4.3. Figure 4.1 shows a simplified geometry of our transfer coils located around the vacuum chamber.

The coil arrangement in Fig. 4.1 is chosen based on the following constraints:

1. The MOT/first transfer coil must be large enough for our 1.25" MOT beams to pass through the coils without obstructing the beams.

2. A commercial, high numerical aperture microscope objective (∼1.5" in diameter) and the mounting fixtures should fit comfortably inside the final transfer coil.

3. The axial separation of the coils must be large enough to clear the 1.65"-high walls of the octagonal MOT chamber.

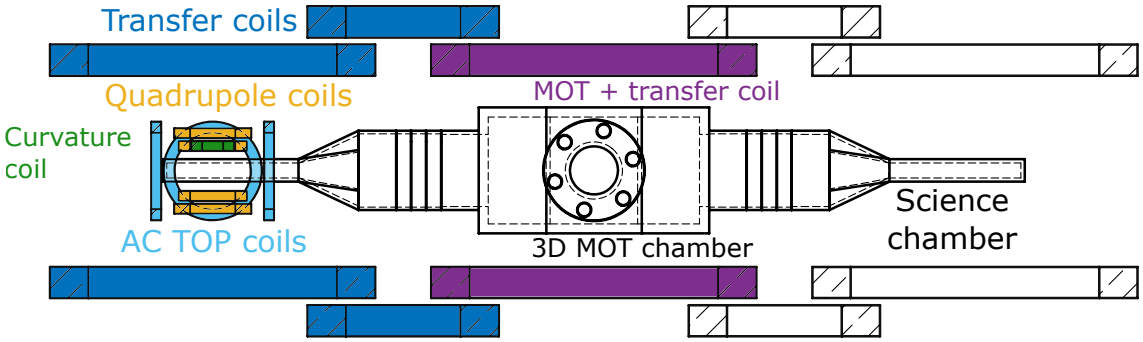

Figure 4.1: Diagram of the magnetic field coil system in BEC 2 located around the 3D MOT/BEC cell. Purple and dark blue coils comprise the magnetic transfer system. The center coil is colored puple as it also serves as the 3D MOT coil. The smaller coils around the science cell are the magnetic field coils that make up the final trap for the BEC. The quadrupole coils (yellow) and the AC TOP bias coils (light blue) make up the TOP trap which is discussed in this chapter. The quadrupole coils and the curvature coil (green) make up the gravito-magnetic trap, which is discussed in Ch. 7.

4. We would like to use as few coils as possible to minimize the number of computer-controlled voltages required to operate the transfer.

5. A single commercially available power supply must be able to provide the maximum total current used during the transfer sequence and the heat generated during the transfer process should be removable by a modest amount of water cooling of the mounting structure for the coils.

4.2.1 Calculation of currents

We calculate the current sequence required for transferring atoms numerically by calculating the local magnetic field near the atoms in three dimensions at all positions during the transfer. We enforce the following conditions, that dictate the currents flowing through the coils that are in operation at any point during the transfer:

1. The magnetic field at the center of the trap at any position during the transfer sequence must be identically zero.

2. The gradient in the z-direction (axis of symmetry of the coils), $\partial B/\partial z$, remains constant during the transfer

3. The gradient in the x-direction (transfer axis), $\partial B/\partial x$, remains constant during the transfer.

The shape of the atom cloud during the transfer is determined by the aspect ratio $\partial B/\partial z$:$\partial B/\partial x$. Requiring that $\partial B/\partial z$ and $\partial B/\partial x$ remain constant minimizes heating due to changes in the shape of the cloud.[2]

The local magnetic field and the magnetic field gradients in three dimensions are determined numerically. The magnetic field from a single loop of current, I, perpendicular to the z-axis, with radius, R, centered at $z = A$ has a known, closed form, which can be found in Ref. [80]. Equations 4.7 and 4.8 give the magnetic field component in the radial and axial directions as a function ρ and z, the radial and axial coordinates, respectively:

$$B_\rho = \frac{\mu_o I}{2\pi} \frac{1}{[(R+\rho)^2 + (z-A)^2]^{1/2}} \cdot \left[K(k^2) + \frac{R^2 - \rho^2 - (z-A)^2}{(R-\rho)^2 + (z-A)^2} E(k^2) \right] \tag{4.7}$$

$$B_z = \frac{\mu_o I}{2\pi\rho} \frac{z-A}{[(R+\rho)^2 + (z-A)^2]^{1/2}} \cdot \left[-K(k^2) + \frac{R^2 + \rho^2 + (z-A)^2}{(R-\rho)^2 + (z-A)^2} E(k^2) \right] \tag{4.8}$$

[2] At the beginning and end of the transfer sequence where there are only at most two coils on at a given time, we relax the conditions on the gradient of the field. For the regions of the transfer where up to two coils are on, we only require that $\partial B/\partial x$ remain constant and that $\partial B/\partial z$ changes continuously.

where μ_o is the vacuum permeability, and

$$k^2 = \frac{4R\rho}{(R+\rho)^2 + (z-A)^2} \tag{4.9}$$

is the argument of the complete elliptic integrals K and E. Notice that the magnetic field distribution can be written in the form

$$B_\rho = \beta_\rho(\rho, z)I \tag{4.10}$$

$$B_z = \beta_z(\rho, z)I \tag{4.11}$$

where the fields in ρ and z are proportional to the current through the coils and the constants of proportionality, β_ρ and β_z, carry information about the geometry of the coil.

We reduce the geometry of each coil (i.e. inner radius, outer radius, coil thickness, wire thickness, number of turns and distance from the transfer axis) into a single, zero thickness coil with an effective radius and distance from the atoms. We then determine the local magnetic field (and the field gradients) as a function of position along the transfer axis by summing up the field contributions from each of the three coils in operation. The conditions described above can be written in terms of a set of equations that depend linearly on the currents in the three coils:

$$I_1 B_1(x,0,0) + I_2 B_2(x,0,0) + I_3 B_3(x,0,0) = 0 \tag{4.12}$$

$$I_1 \frac{\partial B_1(x,0,0)}{\partial z} + I_2 \frac{\partial B_2(x,0,0)}{\partial z} + I_3 \frac{\partial B_3(x,0,0)}{\partial z} = \frac{\partial B_0(x)}{\partial z} \tag{4.13}$$

$$I_1 \frac{\partial B_1(x,0,0)}{\partial x} + I_2 \frac{\partial B_2(x,0,0)}{\partial x} + I_3 \frac{\partial B_3(x,0,0)}{\partial x} = \frac{\partial B_0(x)}{\partial x} \tag{4.14}$$

Coil	R_{inner}(in)	z_{mount}(in)	$x_{transfer}$(in)	N_{turns}
1	3.5	1.25	-5	40
2	1.5	1.75	-2.5	47
3 (MOT)	3.5	1.25	0	45
4	1.5	1.75	2.5	47
5	3.5	1.25	5	40

Table 4.1: Coil geometries for the five transfer coils.

These are expressed in matrix form as follows:

$$\vec{b} = \begin{bmatrix} |B_0(\vec{x})| \\ \partial B_0(x)/\partial z \\ \partial B_0(x)/\partial x \end{bmatrix} = \begin{bmatrix} 0 \\ 127 \text{ G/cm} \\ \text{-42 G/cm} \end{bmatrix} = \begin{bmatrix} \beta_{11}(x) & \beta_{12}(x) & \beta_{13}(x) \\ \beta_{21}(x) & \beta_{22}(x) & \beta_{23}(x) \\ \beta_{31}(x) & \beta_{32}(x) & \beta_{33}(x) \end{bmatrix} \cdot \begin{bmatrix} I_1(x) \\ I_2(x) \\ I_3(x) \end{bmatrix} \tag{4.15}$$

where $B_0(x)$ refers to the magnetic field at the position (x,0,0) and the elements of matrix $\beta(x)$ are the coefficients of Eqs. 4.12, 4.13 and 4.14. The values $\partial B/\partial x$ = 127 G/cm and $\partial B/\partial x$ = -42 G/cm are the values chosen for our current transfer conditions. We calculate the matrix $\beta(x)$ for a discrete set of positions, x, along the transfer axis. Then the currents as a function of the transfer position are given by

$$I_j(x) = \beta(x)^{-1} b_j \quad j \in \{1, 2, 3\}. \tag{4.16}$$

Fig. 4.2 show a calculation of the currents $\vec{I}$ and the corresponding field gradients for a transfer where $\partial B/\partial z$ and $\partial B/\partial x$ are chose according to Eq. 16.

The final coil geometries and arrangements for the transfer system were chosen by experimenting with different coil geometries, field gradients and total current values. The final transfer coil pair parameters are given in Table 4.1.

In the above discussion, the transfer currents are calculated only as a function of position of the trap minimum. In practice, the velocity of atoms (which determine

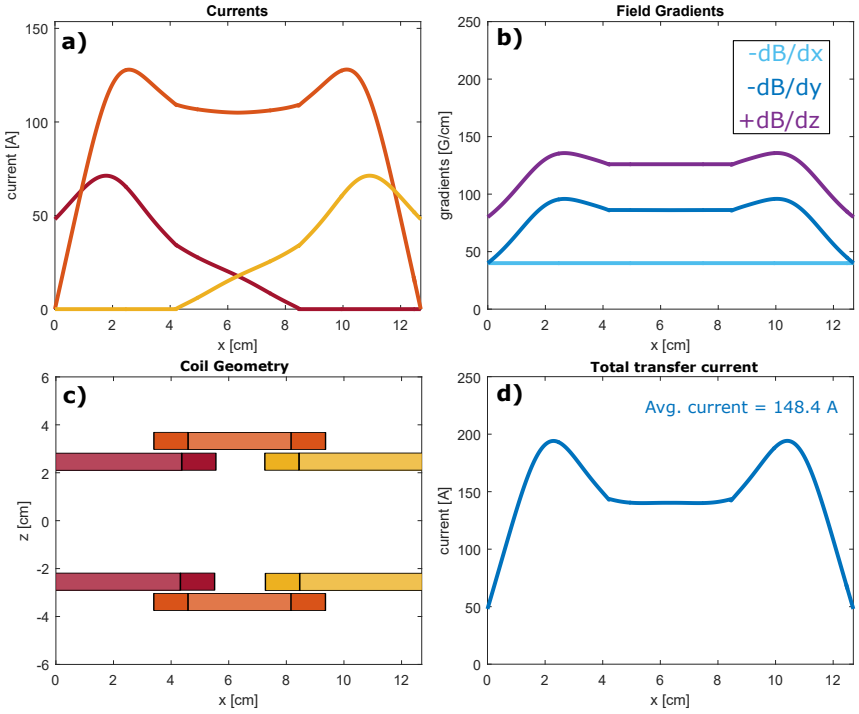

Figure 4.2: Simulations of the transfer current. a) and c) Current in the three transfer coils as a function of position during the transfer. In these figures red represents the MOT coil, orange is the middle transfer coil and yellow is the final transfer coil. d) Shows a sum of the three transfer currents as a check to make sure the total current does not exceed 200 A. b) Field grandients in x,y and z (which determine the aspect ratio of the trap) as a function of position during the transfer. During the middle sections of the transfer, the aspect ratio remains constant which is a condition for our transfer.

the total transfer time) during the transfer process is also an important parameter. The transfer must be slow enough that the atoms do not incur unwanted heating but quick enough so that we don't overheat (and possibly burn) the transfer coils in the process. Since the transfer process requires currents in excess of 190 A, overheating the coils is a serious concern (and one that is discussed later in this chapter with regards to safety interlocks). We have experimentally settled on a sequence where the atoms are transported from MOT cell to science cell over 1 sec at constant velocity. We have also experimented with non-linear velocity ramps, thinking

that we might minimize heating by accelerating atoms slowly. Ultimately we found alternative velocity ramps do not affect the number of atoms or the temperature significantly and thus we have chosen not to implement them.

4.2.2 Physical design of the coils and the coil mount

The coils used in the tansfer system are wound using 0.5" wide by 0.01" thick copper tape with a 0.0012" thick Kapton® backing. The copper tape was purchased from Bridgeport Magnetics, Inc. We have chosen to use Kapton backed copper tape over traditional magnet wire as it simplifies the coil winding process significantly and improves the packing fraction of copper to insulation by eliminating air gaps between coil layers. In addition, the copper tape coils have exposed copper on the top and bottom of the coil which aids in dissipating heat from the coils during the transfer process.

Figure 4.3 shows an example of a transfer coil used in BEC 1 compared to one of the transfer coils in BEC 2. We wind coils on a set of home built coil forms on the coil winding jig shown in the figure.[3] The copper tape is somewhat stiff and a modest amount of tension is sufficient to hold the coils together during the winding process. After the coils have been wound and removed from the jig a few layers of Kapton tape wrapped around the outside of the coils is enough to keep the coils from unravelling. In addition to providing structural support, the Kapton tape adds another layer of electrical insulation from the mount. After winding and taping coils, we apply a small amount of thermally conductive (but electrically insulating) epoxy to the bottom of each coil to prevent the coil from shorting to the aluminum mount and to further stabilize the coil. Figure 4.3 gives an overview of the coil winding

[3]Thanks to Prof. Jose Sasian for donating his coil winding machine to the BEC group.

Figure 4.3: Overview of the transfer coil winding process. The image in d) shows the coil winding machine and the jig we use to wind the large transfer coils. c) A photo taken during winding process. Coil winding can be accomplished by one person; an extra set of hands makes the coil winding process very simple. a) and b) Show the difference between the transfer coils in BEC 1 (b) and BEC 2 (a). Coils wound with the thick copper tape are much more uniform and are easier to wind. e) Shows a close up view of one of the transfer coils and demonstrates the uniformity and regularity of the copper tape-style coils. The uniformity in winding leads to more efficient heat dissipation.

process.

The top and bottom coil sets are each mounted on a single block of aluminum that has been machined so that individual coils are positioned precisely in the locations given in Tab. 4.1 and fit snuggly in the mount. Coils are epoxied to the mount using a high thermal conductivity made by Epoxies Etc (50-3100RBK), a high viscosity, two part epoxy. This ensures the epoxy has a long shelf life; we've used the same batch of epoxy on all of the coils in our transfer/shuttle system. The high viscosity of the epoxy allows us to apply epoxy precisely, like a thick paint. Once epoxy has been applied and the coils are set in place, the epoxy cures over a period of 24 hours at room temperature (at elevated temperatures around 75°C the curing process only takes ∼2 hours).

Figure 4.4 shows drawings of the mount along with pictures of the mount during

the coil installation process and in its final position over the MOT/BEC chamber. The drawing indicates a few important features of the coil mounts. First, a series of 1/2-inch channels are drilled through the mount which are used for water cooling the mount and the attached coils. We use a Neslabs ThermoFlex 900 water chiller to water cool the mounts.[4] A second feature of the mount are the slits cut through three of four sides. We place slits in the transfer coil mount (and the shuttle mounts) to prevent eddy currents from flowing through the mount when coils are turned on and off. This can be especially problematic for atoms in the BEC which are sensitive to stray magnetic fields. By avoiding extraneous fields due to eddy currents, we hope to minimize the shot-to-shot differences between runs of the experiment. The mount also has a number of 1/4-20 tapped holes which come in handy for mounting optics close to the cell. In fact, the vertical beam expanders for the 3D MOT are mounted directly onto the transfer coil mount. Lastly, Fig. 4.4, shows a pair of 1/8-inch tracks machined into the underside of the transfer mount. The tracks allow for precise positioning of the shuttle that holds the magnetic field coils for the final stages of atom trapping. The shuttle is a small aluminum insert which slides into place inside the transfer coil mount and around the cell. The length of the tracks were chosen such that the center mounted on the shuttle are concentric with the final transfer coil pair. The quadrupole coils used for forming the BEC and shown in Fig. 4.1 are mounted on the shuttle. The tracks also allow the shuttle to be taken in and out of the transfer mount easily and repeatably.

[4]We cool the mount to 15.5°C. We choose this temperature to avoid condensation on the mounts dripping on the vacuum chamber/optics in the summer, a problem that we've experience in BEC 1 where the building's chilled water supply is used. 15.5°C is a few degees above the maximum average dew point in Tucson, so the mount stays cold during routine operation of the experiment. We haven't noticed any condensation forming on the mount.

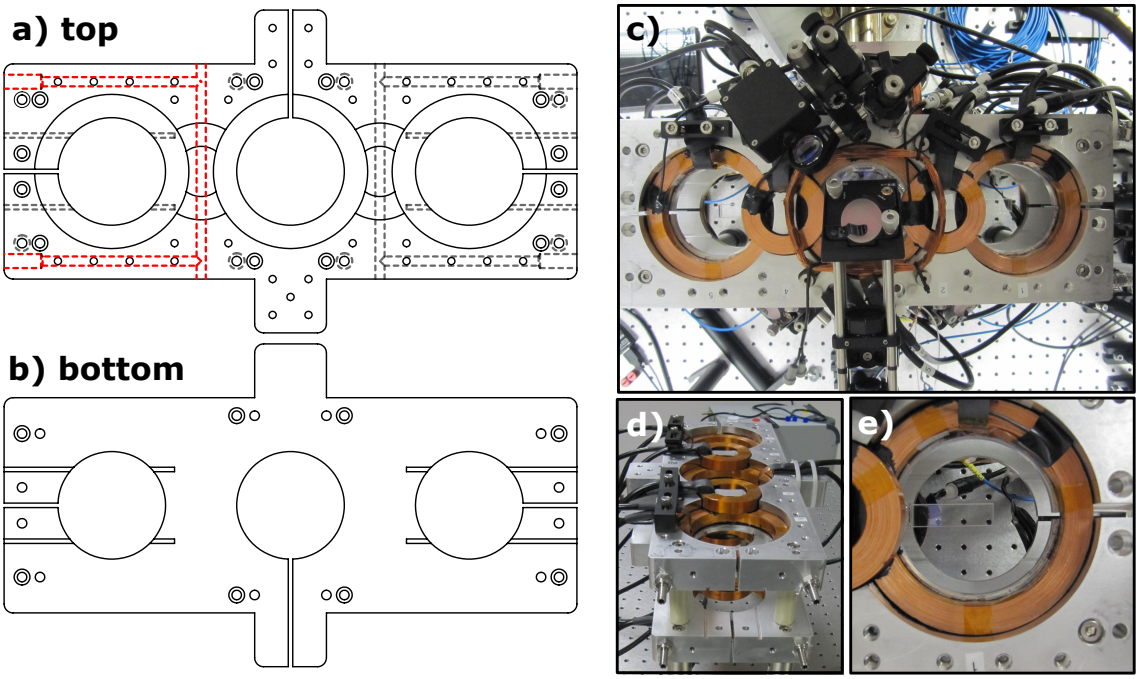

Figure 4.4: a) Top and b) bottom view diagrams of the transfer coil mount. Red dotted lines show the water cooling channels drilled into the mount. d) Side view image of the transfer coil mount after coils have been expoxied and the wire connections have been made. c) Top view of of the transfer coil mount after positioning it in place around the glass cell and all of the MOT optics have been set up. e) A close up view of the BEC cell in the center of the final transfer coil. At the top right corner of the image is one of the thermistors used to monitor coil temperature for the power supply interlock.

Once all the coils are epoxied in placed, the two pieces of the mount are bolted together using a set of 2" ceramic spacers to separate the mounts. The mounts are separated by two inches so that the insides of the aluminum mount clear the octagonal MOT chamber by 1/8-inch on either side of the cell. The ceramic spacers prevent eddy currents from developing between the two coil mount pieces.

Before installing the transfer coil mount around the cell, we measure the magnetic field gradients for each of the five coils in the transfer system. Figure 4.5 shows plots of the gradients for each of the coils.

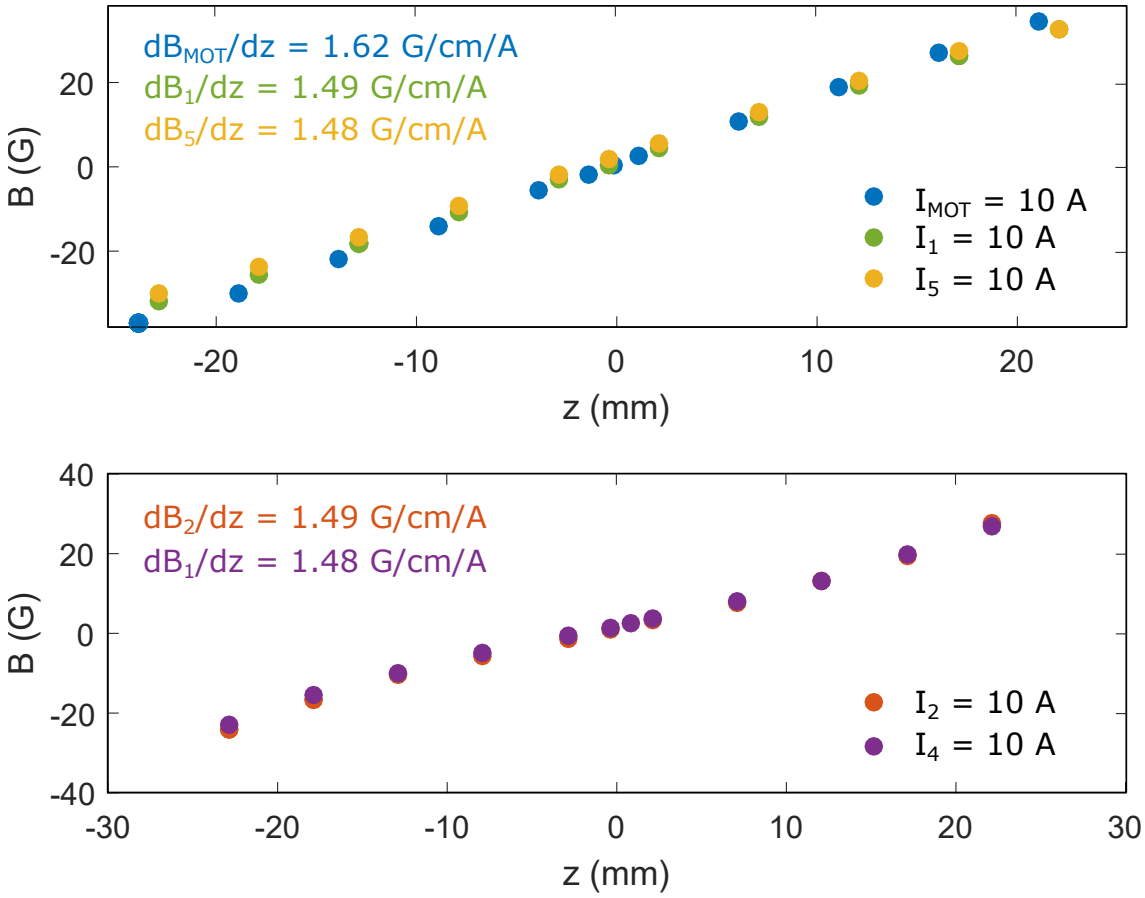

Figure 4.5: Plots of the B-field along the axis of each of the five transfer coils measured offline with an F.W. Bell 5070 Gaussmeter. We measure the field strengths for a 10 A current in all coils.

4.2.3 Controlling the transfer current - high power electronics

We use a TDK Lambda Genesys 50-200 10kW power supply to drive current in the transfer coils. The Gen 50-200 can supply up to 200 A at 50 V. We operate the power supply in constant voltage mode at 20 V. The ground for the power supply is directly to the building ground, which serves as the central ground for the lab. The lab grounding protocol is discussed in Appendix B. Since we use a single power supply to drive current in all the coils we use a series of high power MOSFETs made by IXYS Corp (model number IXFN180N10) to regulate current through individual

coil pairs in the transfer system. We operate the power supply at the lowest possible voltage that will allow the full transfer current (V=IR), which corresponds to the minimum power per MOSFET. Each pair of coils is assigned a set of two MOSFETs that each regulate half the current through the coil. The MOSFETs are mounted on a water cooled plate that is directly connected to the power supply return and serves as the ground for all the MOSFETs.

We use two MOSFETs per coil pair due to the fact the IXFN180N10 MOSFETs have a maximum power rating of 600W. We divide the total current in the coil in each coil pair between two MOSFETs so that each MOSFET runs at half the total current power. This reduces the chance of failure during a single run and increases the lifetime of the MOSFETs in our system. At a drain-source voltage of 20V, even a modest continuous current of 30 A would destroy the MOSFETs. Since we operate the MOSFETs with a duty cycle of $\sim$1 sec every 3-4 min, we can afford to run at much higher powers. Figure 4.6 shows an image of the MOSFET bank mounted on the water-cooled plate. With the water cooling and the short duty cycle, we are able to run upwards of 60A through individual MOSFETs for short periods. In addition, since we control the gate voltages of the two MOSFETs independently, if one of the pair of MOSFETs for a given coil blows, the other is not at risk from a high current dump.

The current through each MOSFET is controlled by an analog voltage from the lab computer determined by the current ramps discussed in section 5.2.1. An FW Bell CLSM 200-LA Closed-Loop Hall effect sensor monitors the current flowing through each coil pair and is used in a feedback loop to stabilize current. The feedback loop for controlling the transfer current is discussed in more detail in section 5.2.4. Flyback diodes are installed across the coil pairs to protect MOSFETs from

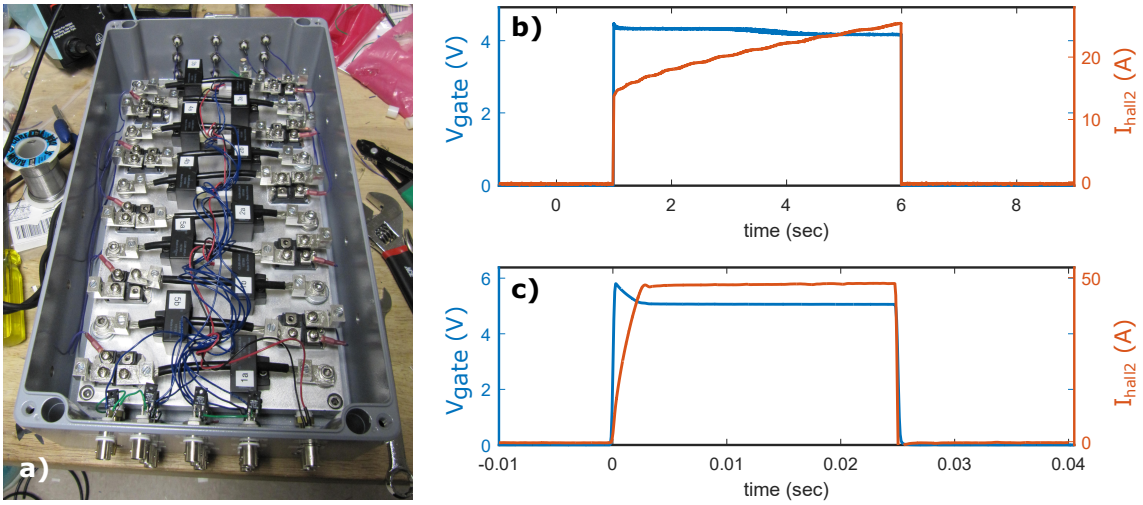

Figure 4.6: a) Image showing the layout of the transfer coil MOSFETs and Hall probes. b) and c) show plots of the current (red) and gate voltage (blue) through a single coil pair in response to a square pulse input from the timing computer. b) Shows the response current for a 5 sec square input without feedback. With no feedback the current increases during the pulse as the MOSFET heats up. There is a corresponding drop in gate voltage as the current increases. c) Shows the current through a coil with feedback for a short pulse of 25 msec. With feedback, current remains constant for the duration of the pulse. The pulse duration in c) is chosen to show the non-zero turn-on time due to the inductance of the coils. For currents around 50 A, the transfer coils turn on to full value in ∼1-2 msec.

large induced voltages (-L$\frac{\partial I}{\partial t}$) when current is switched off quickly. Figure 4.8 shows a diagram of the high power side of the transfer current control system.

In the event that the current control system fails, an interlock circuit can disable the power supply protecting the coils and other components of the transfer system from being damaged. Figure 4.7 shows a diagram of the interlock circuit. The interlock will disable the TDK power supply in the event that one of the hall probes measures too high a current passing through one or all of the coils, if any one of ten thermistors epoxied directly to the transfer coils measures a temperature significantly above normal operating conditions, or if the water cooling is shut off.

The MOSFET source terminals are connected to the power supply ground via

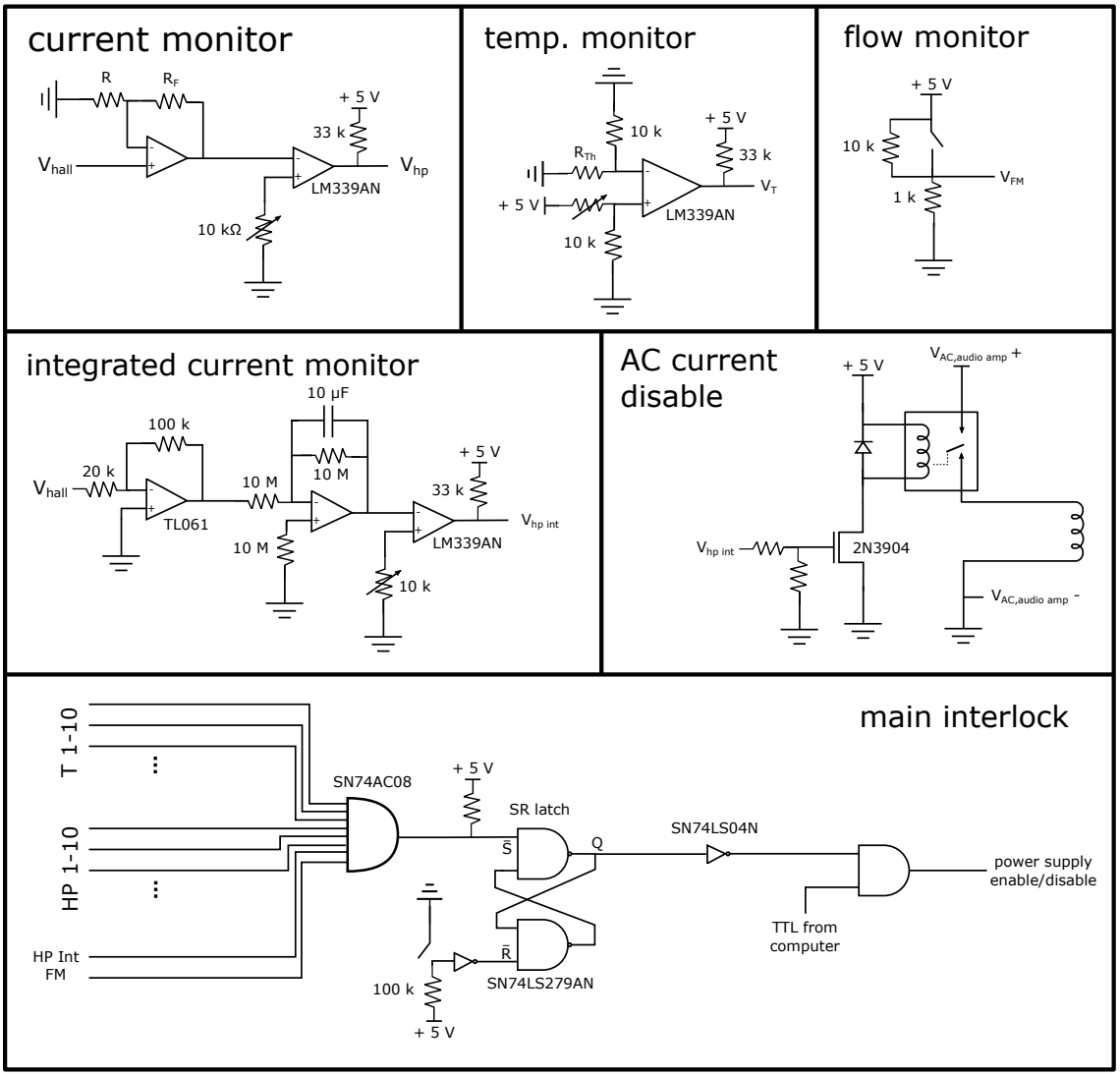

Figure 4.7: Circuit diagrams for the various interlock on the transfer and shuttle coil systems.

three, size 3 AWG cables so there is essentially zero resistance between the power supply ground and the MOSFET ground. Although this seems like a relatively trivial detail, at the high currents during transfer, the fact that this ground line has a non-zero resistance means we have a transfer current dependent voltage shift at the source of the MOSFETs. Since the current through a coil pair is controlled by the G-S voltage for the MOSFETs assigned to that coil pair, a few hundred mV change in the G-S voltage has a substantial effect on the current flowing through all the coil pairs. A single, 10 ft long, size 3 AWG wire has a resistance of 0.002 Ohms. At the highest transfer currents(∼200 A) this would correspond to a change in the G-S voltage of 0.4 V.

4.2.4 Transfer current feedback

The high currents during transfer lead to temperature-dependent changes in the current through the transfer coil pairs. We use a feedback loop to stabilize the transfer current from temperature dependent drifts that would lead to changes in the magnetic fields. The feedback circuit is based on the feedback circuit for the transfer system in BEC 1, which was designed by M. David Henry.[5] Figure 4.8 a) gives a conceptual schematic of one channel of the feedback circuit. In this pared-down form, the circuit consists of a single op-amp with negative feedback determined by the current flowing through the MOSFET. When no current is flowing through the resistor, R, the op-amp's inverting input, V_{-},is grounded. If a positive voltage is applied to the non-inverting terminal of the op-amp, V_{+}, the output voltage, V_{out}, of the op-amp rises and the MOSFET will turn on allowing current to flow through the resistor. When current flows through R, V_{-} rises to the point where $V_{-} = V_{+}$. If

[5]For more details on the feedback circuit design see David Henry's undergraduate honors thesis.

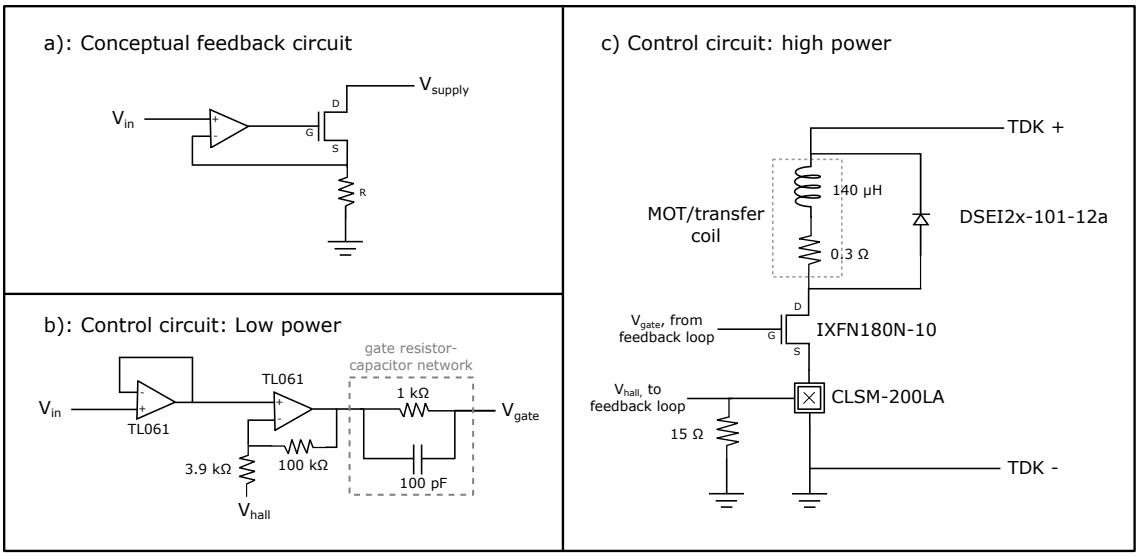

Figure 4.8: Transfer coil feedback electronics.

too much current flows through the resisor, such that $V_- > V_+$, V_{out} decreases and the MOSFET restricts current flow through the resistor until $V_- = V_+$ again. In this conceptual example, the resistor acts as a current monitor through the MOSFET and provides a path for feedback.

This architecture has several advantages over driving the MOSFET directly from the computer with no feedback circuit. First, the presence of feedback linearizes current through the MOSFET as a function of the gate voltage, which would otherwise be proportional to V_{gate}^2 according to the square-law theory of FETs [81]. Second, the characteristics of each MOSFET vary for the individual device. The same gate voltage can result in D-S currents that differ by tens of amps between individual devices. By using a feedback circuit, we shift the sensitivity of the output from the MOSFET to the resistor (or other methods for monitoring current) which can be very precise. Third, the op-amp helps to supply the MOSFET gate with enough charge to operate the MOSFET. Most importantly, feedback allows repeatable current control from shot to shot and prevents thermal runaway.

In the above example, a resistor is used to monitor current flow through the MOSFET. At the currents used during our transfer sequence, hundreds of amps at D-S voltages of tens of volts, kW power, precision resistors would be required to operate the control circuit. In addition to the fact that resistors like this are impractical and expensive, the added resistance would limit the maximum current. In place of a resistor, we use a Hall Probe, which is a current sensing device that outputs a voltage (or current) proportional to the measured current. Figure 4.8 shows a diagram of the high and low power sections of the transfer current control system.

The last element of the feedback circuit is a resistor-capacitor pair between the output of the op-amp and the MOSFET gate. By adjusting the values in this pair of components we can adjust the gain bandwidth of the feedback loop.

Simulations of the control circuit were performed in LTSpice, an open-source circuit simulation package. The transient current and voltage response to a 10 ms, square voltage input voltage were calculated for a range of input voltage levels and component values. In these simulations, the D-S voltage is a quantity of particular interest as fast ringing in the D-S voltage at a circuit resonance will also result in ringing in the current through the coils. Small-signal, AC analysis of the control circuit was also performed in order to understand how the output resistor-capacitor pair affects the loop gain. Figure 4.9 shows transient and AC simulations of the control circuit response.

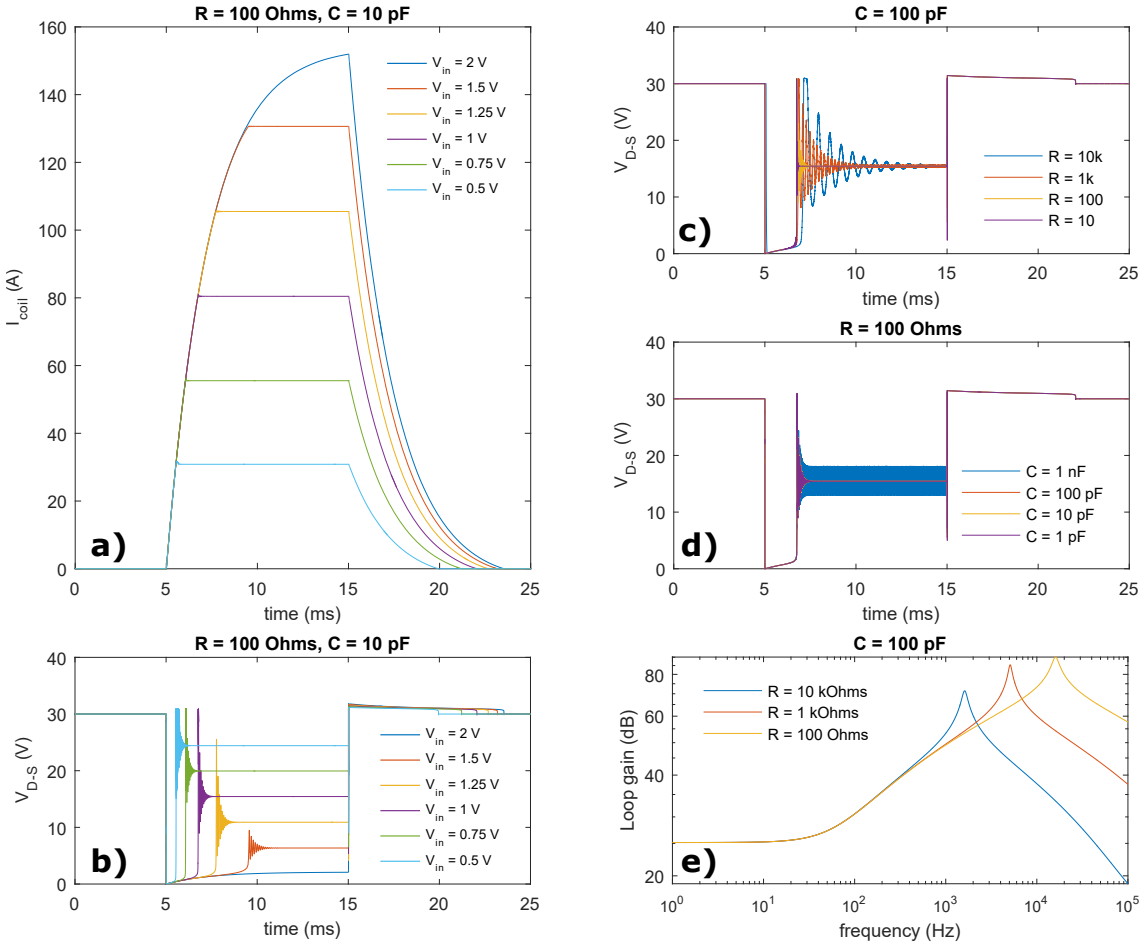

Figure 4.9: Current simulations for transfer feedback system. Plots a) and b) Show the current and voltage response to a 10 msec square pulse input of varying amplitudes. Plots c) and d) show the amount of ringing on the gate voltage as a function of the resistor and capacitor values in the gate network. e) Small-signal AC analysis shows that the frequency response for smaller RC constants moves to higher frequencies. This matches the trend in the gate voltage simulations.

4.3 BEC coils

The final trap coils and rf coils for BEC 2 are mounted on a small removable mount that slides and bolts into the transfer coil mount, which we refer to as the shuttle.[6] A number of considerations went into the design of the shuttle; these are listed below:

1. The shuttle is designed so that the magnetic field coils that make up the final trap are as close to the cell as possible without risk of damaging the cell or heating the cell during regular operation. This serves two purposes: First, having the coils close to the cell, given our thin cell, allows us good optical access to the atoms. Based on observations of *in situ* images of vortex lattices in BEC 1 and theoretical predictions on the closest approach of two vortices in typical turbulence experiments [82], we anticipate needing an imaging system with a numerical aperture of ~ 0.3. Ideal measurements from our CAD drawings show that we should be able to use imagings systems with NA up to 0.46.

   Second, placing magnetic field coils close to the cell allows for strong magnetic confinement at modest currents. In BEC 1, the tightest trap frequencies are achieved by running 20 A through the final trap coils. In BEC 2, the final trap coils use 3.5 A at our highest trap frequencies.

2. The shuttle is machined out of aluminum and serves as a heat sink for the coils. The shuttle is bolted directly into the transfer coil mount and we can use the water cooling in the transfer mount to cool the shuttle. Since we use

[6] The shuttle, along with all the accessory pieces were machined at the University Research Instrumentation Center (URIC). The designs should be on file if duplicates of the any of the parts need to be made.

relatively thin, high resistance wires for our coils we generate enough heat that the coils warm up during everyday operation; without water cooling, the polyester backing on the coils would likely melt.

3. The shuttle is actually composed of four pieces. A center coil mount (with several attachable plates for accesory coils), and two sleds, with the larger sled being made of two pieces. On close inspection, the central coil mount has three small slits cut out of the mount in orthogonal directions. The purpose of these slits is to prevent induced eddy currents from affecting the atoms. The two halves of the large sled are electrically isolated with Kapton tape for the same reason.

4. The shuttle has been designed to be easily removable and reconfigurable. With the exception of the TOP coils, the final magnetic field coils are all epoxied to aluminum plates that bolt onto the center piece of the shuttle, which serves as the coil mount. The TOP coils are epoxied directly to the center coil mount, but can be reconfigured by replacing the center mounting piece.

   The center piece of the shuttle is bolted onto two sleds. Wiring from the power supply is attached to the coils via a set of plastic terminal blocks, which are attached to the sleds. The wires connected directly to the coils are flush with the sleds so that the sled can be easily removed without untangling coils.

   Each of the sleds has a set of 1/8-inch runners that slide into the tracks on the transfer coil mount. The runners allow us to align the final trapping coils to be concentric with the last transfer coil.

   Our hope is that by making the magnetic trapping geometries reconfigurable, we will be able Opto perform a wide range of experiments. In addition, the

modular nature of the shuttle allows us to replace broken components relatively easily, without having to realign optical systems or reposition trapping coils. We've been able to trap atoms in the final quadrupole trap, remove and replace the shuttle, and trap atoms in the same position in the cell within a matter of minutes.

The coils mounted on the shuttle are made of 0.125" wide by 0.001", polyester backed (one side only) copper tape purchased from Bridgeport Magnetics and were wound using the same coil winding jig use that was use to wind the transfer coils (with different forms). We also epoxy coils to the mounting plates with the same epoxy used for the transfer mount. Since the final trap coils are relatively small, once epoxy is applied, we are able to bake the epoxy at 75°C for 2 hours until cured. Once all the coils are epoxied and connections are made, the shuttle is positioned in place inside the transfer coil mount.

Figure 4.11 shows diagrams of the center piece of the shuttle and a diagram of the coils and their locations relative to position of the atoms in the science cell. Table 4.2 gives further details about the coil construction. Figure 4.10 shows photographs of the shuttle during construction and installation.

There are four sets of coils used at present in the production and manipulation of the BEC. Three of these are shown in Fig. 4.11. The four sets of coils are described in detail below.

4.3.1 Quadrupole coils

In BEC 2, the final quadrupole trap consists of two pairs of asymetric anti-Helmholtz coils as shown in Fig. 4.11. The two sets of anti-Helmholtz coils operate in parallel and for the purposes of this discussion can be considered one large, symmetric

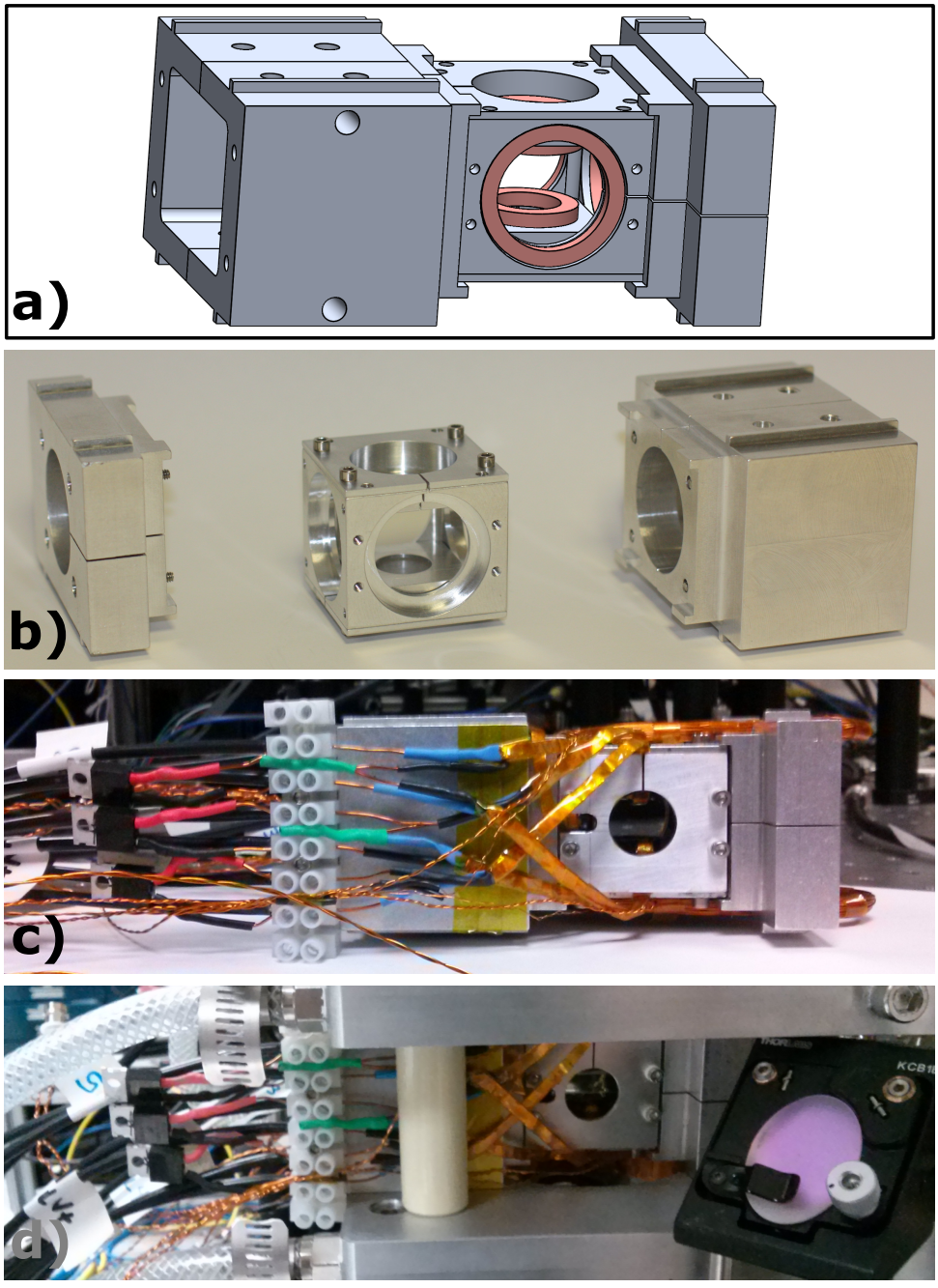

Figure 4.10: a) A CAD rendering of the shuttle with the coils attached. Images b) - d) show the shuttle in various stages of preparation. c) shows the shuttle fully assembled and ready to be installed in the transfer mount. On the left side of the mount, small fly-back diodes for the coils are visible.

quadrupole coil. The inner coil and outer coil of each pair is located 8.32 mm and 12.5 mm from the position of the atoms respectively. Both inner and outer coils have a 7.5 mm inner radius; only the number of turns differs between the two sets of coils.

4.3.2 Rotating bias field coils (a.k.a. AC TOP coils)

The rotating bias field coils consist of two pairs of perpendicular, 1" diameter coils arranged in a Helmholtz configuration. Each pair of TOP coils provides a roughly constant 10 G/A bias field over the volume of the science chamber. We run a 2 kHz, AC current through the TOP coils during TOP trap operation. The current in the two pairs is out of phase by 90° in the two channels providing the rotation of the bias field.

4.3.3 "Curvature" coil

The "curvature" coil is a bias coil that is concentric with the quadrupole coils and mounted on the upper quadrupole coil mounting plate. As discussed in Ch. 6, we use this coil, in conjunction with the quadrupole coils to generate a gravito-magnetc (GM) harmonic trap for the BEC with a well defined magnetic field axis parallel to gravity.

4.3.4 rf coils

The last set of coils, which is not shown in the figure, are the rf coils, which are arranged in a helmholtz configuration and are wound directly around the two inner quadrupole coils. Figure 5.1 shows an image of one of the rf coils.

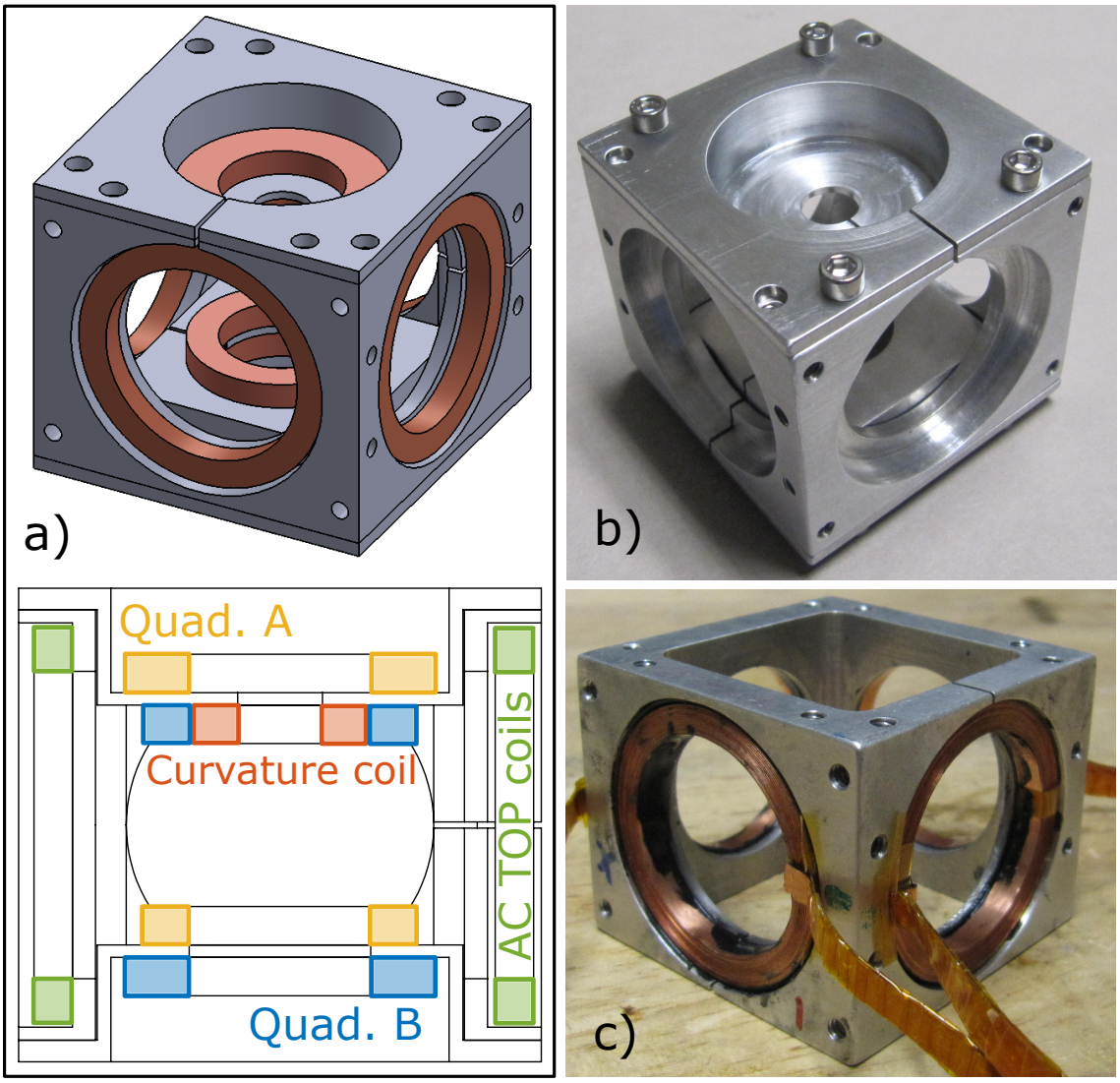

Figure 4.11: a) and d) Drawings of the center piece of the shuttle showing the various coils used in the final trap for the BEC. b) and c) Pictures of the shuttle before and after the coils have been epoxied.

Coil	N_{turns}	r_{inner}(mm)	r_{avg}(mm)	d_{BEC}(mm)
$Quad_{outer}$	69	7.5	10.12	12.51
$Quad_{inner}$	50	7.5	9.4	8.32
GM Curvature	50	3.5	5.4	8.32
TOP	50	12.7	14.6	18.74
Bias	40	8.5	10.02	25.72
Quic 1	32	2.5	3.72	10.38
Quic 2	40	8.5	10.02	20.00

Table 4.2: Coil geometries for the shuttle coils. Column 5 gives the distance

4.3.5 Shuttle coil electronics

Since the transfer coils and the final magnetic trap coils run at much different powers (a few kiloWatts for the transfer coils compared to a few tens of Watts for the shuttle coils), we have chosen to run the two sets of coils using separate power supplies. The major benefit of using separate supplies is that typically the rms current ripple on DC power supplies is proportional to the total power. At low atom cloud temperatures, atoms are very sensitive to current fluctuations in trapping coils, so we reduce heating by using low power, low current ripple supplies for the final trap coils. In addition, current noise on the transfer coil does not couple to the BEC coils and vice versa.

The final magnetic trap coils are powered by two Aligent 6642A 20 V, 10 A power supplies. The quadrupole coils are run off one power supply and the curvature coil (and two QUIC coils) runs off the second. We regulate the current through the BEC coils using International Rectifier IFRP250N power MOSFETs. The IRFP250N can handle up to 250 Watts at room temperature without failing. Since we run at most 50 Watts through the BEC coils at any point in time, we do not water cool the MOSFETs for the BEC coils.

As with the transfer coils, we control the current through the Hall probes using an

analog voltage from the lab computer. We stabilize the coils by providing feedback from a set of LEM LAH25-NP Hall effect transducers. For the BEC coils, we use a true, error signal feedback circuit. In this case, the current through the Hall probe is compared a set voltage from the computer, and the difference between the two signals is added to the set point voltage and sent to the gate of the MOSFET. Our hope in choosing to use a redesigned feedback circuit for the BEC coils was that although this type of circuit was requires more components, it would ultimately be more stable than the feedback circuits in BEC 1.[7] An interlock circuit, similar to the transfer coil interlock, protects the power supplies from damaging the BEC coils in the event of a failure.

The AC current for the rotating bias field is supplied using a Crown XLS602 power audio amplifier. Since our AC TOP coils are essentially voice coils for speakers (minus the permanent magnets and speaker membranes), audio amplifiers are a convenient, and cheap way of generating the AC currents needed to run the TOP trap.[8] The 2 kHz drive voltage for the TOP coils comes from a two channel function generator; during the evaporation sequence we modulate the amplitude directly from one of the analog output voltages from the computer. A separate interlock protects the AC TOP coils from being damaged by the audio amplifier; in the event that either the peak current or the temperature of the TOP coils rises above some set point, a set of relays disconnects the TOP coils from the amplifier. Figure 4.7 shows a diagram of the AC interlock used for the AC TOP coils.

[7] We have only tested the new circuit design for the BEC coils while the older design is used for the transfer coils, so we do not really have a good sense of the differences between the two circuits. Both circuits work so we don't have a reason to change either design.

[8] As an interesting aside, it's not uncommon to hear the 4 kHz, AC TOP coils in BEC 1. In the presence of other magnets in the system, they actually vibrate and produce a very audible, high pitch note.

CHAPTER 5

Evaporation Process and BEC

Forced evaporation provides a process by which phase space density of atoms in a magnetic trap can be increased dramatically. In Section 1, I discuss the process of evaporative cooling and the implementation of these techniques in BEC 2. In Section 2, I discuss our imaging system and finally the formation of a BEC in the new apparatus.

5.1 Evaporative cooling

Evaporative cooling refers to a process in which energetic particles are selectively removed from the system and after some time remaining particles reach a new thermal equilibrium through elastic collisions. The new kinetic energy distribution for the system has lower average kinetic energy and correspondingly the system has a lower average temperature. Evaporative cooling occurs naturally in liquids that are out of thermal equilibrium with their environment. The most energetic particles leave the system in the vapor phase (hence "evaprative cooling"); the remaining liquid is colder. Residents of Tucson are familiar with this process as it is the operating principle behind the evaporative coolers or "swamp coolers" found throughout the city.[1]

This technique can be readily applied to cold atom experiments by selectively removing energetic atoms through spin transitions to untrapped states [78]. In a

[1]The cooling process stops once the vapor-phase is saturated, which happens during the monsoon season in the summer when the relative humidity is high. I've lived in a few houses with evaporative coolers and when swamp coolers stop working, it is **very** uncomfortable.

magnetic trap, where position is proportional to energy, evaporative cooling leads to an increase in density and as a result phase-space density. All dilute-gas BEC experiments to date rely on evaporation for the final stages of cooling.[2]

This selective removal process was discussed in Ch. 4 in the context of Majorana spin flips at the "circle of death" in the TOP trap. Cooling can be achieved in a TOP trap by gradually reducing by the rotating bias field amplitude and correspondingly the "circle of death" radius, R_{COD}.

Alternatively, an radio-frequency (rf) magnetic field can be used to induce a hyperfine spin transition from a trapped state to an untrapped state in atoms whose transition frequency matches the rf frequency. Magnetic trapping potentials provide a position-dependent Zeeman shift, so that the transition frequency between the trapped untrapped states increases when moving away from the center of the trap. Lower rf frequencies remove atoms of lower energy that reside closer to the center from the trap. Since the rf field removes atoms in a very narrow volume in space (which is related to the bandwidth of the rf field and the trap magnetic field gradient), the region in space where atoms are removed is sometimes known as the "rf knife". Evaporative cooling can be achieved by sweeping the frequency of an applied rf field in discrete steps from high frequencies to low frequency; the step time is chosen so the atoms have sufficient time to rethermalize before the frequency is changed.

We have found that the most efficient evaporation results from the combination of rf induced and TOP trap evaporation, where the "circle of death" closely lags the rf field.

[2]Although the mechanism for evaporation is not always through spin transitions to untrapped states [83, 84]

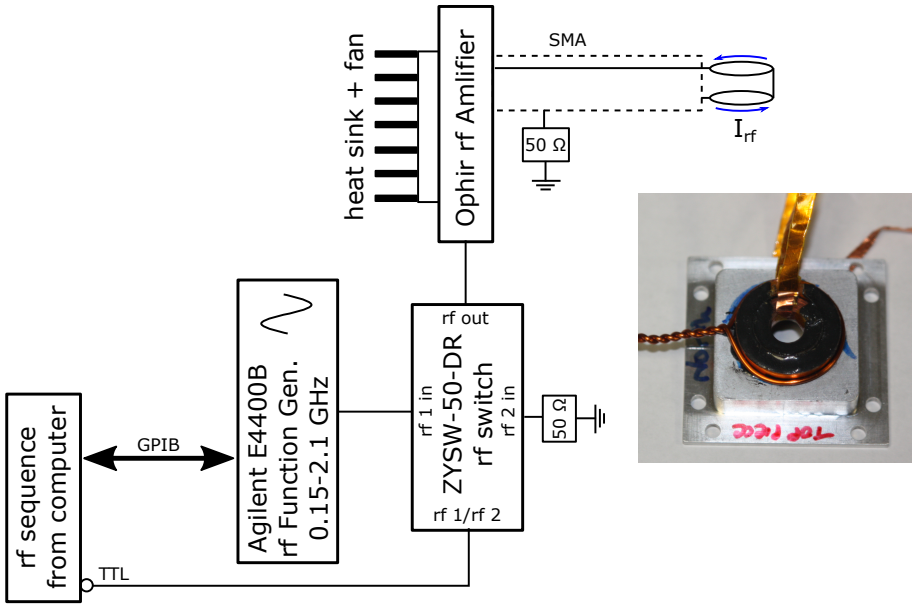

Figure 5.1: Block diagram of the rf electronics used to generate the rf field used during evaporation.

5.1.1 rf electronics

As discussed in the previous chapter, we use a pair of single-turn, Helmholtz coils which are wound around the inner quadrupole coils and epoxied to the quadrupole coil mounting plates to provide the rf evaporation fields. We generate the current for our evaporation sequence using a programmable, Agilent E4400B rf function generator that seeds an Ophir 5303055 Solid State RF amplifier. A MiniCircuits ZYSW-2-50DR rf switch is placed before the amplifier so that the rf field can be turned on and off via a TTL pulse from the timing computer. A set of rf ramps which define an evaporation sequence is pre-loaded from the computer into the function generator via GPIB and triggered by a TTL pulse from the timing computer. Figure 5.1 shows a schematic of the rf electronics along with a picture of the rf coils before being epoxied to the quadrupole coil mount.

5.2 Imaging atoms in a magnetic trap

We image atoms in our magnetic trap using near resonance absorption imaging [34]. To image the cloud of atoms, we shine collimated, near (or on) resonance probe light through the cell. The portion of the light that interacts with the atoms is partially (or completely) absorbed. The reamining probe light is imaged on to a CCD camera and the atoms show up as a dark spot in the center of the probe beam.

The optical depth of the cloud is proportional to the integrated density of atoms along the imaging axis. Since magnetic traps relate position and momentum, measuring the optical depth gives us a way to calculate many of the system parameters including peak density and atom number. In a harmonic trap, such as the TOP trap, where the distribution of atoms is a guassian, parameters such as temperature and phase-space density can be related to the width of the spatial distribution.

In practice, generating an optical density for a cloud of atom requires three images: 1) An absortion image of the atoms, 2) a background image of the probe beam and 3) an image where no imaging light is incident on the camera (the "dark" frame). The measured optical density is given by

$$\mathrm{OD} = -\ln\frac{(I_{absorption} - I_{dark})}{(I_{background} - I_{dark})}. \tag{5.1}$$

Fitting a thermal distribution of atoms in a TOP trap to a Gaussian allows us to calculate physical properties of the cloud. The peak atomic density is

$$n_o = \frac{OD}{r_\perp \sigma(\Delta)}, \tag{5.2}$$

where $r_\perp$ is the width of the Gaussian fit in the horizontal direction and $\sigma(\Delta)$ is the detuning-dependent atom-photon scattering cross section. Using the number

density, the total atom number is just

$$N = n_o \pi^{3/2} r_\perp^2 r_z, \tag{5.3}$$

where $\pi^{3/2} r_\perp^2 r_z$ is the volume of the cloud defined by the Gaussian radii in the horizontal and vertical directions $r_\perp$ and r_z. The temperature, T, of atoms in the TOP trap is given by

$$T = \frac{\mu_B}{4k_B} \frac{B'^2 r_\perp^2}{B_0}, \tag{5.4}$$

where k_B is the Boltzmann constant, μ_B is the Bohr magneton and B_0 and B' are the parameters of the TOP trap described in section 5.1.3. From here we can calculate phase-space density, which is our figure of merit for optimizing the evaporation sequence. For a much more complete discussion of the imaging techniques used in our group, see Kali Wilson's, Joe Lowney's or David Scherer's PhD dissertations [44, 43, 85].

Figure 5.2 shows an example of the three components of a given image and a calculated optical depth based on those images. The purpose of the "background subtraction" is to remove artifacts of the image that come from aspects of the optical system other than the atoms. Examples of artifacts include dust particles on optics, edges of optical mounts or interference fringes. As shown in the set of images in Fig.5.2 our most frustrating imaging artifact comes from what we believe is partially damaged anti-reflection coating that occured during cell construction. Diffraction from the edges of the damaged coating (which is $\sim$5 mm from the image plane at the atoms) causes significant interference friges, to the point that we have a difficult time imaging atoms near the coating fringes. Fortunately, the final position of the

BEC is far enough away from these fringes that we have not had trouble imaging atoms.[3]

Since we trap atoms in the $|F = 1, m_F = -1\rangle$ state, we have the option of using either the repump light ($|F = 1\rangle \rightarrow |F' = 2\rangle$) or the cooling light ($|F = 2\rangle \rightarrow |F' = 3\rangle$) for the probe beam. If the cooling light is used for imaging, the atoms must be pumped into $|F = 2\rangle$ using the repump light. In this case we shine repump light along an axis perpendicular to the image axis. We couple a small portion (a few mW) of the 3D repump light into a fiber for imaging. The cooling imaging light comes from the zeroth order light from the 3D tapered amplifier which passes through a double pass AOM and the frequency is shifted to the desired detuning. Both the repump and cooling light are delivered to the vacuum chamber via fiber.

Typically, we use repump light to image atoms in the quadrupole trap where the cloud is optically thick, and cooling light to image atoms in the BEC where the atom number (and thus OD) is much lower.

[3]We have on a few occasions considered removing the coating to clean up the imaging system. One of the technicians in the 2nd floor optics shop suggested using a solution of hydrochloric acid (HCl) and copper sulfate (CuSO4) which is a common algicide used in swimming pools. Apparently the street name for this solution is "Green River". Since we were unfamiliar with the technique we decided not to try removing the coating for the time being. This is something that may be worth revisiting in the future.

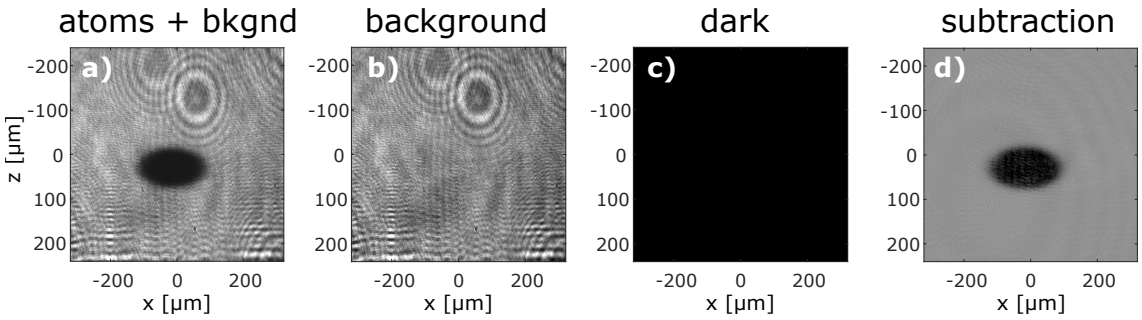

Figure 5.2: Diagram of the absorption imaging process for a thermal cloud in the quadrupole trap. An image of the absorption of a near-resonant probe beam is recorded on the camera. The probe beam is typically large enough so that the intensity is constant over the size of the atoms. We record two reference frames: b) the background probe intensity with no atoms and c) a dark frame where the camera is only illuminated by the scattered light from the experiment or from the room. We then process the image and reconstruct the optical density of the cloud. d) shows the reconstructed image. Although the atoms in a) are easily distinguished by eye, the background subtraction process is useful for observing smaller features like the BEC.

We use a 7-mm diameter, collimated imaging beam that comes directly from a fiber collimating package. The imaging beam passes through a half wave plate and then is sent directly to the atoms. We have the option of imaging the atoms using three distinct imaging systems: 1) a horizontal imaging system with a magnification of M $\sim$0.5, 2) a horizontal imaging system with a magnification of M =4.83 and 3) a vertical imaging system with a magnification of M $\sim$ 5.[4] The two higher magnification imaging systems use a matched achromat pair as an imaging objective. The light that passes through the objectives is focused directly on to a CCD camera. The low magnification imaging system uses a macro lens which threads on to the CCD camera's plastic housing. To date, all of the images in our system come from a Point Grey, 1.3 MP Chameleon camera that is triggered by a TTL pulse from the

[4]We calibrate the magnification of the M = 4.83; imaging system carefully by releasing atoms from the TOP trap and allowing them to fall. We determine the magnification of the imaging system by fitting the free fall position to a parabola with acceleration, g = 9.8 m/s^2.

timing computer.

We typically use a few hundred μW of power in the imaging beams ($\ll I_{sat}$). Image pulses range between 20-150 μs per pulse depending on the optical depth of the atoms being image and the frequency of the imaging light. Camera gain and shutter settings are determined such that the probe light does not saturate the camera.

5.3 rf evaporation to BEC

Once atoms have been transfered from the MOT chamber to either one of the science chambers, we transfer and evaporatively cool atoms in the quadrupole trap mounted on the shuttle. The final stages of cooling occur in BEC 2 in a $\omega_r \times \omega_z = 2\pi \times (37.5 \times 106.1)$Hz TOP trap. The following sections details the process of transferring atoms from the final transfer coil to the quadrupole trap and the rf evaporation of atoms to BEC. Figure 5.6 shows the timing sequence for producing the BEC starting with the transfer of atoms from the MOT cell through the formation and imaging of the BEC.

5.3.1 Transfer into the quadrupole trap

The final stages of the BEC production occur in the science chamber. The first step in this process is to transfer atoms from the last transfer coil into a linear trap created by the quadrupole coils attached to the shuttle. When loading from the final transfer coil into the final magnetic trap, the two pairs of quadrupole coils operate as a single coil. We transfer atoms to the quadrupole trap by ramping off the current in the last transfer coil while simultaneously ramping on the current in the quadrupole pairs over a period of 100 ms. We run $\sim$3 A through each of the

two coil pairs which produces a quadrupole trap with a gradient of ∼250 G/cm. Since we run equal amounts of current through the two quadrupole pairs the local minimum of the trap is equidistant from the two sides of the mount. As long as the shuttle has been aligned properly, this corresponds to a position very close to the center of the science cell. The magnetic field minimum in the quadrupole trap defines the final position where the BEC is created later in the cooling process.

5.3.2 rf evaporation in the quadrupole trap

Immediately after transferring atoms into the quadrupole trap, we turn on the rf field at 80 MHz and sweep the frequency from 80 MHz to 30 MHz over a period of ∼1 sec. The purpose of this high frequency sweep is to remove the non-thermal, high energy atoms from the trap without allowing time for rethermalization.

Following the high frequency cut, we sweep the rf field from 30 MHz to 9.5 MHz over a period of 27.67 seconds. Over the course of this stage of evaporation the cloud of atoms becomes more and more localized near the center of the trap and increases in density, something that is clearly evident in Fig. 5.3.

5.3.3 Transfer to TOP trap

At this point in the sequence we transfer atoms from the quadrupole trap into the 2 kHz TOP trap by ramping up the current in the AC TOP coils to ∼1.25 A over a period of 75 msec, while simultaneously ramping the quadrupole field gradient to 300 G/cm. We ramp the quadrupole gradient out so that the trap geometry does not change significantly when transferring to the TOP trap.

In other words, the cloud of atoms in the quadrupole trap is mode-matched as much as possible to the new trap geometry. We optimize the TOP trap geometry

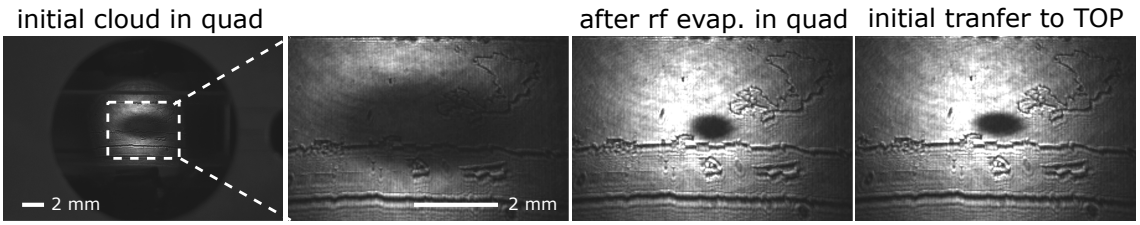

Figure 5.3: Sequence of images showing the process for transferring atoms from the final quadrupole trap into the TOP trap. The first two images show the distribution of atoms after loading into the final quadrupole trap. The atoms then undergo a period of rf evaporation in the quadrupole trap. c) shows an image of the cloud after the rf evaporation period in the quadrupole trap. At this point we transfer atoms into the TOP trap by ramping up the bias field and the quadrupole field simultaneously. During the transfer process, the aspect ratio of the trap changes from 2:1 to ∼3:1. This change is evident in c) and d). During this process the cloud undergoes some heating but we able to retain 90% of the atoms.

by optimizing phase-space density in the TOP trap after a brief hold period. For a given bias field value, we scan through a range of quadrupole gradients in order to maximize the atom number. Typically, when the TOP trap is optimized, we can transfer 80-90% of the atoms from the final quadrupole trap into the TOP trap. Fig.5.3 shows a set of images of the atoms during the initial evaporation process and after loading into the TOP trap.

5.3.4 Lifetime measurements

While traps with a non-zero minimum overcome limitations of the quadrupole trap, other loss mechanisms exist that could in principal prevent the creation of a BEC. The predominant mechanisms are three-body recombination and elastic collisions with the background gas [86]. A third loss mechanism is spin-depolarizing collisions, however these are not a limiting factor in rubidium $|F = 1, m_F = -1\rangle$ traps.

At high atom densities and low temperatures, inelastic collisions between three atoms can occur where two of the atoms form a dimer and become untrapped and

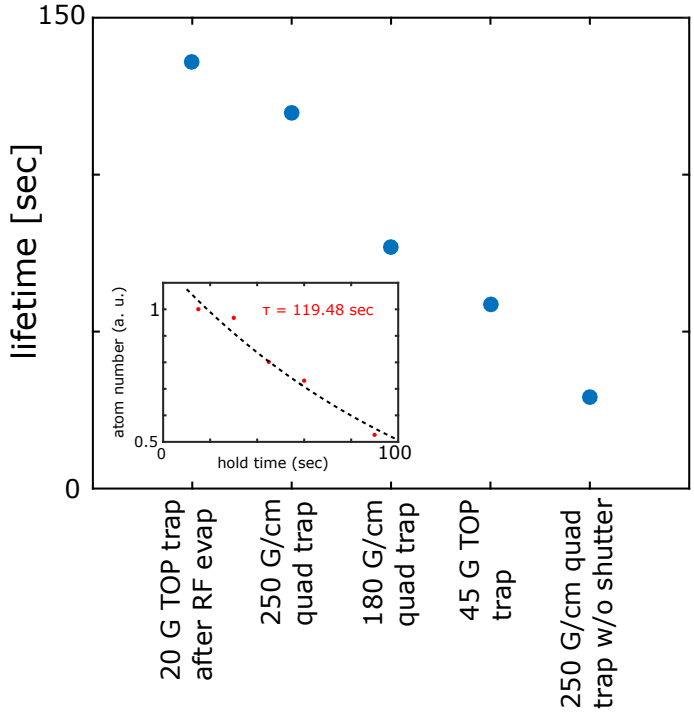

Figure 5.4: Lifetime measurements in various trap geometries and locations in the system. The inset shows an example of a lifetime measurement which involves a fit of the number of trapped atoms as a function of time to an exponential decay. From there, we extract a 1/e lifetime.

the third atom carries away the excess energy in the form of kinetic energy. Since this collisional energy is typically much larger than the trap depth, all three atoms are lost. This type of loss mechanism is typically a relevant in optical traps where initial densities are much higher than in magnetic traps or near the end stages of evaporation in magnetic traps where the cloud is very cold and very dense.[5]

During the initial stages of evaporation in the TOP trap in BEC 2, the atom density is low enough (1×10^9 cm^{-3}) that three-body losses are not a concern.

In weak traps where number density is lower, the evaporation process, which proceeds by rethermalizing elastic collisions, is less efficient than in higher strength

[5]In BEC 1, evaporation takes place in two stages, at first a tight trap and then later a much weaker ("sag") trap, in order to avoid such losses. In BEC 2 we keep a constant, tight trap potential during the evaporation process.

traps. In this regime collisions with high energy atoms in the background gas are the dominant loss mechanism. Evaporation towards BEC will be efficient if the background gas collision limited lifetime of the atoms in the TOP trap is (much) longer than the evaporation timescales.

The TOP trap geometries in BEC 2 are similar to those in BEC 1, so evaporation timescales should be similar between the two experiments. We can use the evaporation times in BEC 1, ∼60 sec, as a benchmark for the evaporation timescales in BEC 2. Figure 5.4 shows a lifetime measurement of atoms in the TOP trap in the science chamber and in quadrupole traps in the 3D MOT chamber and science chamber for comparison. The measurements in Fig. 5.4 suggest a background limited lifetime in the TOP trap of ∼130 sec, which is more than sufficient for achieving BEC.

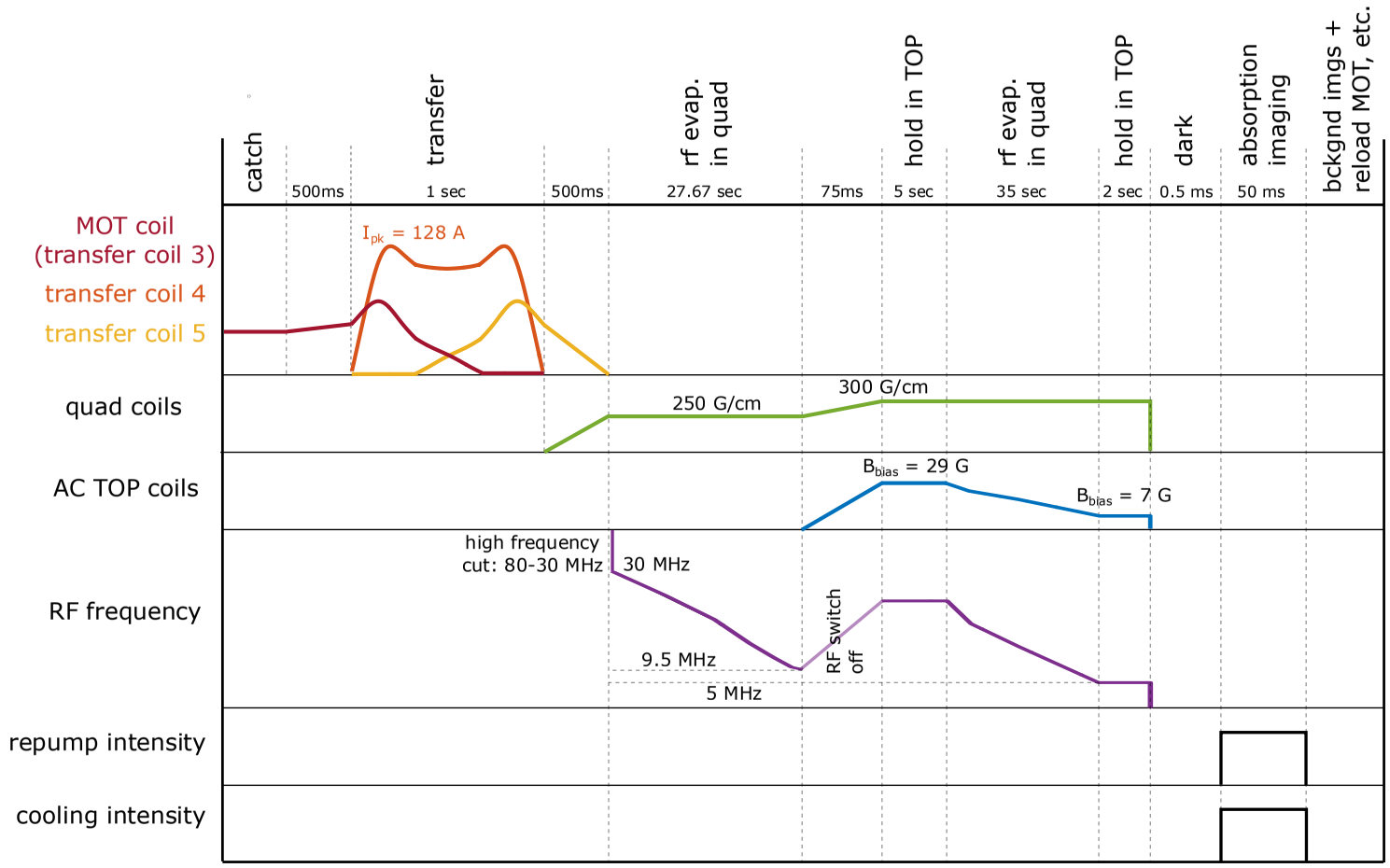

Figure 5.5: Experimental sequence for creating and imaging a BEC in our system starting from magnetic trapped atoms in the 3D MOT chamber. The sequence shows the transfer of atoms from the MOT chamber to the science cell, followed by the evaporation sequence in the final quadrupole trap and then the TOP trap.

5.3.5 Evaporation to BEC in the TOP trap

Before proceeding with the evaporation in the TOP trap, we hold the atoms in the TOP trap for a period of 5 seconds with the rf field off. During the hold period, we jump the rf frequency up to 15 MHz with the rf switch off. At the end of the 5-sec hold period, we turn the rf fields back on and continue the evaporation sequence. The final rf cut to BEC involves a two-stage, 35-sec linear ramp ending with a two second hold period. As long as initial loading conditions into the quadrupole trap are good, at the end of the 2-sec hold period we observe BECs of $\sim$2x10^6 atoms almost every run.[6] Figure 5.5 gives an overview of our magnetic evaporation sequence beginning with the transfer of atoms from the MOT chamber and ending with the formation of the BEC. Figure 5.6 shows images of the atoms during the evaporation process.

[6] If we continue the evaporation sequence immediately after transferring into a TOP trap, we have a difficult time making BECs repeatably. In this case, at the end of the evaporation sequence we observe a thermal cloud about 80% of the time. We suspect that the initial transfer into the TOP trap adds energy to the cloud and alters the kinetic energy distribution. It's possible that without allowing atoms time to rethermalize, the evaporation may be inefficient which would explain the loss of BEC.

In addition to the loss of BEC, we notice that the position of the thermal cloud changes significantly from shot to shot. Gross oscillations in motion in the trap ("sloshing") would also make rf evaporation inefficient as the entire cloud could move through the rf knife during sloshing. In a purely quadratic potential where there is no mechanism for dissipation, atoms could continue sloshing indefinitely. However the TOP trap potential is only approximately harmonic. The slight anharmonicity of trap may allow oscillations to damp out during a hold period, so that the rf evaporation proceeds as intended. With the hold period we generate BECs in the same position to within a few pixels on our camera (the BEC takes up about 60-80 pixels).

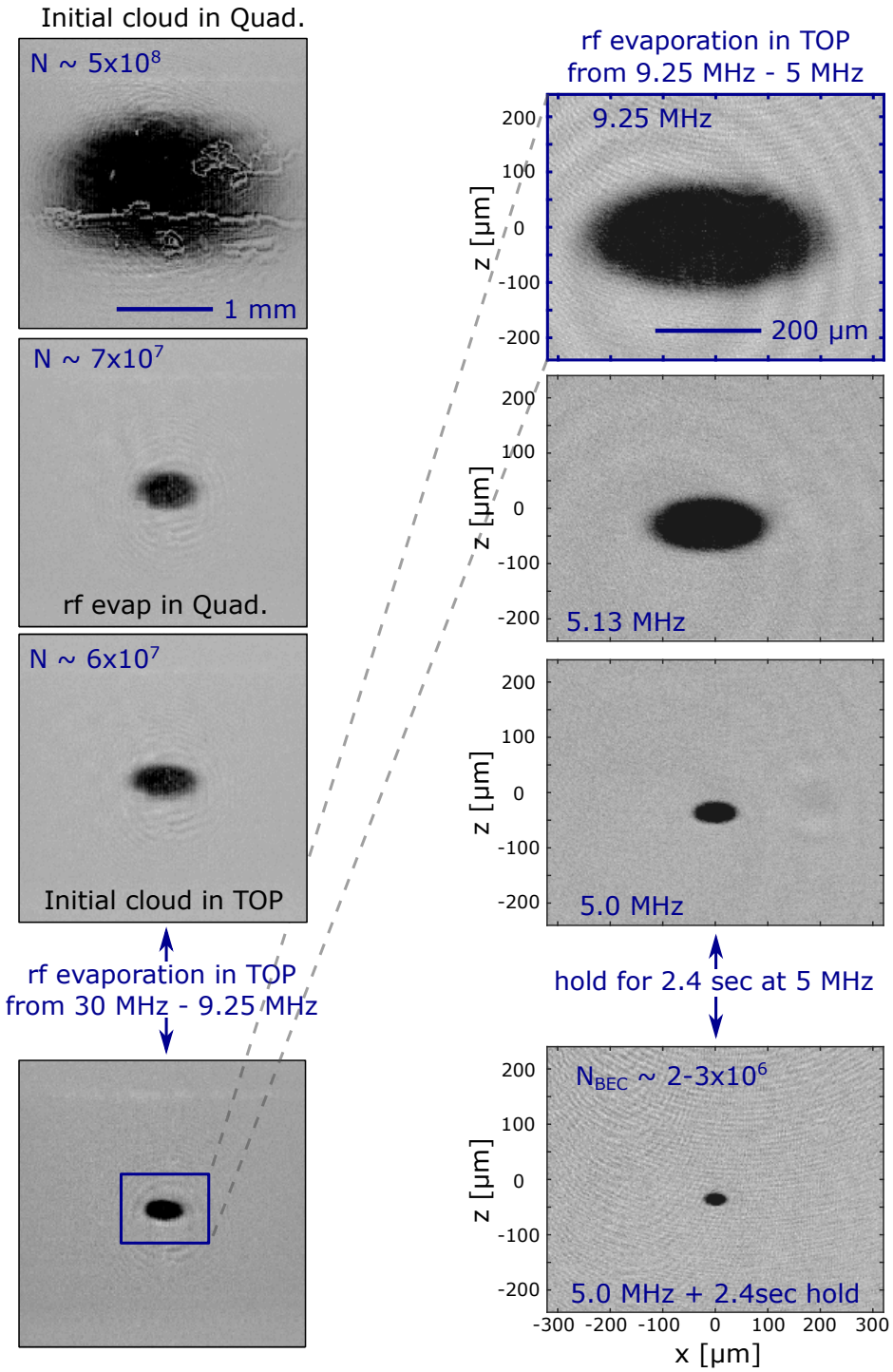

Figure 5.6: Images of the cloud throughout the evaporation sequence. Note the change in atom number and size of the cloud through the evaporation process. During the evaporation process the atom number drops by a factor of ∼100 and the size is reduced by a factor of ∼400.

5.4 BEC

The first fully confirmed BECs in our system were observed after a 13 ms expansion from the $2\pi \times (37.5 \times 106.1)$ Hz TOP trap on Jan. 6, 2016. Looking back and comparing images of atoms in the same trap from the previous month, it is likely that we had achieved BEC near the end of 2015, but had trouble resolving signatures of BEC (i.e. a distinct separation of thermal and BEC atoms).

Fig. 5.7 shows a sequence of images showing the formation of a BEC from a thermal cloud. The formation of the BEC is indicated by the appearance of a narrow, central peak from an initially Gaussian distribution. Since the trap correlates position with energy, the appearance of a dense, central feature during the evaporation indicates a large fraction of atoms populating the zero-energy ground state of the trapping potential: this is the BEC.

In most cases we produce partially condensed clouds with a large condensate fraction and a small thermal component. In this case a cross section of the 2D optical density, shows a bimodal distribution which is a strong indication of condensation.

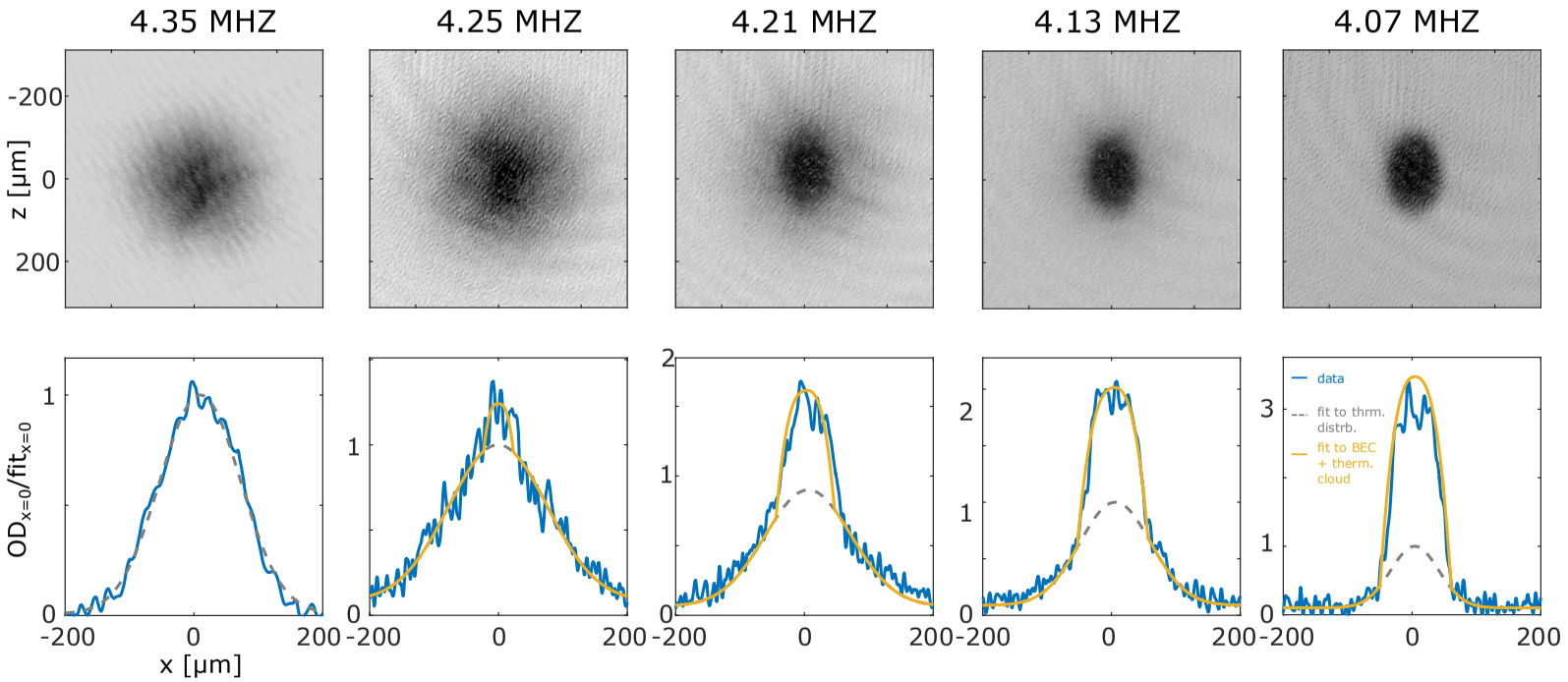

Figure 5.7: Sequence of 200×200μm images during the final stages of the evaporation sequence (top row) showing the formation of a nearly pure BEC (right) from a thermal cloud (left) after a 13 ms expansion from the TOP trap and corresponding cross sections (bottom row). Top row: Sideview images (greyscale) of the velocity distribution of atoms after a 13 ms expansion. The non-condensed fraction of atom appears is isotropic while the condensed fraction is ellitical indicating a non-thermal velocity distribution. Bottom row: Cross sections (blue) of the OD (taken at z=0 μm) are fit to a bimodal distribution (yellow) with the peak OD scaled to the OD of the Gaussian fit (grey). As the atom number in the condensate increases, the parabolic distribution of the BEC dominates over the gaussian distribution of the thermal cloud.

Another indication of condensation is an inversion of the aspect ratio of the condensate during expansion from the trap [24]. A BEC in an anisotropic harmonic trap will expand faster in the tight trapping than in the weak trapping directions leading to an inversion of the aspect ratio of the cloud. Anisotropic expansion is a striking signature of the wavelike properties of the BEC. By contrast, the thermal cloud exhibits isotropic, spherical expansion at long times (a few milliseconds) after it has been released from the trap, even if the trap is anisotropic. That is, at long expansion times the ballistic expansion process correlates the final position of a given atom with it's initial velocity. Since atoms in a thermal cloud have a gaussian distribution in velocity, the cloud distribution after long expansion times is a isotropic gaussian. For our trap parameters, this inversion of aspect ratio is fairly obvious after ∼13 msec of expansion. The images of the thermal cloud (far left) and the nearly pure BEC (far right) in Fig. 5.7 demonstrate this difference.

5.4.1 Condensate parameters

In a BEC, strong interactions alter the shape of the cloud in a harmonic trap from gaussian, to parabolic. The thermal cloud retains its Gaussian shape. If we look at a cross section along z through the middle of the cloud, the thermal and condensate fractions of the cloud fit to the following distributions:

$$n_{th}(z) = n_{o,th} \cdot g_2 \left[e^{-z^2/\sigma_z^2} \right] \tag{5.5}$$

$$n_c(z) = n_{o,c} \cdot \left[\max\left(1 - z^2/R_{TF,z}^2, 0\right) \right]^{3/2} \tag{5.6}$$

where $n_{th}(z)$ is the thermal distribution, $n(z)$ is the condensate distribution, $n_{o,th}$

and $n_{o,c}$ are the peak densities of the thermal cloud and the condensate respectively, $g_2(x)$ is the dilogarithm function and σ_z and $R_{TF,z}$ are the gaussian width and the Thomas-Fermi radius along z respectively. Fitting a bimodal distribution allows us to measure a number of the physical parameters of the condensate.

A quantitative characterization of the BEC requires a number of relies on an accurate measurement of harmonic trapping frequencies, ω_i, where $i = (x, y, z)$ indicates the axis of the trap. We measured the trap frequency by shifting the minimum of the magnetic trap position in one dimension and observing oscillations of the cloud at subsequent times. A sinusoidal fit to the oscialltions gives us a good measurement of the trap frequencies. Figure 5.8 shows a set of images of the BEC oscillating in the magnetic trap from which we measure the trap frequencies.

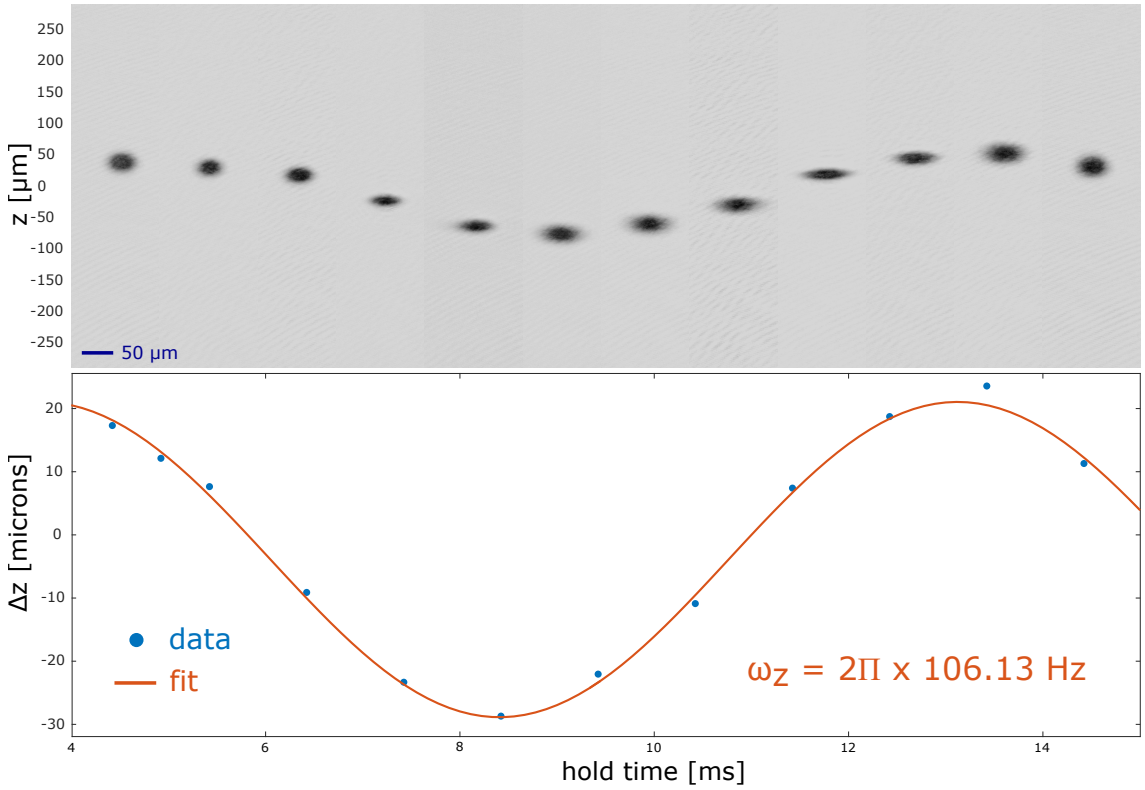

Figure 5.8: An acurate measurement of the trap frequency can be made by momentarily shifting the position of the trap minimum and allowing the atoms to oscillate in the initial trap. We measure the trap frequency by taking a sequence of images at subsequent points in time after the initial kick. The top plot shows a sequence of 12 images of the cloud oscillating in the trap and the bottown plot shows the clouds displacement from the initial trap minimum (blue) with a sinusoidal fit (orange).

Once we have a measurement of the trap frequency, the atom number in the BEC can be calculated from a good measurement of the Thomas-Fermi radius, $R_{TF,i}$, which is extracted by fitting a cross section of the density to Eq. 5.6. From here, we can calculate the atom number in the BEC using:

$$N = \frac{15a}{l}\left(\frac{mR_{TF,i}^2\omega_i^2}{\hbar\bar{\omega}}\right)^{5/2} \tag{5.7}$$

where $\bar{\omega} = (w_\perp^2 w_z)^{(1/3)}$ is the geometric mean of the radial ($\omega_\perp$) and axial (ω_z) trap frequencies, a is the scattering length and $l = \sqrt{\hbar/m\bar{\omega}}$ is the harmonic oscillator

length for a trap with freuency $\bar{\omega}$.

As discussed in Ch. 1, the fraction of atoms in the condensate, N_0/N, follows

$$\frac{N_0}{N} = 1 - \left(\frac{T}{T_C}\right)^3 \tag{5.8}$$

where N_0 is the condensate fraction, N is the total atom number, T is the temperature and T_C is the critical temperature at which condensation occurs. A measurement of the critical temperature can be made by mapping out the condensate number as a function of temperature in trap.

CHAPTER 6

Gravito-magnetic trap

High contrast imaging of trapped atoms requires a well defined magnetic field axis aligned with the imaging axis. While the TOP trap provides the harmonic confinement necessary for achieving BEC, the magnetic field axis direction rotates with the bias field making *in situ* imaging more difficult.

In this chapter I discuss our implementation of the gravito-magnetic (GM) trap, which provides harmonic confinement with a non-zero potential minimum using DC magnetic fields and has a well defined axis that is co-propagating with our imaging axis.

6.1 Trapping potentials for in trap imaging

In general, the most efficient imaging of atoms is achieved by having a well defined magnetic field axis. Choosing a quantization axis lifts the degeneracy of the magnetic sub-levels and allows us to address specific m_F states for imaging by choosing the image light polarization and detuning carefully. The so called "stretched" states offer the most efficient imaging for two reasons: 1) they have the highest atom-field coupling strengths and 2) they access cycling transitions for circularly polarized light so multiple atom-photon scattering events can occur for a single image.[1]

As mentioned above, the TOP trap magnetic field direction varies with the rotating field. In our tightly confining TOP trap, the atoms occupy a region close

[1]For a more detailed discussion of imaging atoms in a TOP trap, see Kali Wilson's thesis [43].

to the center position of the quadrupole field. At this position, the magnitude of the field in the z-direction (imaging axis) is close to zero and the magnetic field axis of the trap is aligned with the 7 G rotating field which is perpendicular to the imaging direction.

In the following section I present our implementation of the gravito-magnetic trap, which provides an all-magnetic, weak spherical, harmonic confinement with a well defined, static magnetic field axis in the z-direction.

6.2 The gravito-magnetic trap

The gravito-magnetic (GM) refers to a weak, harmonic magnetic trap geometry where atoms are supported against gravity by a combination of a quadrupole field and one or more bias coils whose axes are in the direction of the gravity. Leandhart textitet.al [87] first demonstrated gravito-magnetic trapping of picoKelvin temperature BECs of ^{23}Na atoms in a $\sim 2\pi\times1$ Hz spherical trap. The apparatus in the aforementioned paper used a bias coil located inside the vacuum chamber to support atoms against gravity. More recently Bertoldi and Ricci [88] loaded an ensemble of cold atoms into a GM trap directly from a MOT using a set of six cylindrically symmetric coils with precisely tailored currents located outside the vacuum chamber which allows improved optical access over *in vacuo* coils.

Our implementation of the GM trap utilizes a set five magnetic field coils located immediately outside the science cell. These consist of two pairs of quadrupole coils which share an axis with gravity (the z direction) and are spatially offset from each other along the axis and a curvature coil which is concentric with the quadrupole coils. Figure 6.1 shows a diagram of the coil configuration for the GM trap.

In our trap, current in the curvature coil is adjusted so that the sum of the po-

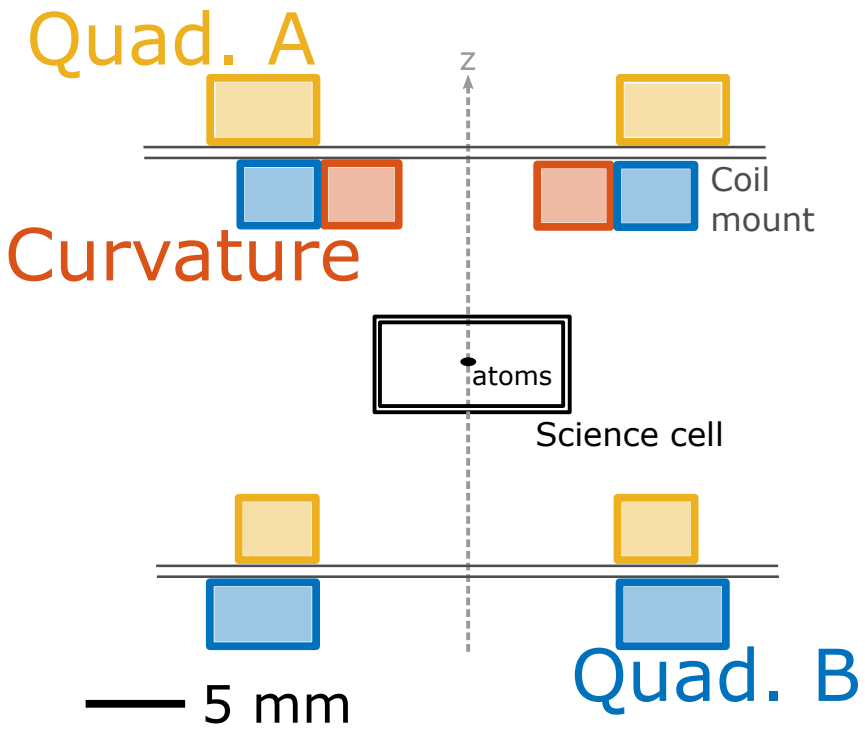

Figure 6.1: GM trap coil layout.

tential gradients from the quadrupole coils and the curvature coil identically cancel the potential gradient due to gravity. In this case, the potential in the z direction is harmonic with a trap frequency set by the field curvature from the curvature coil. The radial trap geometry depends on a balance between the field curvature from the quadrupole and curvature coils and conditions can be chosen such that the trap is also harmonic in the radial direction. Trap frequencies can be adjusted by varying the current in the quadrupole and curvature coils. Figure 6.2 shows the trap geometry for a set of currents that result in a nearly spherical $\sim 2\pi\times 7$ Hz harmonic trap.

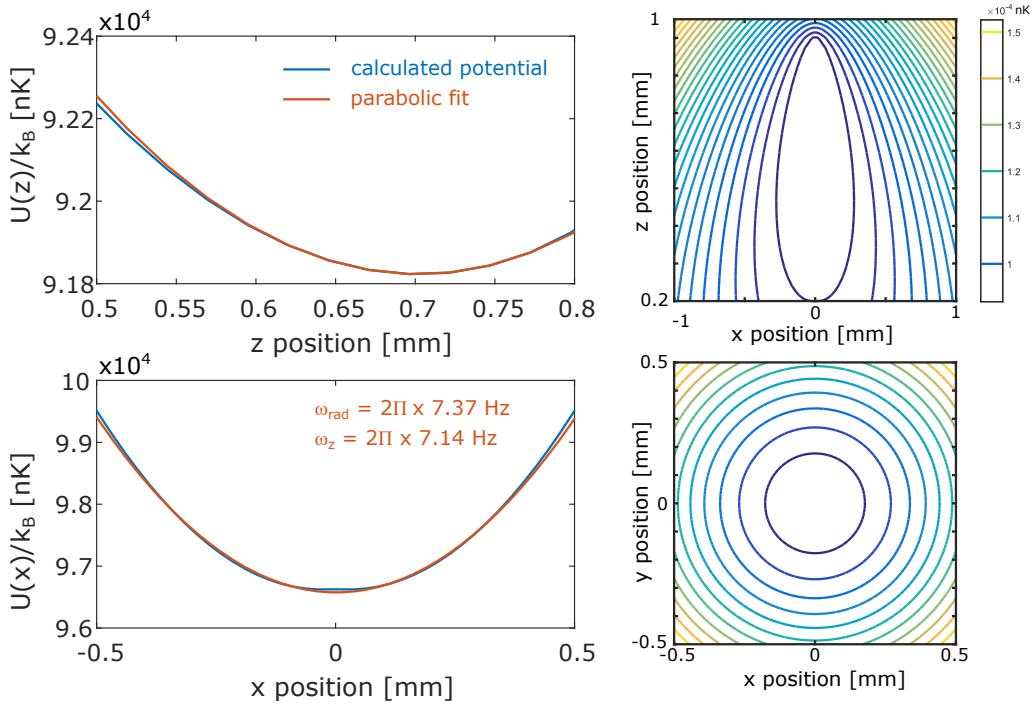

Figure 6.2: Cross sections (blue) of the GM trap potential energy in the z (top left) and x (bottom left) with parabolic fits (orange). A cross sections of the trap potential in x-z (top right) and x-y (bottom right) show the shape of the GM trap. The current configurations indicated in Fig. 6.3 result in a nearly spherical $\sim 2\pi \times 7$ Hz trap.

Since the GM trap is a relatively weak trap, we have had difficulty evaporating in this trap. Instead, we follow our normal evaporation procedure in the TOP trap to BEC, and then transfer the BEC into the gravity trap. We start the transfer process by linearly ramping the quadrupole and bias field down so that the atoms are confined in a weak TOP trap. From there, we ramp up the current in the curvature coil while simultaneously ramping off the TOP bias field and adjusting the current in the two pairs of quadrupole coils. We transfer atoms from the tight trap to the gravity trap slowly, over a period of 8 sec, as we have found that a slow ramp drastically reduces sloshing in the GM trap. Figure 6.3 shows the current ramp sequence for transferring a BEC into the gravity trap.

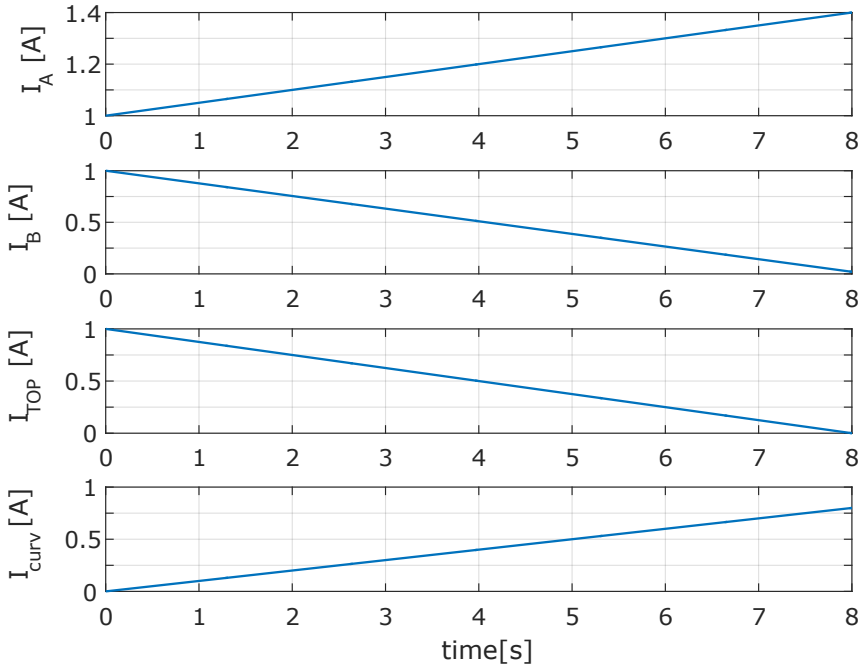

Figure 6.3: Current ramps in the five GM trap coils.

Figure 6.4 shows an image and a cross section of BEC in our GM trap. Based on the fitted Thomas-Fermi radius we estimate that we can transfer a BEC of $\sim 1\times10^6$ atoms into the GM trap.

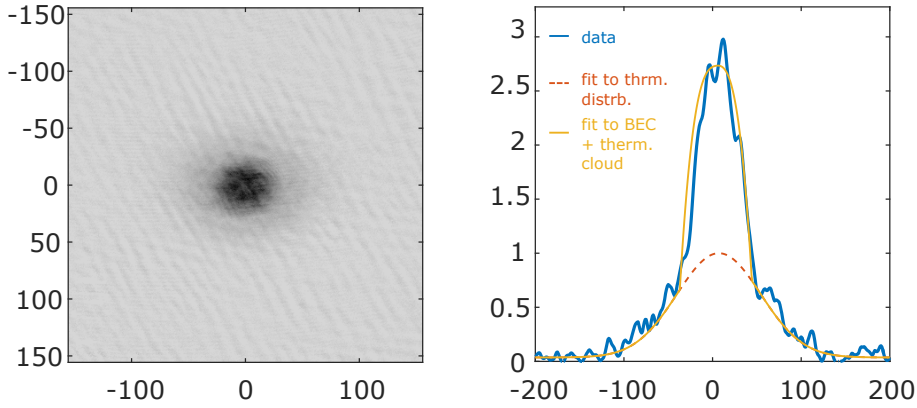

Figure 6.4: a) Side view image of a BEC with $N_{BEC} \sim 1\times10^6$ in the gravitomagnetic trap. b) Cross section (blue) of the OD of the BEC in the GM trap (at z=0 μm) fit to a bimodal distribution (yellow) with the peak OD scaled to the OD of the Gaussian fit (orange).

CHAPTER 7

Conclusion

In this dissertation I have presented the design and construction of BEC 2 which is capable of furthering the *in situ* vortex studies in BEC 1 have recently achieved BECs of ^{87}Rb in our new apparatus with $N \sim 2 \times 10^6$ atoms. The new apparatus improves on our original system in a number of areas.

First, we have designed a compact apparatus that utilizes optical fibers to deliver light to diverging beam 2D and 3D MOTs. In the future, we anticipate adding a laser system for cooling ^{39}K. With the addition of a ^{39}K laser system our apparatus will be capable of producing ^{39}K BECs and performing dual species experiments.

Second, we have increased optical access to the science chamber. With the improved optical access, we have the ability to utilize commercially available, short working distance microscope objectives with NAs up to ∼0.46. We anticipate that this will allow us to image vortices *in situ* in highly oblate BECs with aspect ratios up to 11:1.

Third, we have designed a flexible, all-magnetic trapping system using a modular coil mount design. We currently trap and cooling in a harmonic, TOP trap with an aspect ratio of ∼2:1. With the modular design we have the ability to trap atoms in a pencil shaped trap (utilizing a QUIC trap) and with the addition of a 1064-nm laser beam, we can access weak, highly oblate trapping geometries with aspect ratios ∼10:1.

Finally, we have demonstrated the transfer of a BEC from a TOP trap into a spherical gravito-magnetic trap. Calculations have shown that the radial-to-axial

aspect ratio of the gravito-magnetic trap can be adjusted continuously from 1:1 (spherical) to ∼4:1 (oblate) by varying the current in a "curvature" coil whose axis is parallel to gravity. In addition, the gravito-magnetic trap has a well defined magnetic-field axis aligned with the imaging axis, which is beneficial for in trap vortex studies.

7.1 Future work

At the time of writing there is still a few important additions which need to be designed and installed before BEC 2 is running as "science" machine. The major additions to the system are as follows:

1. **Optical dipole trap:** We are currently in the process of constructing a 1064-nm optical-dipole trap which will be used to trap and cool atoms to BEC. Several techniques for all-optical evaporation to BEC have been demonstrated in ^{87}Rb [84, 89, 90, 91]. The strong trap depths achieved by tightly focused optical traps lead to fast evaporation times, often on the order of ∼10s. Using an optical trap for evaporation will increase our daily number of runs and increase the productivity.

   In most cases the final trap is all optical and these experiments take advantage of the fact that optical traps are state independent to investigate state dependent physics. We intend to follow the procedure described in [91] with the addition of a small bias magnetic field parallel to our imaging axis (and gravity) that will define the quantization axis for imaging.

   By focusing the optical trap light with a cylindrical lens, we will be able to access the trap geometries necessary for studying 2DQT and Onsager's point-vortex model.

2. **High-NA imaging sytem:** As we have shown in previous studies [43, 44, 32] high NA microscope objective is essential for *in situ* imaging of vortices. To that end, we plan to purchase and install a 50X Mitutoyo Plan Apo SL infinity-corrected microscope objective. We anticipate that a higher-NA objective and weaker radial trap frequencies will allow us to resolve vortex cores *in situ*.

3. **Holographic tweezer system:** We are also in the process of developing a extension to our vortex manipulation technique [31] using a digital micromirror device (DMD) as an amplitude hologram. At present, we have demonstrated the ability to generate 8 stirring beams with the DMD. In the near future, this technique will be implemented and tested on BEC 1; a duplicate this system will be installed in BEC 2.

REFERENCES

[1] A. Einstein. Quantum Theory of the Monatomic Ideal Gas. *Sitzungberichte der Preussischen Akademie der Wissenschaften, Pysikalisch-mathematische Klasse*, pages 261–267, 1925.

[2] A. Einstein. Quantum Theory of the Monatomic Ideal Gas, Part II. *Sitzungberichte der Preussischen Akademie der Wissenschaften, Pysikalisch-mathematische Klasse*, pages 3–14, 1925.

[3] S. N. Bose. Plancks Gesetz und Lichtquantenhypothese. *Zetischrift fur Physik*, 26:178–181, 1924.

[4] P. Kapitza. Viscosity of Liquid Helium below the λ-Point. *Nature*, 141(3558): 74–74, 1938.

[5] Allen J. F. and D. Misener. Flow of Liquid Helium II. *Nature*, 141(3558):75–75, 1938.

[6] F. London. The λ-Phenomenon of Liquid Helium and the Bose-Einstein Degeneracy. *Nature*, 141(3558):643–644, 1938.

[7] L. Onsager. Statistical Hydrodynamics. *Il Nuovo Cimento*, 6(2), 1949.

[8] W. F. Vinen. The Detection of Single Quanta of Circulation in Liquid Helium II. *Proc. of the Roy. Soc. of London A*, 260(1301):218–236, 1961.

[9] P. W. Karn, D. R. Starks, and W. Zimmermann. Observation of Quantization of Circulation in Rotating Superfluid ^{4}He. *Phys. Rev. B*, 21(5):1797–1805, 1980.

[10] D. J. Thouless, P. Ao, Q. Niu, M. R. Geller, and C. Wexler. Quantized Vortices in Superfluids and Superconductors. *International Journal of Modern Physics B*, 13(05):675–686, 1999.

[11] Tilley D.R. and Tilley J. *Superfluidity and Superconductivity.* Adam Hilger, New York, 3rd edn., 1990.

[12] R. J. Donnelly. *Quantized Vortices in Helium II.* Cambridge University Press, Cambridge, 2nd edn., 1991.

[13] E. J. Yarmchuk, M. J V Gordon, and R. E. Packard. Observation of Stationary Vortex Arrays in Rotating Superfluid Helium. *Phys. Rev. Lett.*, 43(3):214–217, 1979.

[14] H. E. Hall and W. F. Vinen. The Rotation of Liquid Helium II. I. Experiments on the Propagation of Second Sound in Uniformly Rotating Helium II. *Proc. of the Roy. Soc. of London A*, 238(1213):204–214, 1956.

[15] S. W. Van Sciver and C. F. Barenghi. Visualisation of Quantum Turbulence. *Progress in Low Temperature Physics*, 16(3):247–303, 2009.

[16] G. P. Bewley, D. P. Lathrop, and K. R. Sreenivasan. Superfluid Helium: Visualization of Quantized Vortices. *Nature*, 441(558), 2006.

[17] G. P. Bewley, K. R. Sreenivasan, and D. P. Lathrop. Particles for Tracing Turbulent Liquid Helium. *Experiments in Fluids*, 44(6):887–896, 2008.

[18] E. Fonda, K. R. Sreenivasan, and D. P. Lathrop. Liquid Nitrogen in Fluid Dyamics: Visualization and Velocimetry Using Frozen Particles. *Review of Scientific Instruments*, 83(8), 2012.

[19] G. P. Bewley, M. S. Paoletti, K. R. Sreenivasan, and D. P. Lathrop. Characterization of Reconnecting Vortices in Superfluid Helium. *Proceedings of the National Academy of Sciences*, 105(37):13707–13710, 2008.

[20] D. P. Meichle, C. Rorai, M. E. Fisher, and D. P. Lathrop. Quantized Vortex Reconnection: Fixed Points and Initial Conditions. *Phys. Rev. B*, 86(1):014509, 2012.

[21] M. S. Paoletti, Michael E. Fisher, K. R. Sreenivasan, and D. P. Lathrop. Velocity Statistics Distinguish Quantum Turbulence from Classical Turbulence. *Phys. Rev. Lett.*, 101(15):154501, 2008.

[22] E. Fonda, D. P. Meichle, N. T. Ouellette, S. Hormoz, and D. P. Lathrop. Direct Observation of Kelvin Waves Excited by Quantized Vortex Reconnection. *Proceedings of the National Academy of Sciences*, 111(1):4707–4710, 2014.

[23] M.S. Paoletti, R. B. Fiorito, K. R. Sreenivasan, and D. P. Lathrop. Visualization of Superfluid Helium Flow. *Journal of the Physical Society of Japan*, 77(11): 111007, 2008.

[24] M. H. Anderson, J. R. Ensher, M. R. Matthews, C. E. Wieman, and E. A. Cornell. Observation of Bose-Einstein Condensation in a Dilute Atomic Vapor. *Science*, 269(5221):198–201, 1995.

[25] K. B. Davis, M. O. Mewes, M. R. Andrews, N. J. Van Druten, D. S. Durfee, D. M. Kurn, and W. Ketterle. Bose-Einstein Condensation in a Gas of Sodium Atoms. *Phys. Rev. Lett.*, 75(22):3969–3973, 1995.

[26] C. C. Bradley, C. A. Sackett, J. J. Tollett, and R. G. Hulet. Evidence of Bose-Einstein Condensation in an Atomic Gas with Attractive Interactions. *Phys. Rev. Lett.*, 75(9):1687–1690, 1995.

[27] C. C. Bradley, C. A. Sackett, J. J. Tollett, and R. G. Hulet. Evidence of Bose-Einstein Condensation in an Atomic Gas with Attractive Interactions [Phys. Rev. Lett. 75, 1687 (1995)]. *Phys. Rev. Lett.*, 79(6):1170–1170, 1997.

[28] K. W. Madison, F. Chevy, W. Wohlleben, and J. Dalibard. Vortex Formation in a Stirred Bose-Einstein Condensate. *Phys. Rev. Lett.*, 84(5):806–809, 2000.

[29] E. P. Gross. Structure of a Quantized Vortex in Boson Systems. *Nuovo Cimento*, 20(3):454–477, 1961.

[30] L. P. Pitaevskii. Vortex Lines in an Imperfect Bose Gas. *Soviet Physics JTEP*, 13(2):451–454, 1961.

[31] E. C. Samson, K. E. Wilson, Z. L. Newman, and B. P. Anderson. Deterministic Creation, Pinning, and Manipulation of Quantized Vortices in a Bose-Einstein Condensate. *Phys. Rev. A*, 93(2):023603, 2016.

[32] K. E. Wilson, Z. L. Newman, J. D. Lowney, and B. P. Anderson. *In Situ* Imaging of Vortices in Bose-Einstein Condensates. *Phys. Rev. A*, 91:023621, 2015.

[33] C. Pethick and H. Smith. *Bose-Einstein Condensation in Dilute Gases*. Cambridge University Press, Cambridge, 2nd edn., 2008.

[34] W Ketterle, D. S. Durfee, and D. M. Stamper-Kurn. Making, Probing and Understanding Bose-Einstein Condensates. In *Proceedings of the International School of Physics*, page 67, 1999.

[35] J. R. Abo-Shaeer, C. Raman, J. M. Vogels, and W. Ketterle. Observation of Vortex Lattices in Bose-Einstein Condensates. *Science*, 292(5516):476–479, 2001.

[36] A. S. Bradley and B. P. Anderson. Energy Spectra of Vortex Distributions in Two-Dimensional Quantum Turbulence. *Phys. Rev. X*, 2(4):041001, 2012.

[37] T. W. Neely, E. C. Samson, A. S. Bradley, M. J. Davis, and B. P. Anderson. Observation of Vortex Dipoles in an Oblate Bose-Einstein Condensate. *Phys. Rev. Lett.*, 104(16):1–4, 2010. ISSN 0031-9007.

[38] B. P. Anderson, P. C. Haljan, C. E. Wieman, and E. A. Cornell. Vortex Precession in Bose-Einstein Condensates: Observations with Filled and Empty Cores. *Phys. Rev. Lett.*, 85:2857–2860, 2000.

[39] D. V. Freilich, D. M. Bianchi, A. M. Kaufman, T. K. Langin, and D. S. Hall. Real-Time Dynamics of Single Vortex Lines and Vortex Dipoles in a Bose-Einstein Condensate. *Science*, 329(5996):1182–1185, 2010.

[40] Angela C. White, Brian P. Anderson, and Vanderlei S. Bagnato. Vortices and Turbulence in Trapped Atomic Condensates. *Proceedings of the National Academy of Sciences*, 111(1):4719–4726, 2014.

[41] G. S. Settles. *Schlieren and Shadowgraph Techniques: Visualizing Phenomena in Transparent Media*. Springer-Verlag, Berlin, 2001.

[42] M. R. Andrews, M.-O. Mewes, N. J. van Druten, D. S. Durfee, D. M. Kurn, and W. Ketterle. Direct, Nondestructive Observation of a Bose Condensate. *Science*, 273(5271):84–87, 1996.

[43] Kali Wilson. *Developing a Toolkit for Experimental Studies of Two-Dimensional Quantum Turbulence in Bose-Einstien Condensates*. PhD thesis, University of Arizona, 2015.

[44] Joseph Lowney. *Manipulating and Probing Angular Momentum and Quantized Circulation in Optical Fields and Matter Waves*. PhD thesis, University of Arizona, 2016.

[45] M. Gajdacz, P. L. Pedersen, T. Morch, A. J. Hilliard, J. Arlt, and J. F. Sherson. Non-Destructive Faraday Imaging of Dynamically Controlled Ultracold Atoms. *Review of Scientific Instruments*, 84(8), 2013.

[46] J. E. Curtis, B. A. Koss, and D. G. Grier. Dynamic Holographic Optical Tweezers. *Optics Communications*, 207(1-6):169–175, 2002.

[47] A. Ashkin, J. M. Dziedzic, J. E. Bjorkholm, and S. Chu. Observation of a Single-beam Gradient Force Optical Trap for Dielectric Particles. *Optics letters*, 11 (5):288, 1986.

[48] W. Petrich, M. H. Anderson, J. R. Ensher, and E. A. Cornell. Behavior of Atoms in a Compressed Magneto-Optical Trap. *J. Opt. Soc. Am. B*, 11(8): 1332, 1994.

[49] W. S. Bakr, J. I. Gillen, A. Peng, S. Fölling, and M. Greiner. A Quantum Gas Microscope for Detecting Single Atoms in a Hubbard-regime Optical Lattice. *Nature*, 462(7269):74–77, 2009.

[50] W. S. Bakr, A. Peng, M. E. Tai, R. Ma, J. Simon, J. I. Gillen, S. Fölling, L. Pollet, and M. Greiner. Probing the Superfluid-to-Mott Insulator Transition at the Single-Atom Level. *Science*, 329(5991):547–550, 2010.

[51] W. Alt. An Objective Lens for Efficient Fluorescence Detection of Single Atoms. *Assembly*, 3(3):142–144, 2002.

[52] L. M. Bennie, P. T. Starkey, M. Jasperse, C. J. Billington, R. P. Anderson, and L. D. Turner. A Versatile High Resolution Objective for Imaging Quantum Gases. *Optics express*, 21(7):9011–6, 2013.

[53] J. F. Sherson, C. Weitenberg, M. Endres, M. Cheneau, I. Bloch, and S. Kuhr. Single-Atom-Resolved Fluorescence Imaging of an Atomic Mott Insulator. *Nature*, 467(7311):68–72, 2010.

[54] B. Zimmermann, T. Muller, J. Meineke, T. Esslinger, and H. Moritz. High-Resolution Imaging of Ultracold Fermions in Microscopically Tailored Optical Potentials. *New Journal of Physics*, 13, 2011.

[55] E. A. Salim, S. C. Caliga, J. B. Pfeiffer, and D. Z. Anderson. High Resolution Imaging and Optical Control of Bose-Einstein Condensates in an Atom Chip Magnetic Trap. *Applied Physics Letters*, 102(8), 2013.

[56] C. D'Errico, M. Zaccanti, M. Fattori, G. Roati, M. Inguscio, G. Modugno, and A. Simoni. Feshbach Resonances in Ultracold ^{39}K. *New Journal of Physics*, 9 (7):223, 2007.

[57] A. Marte, T. Volz, J. Schuster, S. Dürr, G. Rempe, E. G. M. van Kempen, and B. J. Verhaar. Feshbach Resonances in Rubidium 87: Precision Measurement and Analysis. *Phys. Rev. Lett.*, 89(28):283202, 2002.

[58] H. Takeuchi, S. Ishino, and M. Tsubota. Binary Quantum Turbulence Arising from Countersuperflow Instability in Two-Component Bose-Einstein Condensates. *Phys. Rev. Lett.*, 105(20), 2010.

[59] T. W. Hänsch and A. L. Schawlow. Cooling of Gases by Laser Radiation. *Optics Communications*, 13(1):68–69, 1975.

[60] M. Kasevich and S. Chu. Laser Cooling Below a Photon Recoil with Three-Level Atoms. *Phys. Rev. Lett.*, 69(12):1741–1744, 1992.

[61] W. D. Phillips, J. V. Prodan, and H. J. Metcalf. Laser Cooling and Electromagnetic Trapping of Neutral Atoms. *J. Opt. Soc. Am. B*, 2(11):1751, 1985.

[62] P. D. Lett, R. N. Watts, C. I. Westbrook, W. D. Phillips, P. L. Gould, and H. J. Metcalf. Observation of Atoms Laser Cooled below the Doppler Limit. *Phys. Rev. Lett.*, 61(2):169–172, 1988.

[63] H. J. Metcalf. *Laser Cooling and Trapping*. Springer, New York, NY, 1999.

[64] C.J. Foot. *Atomic Physics*. Oxford University Press, New York, NY, 2005.

[65] D. A. Steck. Rubidium 87 D Line Data. available online at http://steck.us/alkalidata (revision 2.1.4, 23 December 2010), 2010.

[66] K. L. Corwin, Z. T. Lu, C. F. Hand, R. J. Epstein, and C. E. Wieman. Frequency-Stabilized Diode Laser with the Zeeman Shift in an Atomic Vapor. *Applied Optics*, 37(15):3295–3298, 1998.

[67] J. T. Walraven. Two-dimensional Magneto-Optical Trap as a Source of Slow Atoms. *Phys. Rev. A*, 58(5):3891–3895, 1998.

[68] Z. T Lu, K. L. Corwin, M. J. Renn, M. H. Anderson, E. A. Cornell, and C. E. Wieman. Low-Velocity Intense Source of Atoms from a Magneto-Optical Trap. *Phys. Rev. Lett.*, 77(16):3331–3334, 1996.

[69] Thomas Uehlinger. *A 2D Magneto-Optical Trap as a High-Flux Source of Cold Potassium Atoms*. PhD thesis, ETH-Zurich, 2008.

[70] Matthew B Squires. *High Repetition Rate Bose-Einstein Condensate Production in a Compact, Transportable Vacuum System.* PhD thesis, University of Colorado, 2008.

[71] W.D. Phillips and H. J. Metcalf. Laser Deceleration of an Atomic Beam. *Phys. Rev. Lett.*, 48(596), 1982.

[72] E. Riis, D. S. Weiss, K. A. Moler, and S. Chu. Atom Funnel for the Production of a Slow, High-Density Atomic Beam. *Phys. Rev. Lett.*, 64(14):1658–1661, 1990.

[73] J.M. Kohel, J. Ramirez-Serrano, R.J. Thompson, L. Maleki, J.L. Bliss, and K.G. Libbrecht. Generation of an Intense Cold-Atom Beam from a Pyramidal Magneto-Optical Trap: Experiment and Simulation. *J. Opt. Soc. Am. B*, 20 (1161), 2003.

[74] M. Greiner, I. Bloch, T. Hänsch, and T. Esslinger. Magnetic Transport of Trapped Cold Atoms Over a Large Distance. *Phys. Rev. A*, 63(3):1–4, 2001.

[75] D. E. Pritchard. Cooling Neutral Atoms in a Magnetic Trap for Precision Spectroscopy. *Phys. Rev. Lett.*, 51(15):1336–1339, 1983.

[76] U. Ernst, A. Marte, F. Schreck, J. Schuster, and G. Rempe. Bose-Einstein Condensation in a Pure Ioffe-Pritchard Field Configuration. *Europhysics Letters*, 41(1):1–6, 1998.

[77] T. Esslinger, I. Bloch, and T. W. Hänsch. Bose-Einstein Condensation in a Quadrupole-Ioffe-Configuration Trap. *Phys. Rev. A*, 58(4):R2664–R2667, 1998.

[78] K. B. Davis, M.-O. Mewes, M. A. Joffe, M. R. Andrews, and W. Ketterle. Evaporative Cooling of Sodium Atoms. *Phys. Rev. Lett.*, 74(26):5202–5205, 1995.

[79] W. Petrich, M. H. Anderson, J. R. Ensher, and E. A. Cornell. Stable, Tightly Confining Magnetic Trap for Evaporative Cooling of Neutral Atoms. *Phys. Rev. Lett.*, 74(17):3352–3355, 1995.

[80] T. Bergeman, G. Erez, and H. J. Metcalf. Magnetostatic Trapping Fields for Neutral Atoms. *Phys. Rev. A*, 35(4):1535–1546, 1987.

[81] P. R. Gray, P. J. Hurst, S. H. Lewis, and R. G. Meyer. *Analysis and Design of Analog Integrated Circuits*. Wiley, 2009.

[82] T. W. Neely, A. S. Bradley, E. C. Samson, S. J. Rooney, E. M. Wright, K. J. H. Law, R. Carretero-González, P. G. Kevrekidis, M. J. Davis, and B. P. Anderson. Characteristics of Two-Dimensional Quantum Turbulence in a Compressible Superfluid. *Phys. Rev. Lett.*, 111(23):235301, 2013.

[83] S. Stellmer, B. Pasquiou, R. Grimm, and F. Schreck. Laser Cooling to Quantum Degeneracy. *Phys. Rev. Lett.*, 110(26):263003, 2013.

[84] J. F. Clément, J. P. Brantut, M. Robert-De-Saint-Vincent, R. A. Nyman, A. Aspect, T. Bourdel, and P. Bouyer. All-Optical Runaway Evaporation to Bose-Einstein Condensation. *Phys. Rev. A*, 79(6), 2009.

[85] David R. Scherer. *Vortex Formation by Merging and Interference of Multiple Trapped Bose-Einstein Condensates*. PhD thesis, University of Arizona, 2007.

[86] J. Williams, R. Walser, C. Wieman, J. Cooper, and M. Holland. Achieving Steady-State Bose-Einstein Condensation. *Phys. Rev. A*, 57(3):2030–2036, 1998.

[87] A. E. Leanhardt, T. A. Pasquini, M. Saba, A. Schirotzek, Y. Shin, D. Kielpinski, D. E. Pritchard, and W. Ketterle. Cooling Bose-Einstein Condensates Below 500 picoKelvin. *Science*, 301(5639):1513–1515, 2003.

[88] A. Bertoldi and L. Ricci. Gravito-magnetic trapping of ^{87}Rb. *J. Phys. B*, 41 (15):3891–3895, 2008.

[89] T. Kinoshita, T. Wenger, and D. S. Weiss. All-optical Bose-Einstein condensation using a compressible crossed dipole trap. *Phys. Rev. A*, 71(1), 2005. ISSN 10502947.

[90] K. J. Arnold and M. D. Barrett. All-Optical Bose-Einstein Condensation in a 1.06 μm Dipole Trap. *Optics Communications*, 284(13):3288–3291, 2011.

[91] Y.-J. Lin, A. R. Perry, R. L. Compton, I. B. Spielman, and J. V. Porto. Rapid Production of ^{87}Rb Bose-Einstein Condensates in a Combined Magnetic and Optical Potential. *Phys. Rev. A*, 79(6):063631, 2009.